Electronic Theses and Dissertations, 2004-2019

2016

Understanding Hydroclimatic Controls on Stream Network Dynamics using LiDAR Data

Seoyoung Kim
University of Central Florida

UNDERSTANDING HYDROCLIMATIC CONTROLS ON STREAM NETWORK DYNAMICS USING LIDAR DATA

by

SEOYOUNG KIM
B.S. Kyung Hee University, 2002
M.S. Seoul National University, 2004

A dissertation submitted in partial fulfillment of the requirements
for the degree of Doctor of Philosophy
in the Department of Civil, Environmental, and Construction Engineering
in the College of Engineering and Computer Science
at the University of Central Florida
Orlando, Florida

Spring Term
2016

Major Professor: Dingbao Wang

ABSTRACT

This dissertation investigates the hydroclimatic controls on drainage network dynamics and characterizes the variation of drainage density in various climate regions. The methods were developed to extract the valley and wet channel networks based on Light Detection and Ranging (LiDAR) data including the elevation and intensity of laser returns. The study watersheds were selected based on the availability of streamflow observations and LiDAR data. Climate aridity index was used as a quantitative indicator for climate.

The climate controls on drainage density were re-visited using watersheds with minimal anthropogenic interferences and compared with the U-shape relationship reported in the previous studies. A curvature-based method was developed to extract a valley network from 1-m LiDAR-based Digital Elevation Models. The relationship between drainage density and climate aridity index showed a monotonic increasing trend and the discrepancy was explained by human interventions and underestimated drainage density due to the coarse spatial resolution (30-meter) of the topographic maps used in previous research.

Observations of wet channel networks are limited, especially in headwater catchments in comparison with the importance of stream network expansion and contraction. A systematic method was developed to extract wet channel networks based on the signal intensities of LiDAR ground returns, which are lower on water surfaces than on dry surfaces. The frequency distributions of intensities associated with wet surface and dry surface returns were constructed. With the aid of LiDAR-based ground elevations, signal intensity thresholds were identified for extracting wet channels. The developed method was applied to Lake Tahoe area during recession

periods in five watersheds. A power-law relationship between streamflow and wet channel length was obtained and the scaling exponent was consistent with the reported findings from field work in other regions.

Perennial streams flow for the most of the time during normal years and are usually defined based on a flow duration threshold. The streamflow characteristics of perennial streams in this research were assessed using the relationship between streamflow exceedance probability and wet channel ratio based on wet channel networks extracted from LiDAR data. Non-dimensional analysis based on the relationship between streamflow exceedance probability and wet channel ratio showed that results were consistent with previous research about perennial stream definition, and provided the possibility to use wet channel ratio to define perennial streams.

Wetlands are important natural resources and need to be monitored regularly in order to understand their inundation dynamics, function and health. Wetland mapping is a key part of monitoring programs. A framework for detecting wetland was developed based on LiDAR elevation and intensity information. After masking out densely vegetated areas, wet areas were identified based on signal intensity of ground returns for barrier islands in East-Central Florida. The intensity threshold of wet surface was identified by decomposing composite probability distribution functions using a Gamma mixture model and the Expectation-Maximization algorithm. This method showed good potential for wetland mapping.

The methodology developed in this dissertation demonstrated that incorporating LiDAR data into the drainage networks, stream network dynamics and wetlands results in enhanced understanding of hydroclimatic controls on stream network dynamics. LiDAR data provide a rich

information source including elevation and intensity, and are of great benefit to hydrologic research community.

This dissertation is dedicated to the memory of my father.

BYUNGSUN KIM

July 7, 1942 – December 30, 2011

ACKNOWLEDGMENTS

I also would like to thank the members of my dissertation committee, Dr. Stephen C. Medeiros (Co-Chair), Dr. Boo Hyun Nam, Dr. Arvind Singh, Dr. David M. Sumner. Their contributions have significantly improved this work and I look forward to working with them in the future. A special thank you to Milad Hooshyar with whom I have closely work over this dissertation.

I had the honor of working alongside some outstanding students including Milad Hooshyar, Xi Chen, Debapi Ghosh, Han Xiao, Yin Tang and Marwan Kheimi. They have each taught me in valuable skills and I am fortunate to not only call them my colleagues, but more importantly, my friends. I hope we will continue to work together after my graduation.

Most importantly, I am thankful for the unconditional love and support from my wife, Sukkyung Kim, my mother, Yonggan Kim and my daughters, Joy and Athena. They have provided me with the best education possible for which I am eternally grateful.

TABLE OF CONTENTS

x

LIST OF FIGURES

LIST OF TABLES

CHAPTER 1: INTRODUCTION

1.1 Introduction

The drainage network in a watershed is an important geomorphic and hydrological feature exerting significant control on runoff generation, which is vitally important for practical water resource management. A drainage network is comprised of both unchannelized valleys and channels [*Montgomery and Foufoula‑Georgiou*, 1993]. At a valley head, flow changes from unconfined sheet flow on hillslope to confined flow in valley. Localized confined flow dominates in valleys as a result of convergent topography with positive contour curvature [*Peucker and Douglas*, 1975; *Howard*, 1994]. Drainage or valley lines can be identified based on V-shaped contours [*Pelletier, 2013*]. Drainage density (D_d) is defined as the ratio of the total length of valley in a watershed to its drainage area [*Horton*, 1932; 1945]. Drainage density quantitatively shows the efficiency of a drainage system. Watersheds with denser drainage network usually produce higher peak flows and sediment loads [*Dunne and Leopold*, 1978]. Drainage density is controlled by various factors including climate, soil, vegetation and topography [*Melton*, 1957; *Carlston*, 1963; *Montgomery and Dietrich*, 1988] as well as through hydrologic processes such as infiltration, soil saturation, runoff, erosion and sediment transport, reflecting the signature of climate, geomorphology and hydrology [*Moglen et al.*, 1998].

Wet channel networks can expand, contract, disconnect and reconnect hydrologically in response to rainfall events and land use change [*Schumm*, 1956; *Howard and Kerby*, 1983]. Therefore, channels are categorized as perennial streams, intermittent streams, and ephemeral

streams based on flow durations. Perennial streams flow for the most time during normal years and are maintained by groundwater discharge [*Meinzer*, 1923; *NC Division of Water Quality*, 2010]. *Hedman and Osterkamp* [1982] defined channels with flowing water for more than 80% of the time as perennial streams; *Hewlett* [1982] and *Texas Forest Service* [2000] used 90% as the threshold. Intermittent streams flow during certain times of the year (i.e. seasonal) receiving water from surface sources such as melting snow or from a groundwater source such as a spring [*Meinzer*, 1923; *Levick et al.*, 2008]. Variations in the water table have an effect on the characteristics of intermittent streams that are supplied by groundwater sources [*Meinzer*, 1923]. Ephemeral streams flow only in direct response to precipitation without continuous surface flow [*Meinzer*, 1923]. The total volume of flow under the annual hydrograph from an ephemeral stream watershed is the result of direct runoff from large rainfall events [*Chow et al.*, 1988]. Some ephemeral streams flow only for several hours annually [*Blasch et al.*, 2002]. Intermittent and ephemeral streams flow with high temporal and spatial variability [*Levick et al.*, 2008] and support biodiversity and other important ecosystem processes [*Acuña et al.*, 2014].

Research on stream network dynamics has attracted attention in recent years [*Wigington et al.*, 2005; *Godsey and Kirchner*, 2014; *Goulsbra et al.*, 2014; *Whiting and Godsey*, 2016]. Wet channel networks expand in response to rainfall events and contract during streamflow recession periods. The temporal and spatial dynamics of wet channel networks are one of the key features for understanding the linkage between hydrology and geomorphology driven by climate [*Abrahams*, 1984; *Wang and Wu*, 2013], mechanisms on individual hydrologic processes [*Biswal and Marani*, 2010], stream ecosystem expansion and contraction [*Stanley et al.*, 1997] , and spatial variability in stream chemistry [*Zimmer et al.*, 2013; *McGuire et al.*, 2014]. The drying and

wetting dynamics usually occur on temporal streams located in the headwater catchments. It will benefit both hydrologic and ecological research to monitor the short-term changes in wet channel networks. However, streamflow gauges operated by United States Geologic Survey (USGS) are generally sited on relatively large perennial streams and rivers. Observations on the drying and wetting dynamics of ephemeral streams are usually obtained through field work [*Blyth and Rodda*, 1973].

The challenge is to accurately identify valley heads and channel heads in order to quantify drainage density and channel density in watersheds across climate regions, and further to understand the mechanisms of stream dynamics. Accurate drainage network identification is also important to engineering practices such as road design and land development [*Swisher*, 2002]. The identification of channel heads in the field is difficult and time consuming [*Clubb et al.*, 2014]. Therefore, several methods have been developed to extract drainage networks based on topographic data such as a digital elevation model (DEM). The traditional approach for identifying channel heads was to use a unique contributing area threshold [*O'Callaghan and Mark*, 1984; *Band*, 1986; *Tarboton et al.*, 1991] or slope-area relationship [*Montgomery and Dietrich*, 1988; *Willgoose et al.*, 1991; *Dietrich et al.*, 1992; *Dietrich et al.*, 1993; *Ijjasz-Vasquez and Bras*, 1995]. Recent methods used the tangential curvature from a DEM [*Lashermes et al.*, 2007; *Passalacqua et al.*, 2010; *Sofia et al.*, 2011; *Pelletier*, 2013].

Recent technology such as airborne Light Detection and Ranging (LiDAR) is able to obtain high resolution topographic data that permits direct detection of valleys and channels, and provides an opportunity to explore the fundamental questions of geomorphology such as landslides, hillslopes and channelization processes [*Derron and Jaboyedoff*, 2010; *Jaboyedoff et al.*, 2012;

3

Booth et al., 2013]. LiDAR has become an important technique to acquire topographic data at sub-meter resolution and accuracy [*Marks and Bates*, 2000; *Bowen and Waltermire*, 2002], and has been utilized to extract topographic depressions [*Le and Kumar*, 2014] and drainage networks [*Passalacqua et al.*, 2010; *Sofia et al.*, 2011; *Pelletier*, 2013; *Clubb et al.*, 2014].

The intensity information of LiDAR data provides an opportunity to identify wet channel networks. LiDAR has been used to retrieve water surface information including flood inundation extent [*Genc et al.*, 2005] and water levels and gradients [*Magirl et al.*, 2005; *Hopkinson et al.*, 2011]. As an active remote sensing technique, the airborne LiDAR sensor emits Near-infrared (NIR) laser pulses with a wavelength of 1064 nm that cannot readily penetrate water. Most of infrared laser light is absorbed by the water column or reflected specularly away from the field of view of the discrete echo recording system [*Wolfe and Zissis*, 1985; *Brzank et al.*, 2008]. The signal intensity, which is the relative strength measurement of the return pulse by the LiDAR sensor, is typically lower from the water surface compared with dry lands. The intensity characteristics of the water surface have previously been used to derive water-land boundaries in river segments [*Höfle et al.*, 2009].

Intensity information from single wavelength topographic LiDAR (i.e., NIR) systems has been used to map many types of water surfaces including rivers, wetlands, ponds, and lakes [*Höfle et al.*, 2009; *Smeeckaert et al.*, 2013; *Wu et al.*, 2013]. *Antonarakis et al.* [2008] identified a water surface in a river segment when the height range of the returns is less than 0.5 m and an average intensity value in a local domain is less than a threshold. *Lang and McCarty* [2009] demonstrated the ability of LiDAR intensity data to map inundated areas beneath a forest canopy. *Brzank et al.* [2008] developed a supervised classification method for identifying laser points on the water

surface of Wadden Sea using elevation, intensity, and 2D point density. These studies were successful in delineating water-land boundary of large continuous water areas (i.e., geometrical assessment of water bodies), including those with canopy issues.

1.2 <u>Hypothesis and Objectives</u>

The goal of this research is to evaluate the hydroclimatic controls on drainage network dynamics and characterize the variation of drainage density in various climate regions. A method was developed to extract the valley and wet channel networks based on the LiDAR data. The overarching hypothesis of the research is as follows:

The wet channel network can be identified by LiDAR data and the temporal dynamics of drainage networks can be linked to hydrologic processes.

The hypothesis is tested in an ensemble of watersheds across a spectrum of climatic and topographic gradients based on the hydroclimatic data availability. The purpose of research is addressed through the identification of valley and wet channel networks, using LiDAR data acquired in these watersheds. High spatial resolution LiDAR data including elevation and intensity of ground returns provide a unique opportunity to answer the research subjects. The main objectives to be achieved in this research are as follows:

1. Investigate the climate control on drainage density by quantifying the drainage density in natural watersheds using LiDAR data.

5

2. Develop a systematic framework for mapping wet channel networks based on the signal intensity of near infrared LiDAR ground returns, and construct the relationship between wet channel length and streamflow in regions where multiple streamflow gages and LiDAR survey data are available.

3. Evaluate the streamflow characteristics of perennial streams based on the wet channel network extracted from LiDAR data.

4. Develop a detection framework for wet areas to aid in wetland detection using the geometric and intensity information of LiDAR data in barrier islands in East-Central Florida.

1.3 Climate Control on Drainage Density

The drainage network is a fundamental geomorphological and hydrological property in a watershed. Drainage density quantitatively demonstrates the efficiency of a drainage system. Climate, soil, vegetation and topography are all factors that control the drainage density [*Carlston*, 1963; *Melton*, 1957; *Montgomery and Dietrich*, 1988]. Chapter 2 presents the climate control on drainage density compared with the U-shape relationship from *Melton* [1957] and *Madduma Bandara* [1974]. 121 study sites with minimum human interferences and various climate regions were selected based on the availability of LiDAR data, which were used to generate digital elevation models (DEMs) with a spatial resolution of 1-meter. A curvature-based method, incorporating both positive and negative curvature information, was developed to extract a valley (drainage) network from LiDAR-based DEMs.

6

1.4 Mapping Wet Channel Networks

The temporal dynamics of stream network is vitally important for understanding hydrologic process including groundwater interactions and hydrograph recessions. However, *in situ* observations of wet channel networks are limited, especially in headwater catchments. Near infrared LiDAR data provides an opportunity to map the wet channel networks, owing to the fine spatial resolution, canopy penetration, and strong absorption of the light energy by the water surface. Chapter 3 presents a systematic method to map wet channel networks based on the signal intensity of ground LiDAR return, which is typically lower on water surfaces than on dry surfaces. The frequency distributions of wet surface and dry surface returns were constructed. With the aid of LiDAR-based ground elevation, the signal intensity thresholds were identified for mapping wet channels.

1.5 Streamflow Characteristics of Perennial Stream

Perennial streams flow for the most of the time during normal years and are governed by groundwater discharge [*Meinzer*, 1923; *NC Division of Water Quality*, 2010]. Perennial streams are usually defined based on a certain threshold of flow duration. However, there are discrepancies in the perennial stream definitions in the literature. Chapter 4 explored the definition of perennial streams using a new non-dimensional relationship between streamflow exceedance probability and wet channel ratio, defined as the wet channel length over the total valley length. The valley network and wet channels were extracted from the LiDAR topographic data, specifically the signal intensity of ground returns with 1-m spatial resolution using the method developed by *Hooshyar*

et al. [2015]. The obtained wet channel ratios of perennial streams in the study watersheds were compared with the definitions of perennial streams in the literatures.

1.6 Detection of Wet Area to Aid in Wetlands Identification

Wetlands are a very important natural resource related to biological diversity and ecosystem processes. Water levels of wetlands have seasonal variations depending on rainfall events and evapotranspiration, and many wetland areas contain standing water for short periods [*Mitsch and Gosselink*, 2007; *Tiner*, 1999]. Wetland extent and type can vary due to changes in topography, land use, climate, and vegetation [*Maxa and Bolstad*, 2009]. Therefore, wetlands need to be monitored regularly in order to understand their inundation dynamics, function and health; wetland mapping is a key part of the monitoring program [*Lang and McCarty*, 2009; *Huang et al.*, 2014]. Chapter 5 presents the detection framework for wet areas to aid in wetlands detection using the geometric and intensity information in the point cloud generated by LiDAR systems. After masking densely vegetated areas out of the study space using LiDAR topographic information, wet areas were identified based on the signal intensity of ground returns for barrier islands in East-Central Florida.

1.7 References

Abrahams, A. D. (1984), Channel networks: a geomorphological perspective, *Water Resources Research*, *20*(2), 161-188.

Acuña, V., T. Datry, J. Marshall, D. Barceló, C. Dahm, A. Ginebreda, G. McGregor, S. Sabater, K. Tockner, and M. Palmer (2014), Why should we care about temporary waterways, *Science*, *343*(6175), 1080-1081.

Antonarakis, A., K. S. Richards, and J. Brasington (2008), Object-based land cover classification using airborne LiDAR, *Remote Sensing of Environment*, *112*(6), 2988-2998.

Band, L. E. (1986), Topographic Partition of Watersheds with Digital Elevation Models, *Water Resources Research*, *22*(1), 15-24.

Biswal, B., and M. Marani (2010), Geomorphological origin of recession curves, *Geophysical Research Letters*, *37*(24).

Blasch, K. W., T. Ferré, A. H. Christensen, and J. P. Hoffmann (2002), New field method to determine streamflow timing using electrical resistance sensors, *Vadose Zone Journal*, *1*(2), 289-299.

Booth, A. M., J. J. Roering, and A. W. Rempel (2013), Topographic signatures and a general transport law for deep-seated landslides in a landscape evolution model, *Journal of Geophysical Research: Earth Surface*, *118*(2), 603-624.

Bowen, Z. H., and R. G. Waltermire (2002), EVALUATION OF LIGHT DETECTION ANI) RANGING (LIDAR) FOR MEASURING RWER CORRIDOR TOPOGRAPHY', *Journal of the American Water Resources Association*, *38*(1).

Brzank, A., C. Heipke, J. Goepfert, and U. Soergel (2008), Aspects of generating precise digital terrain models in the Wadden Sea from lidar–water classification and structure line extraction, *ISPRS Journal of Photogrammetry and Remote Sensing*, *63*(5), 510-528.

Carlston, C. W. (1963), *Drainage density and streamflow*, US Govt. Print. Off.

Chow, V. T., D. R. Maidment, and L. W. Mays (1988), *Applied hydrology*.

Clubb, F. J., S. M. Mudd, D. T. Milodowski, M. D. Hurst, and L. J. Slater (2014), Objective extraction of channel heads from high-resolution topographic data, *Water Resources Research*, *50*(5), 4283-4304.

Derron, M.-H., and M. Jaboyedoff (2010), Preface" LIDAR and DEM techniques for landslides monitoring and characterization", *Natural Hazards and Earth System Science*, *10*(9), 1877-1879.

Dietrich, W. E., C. J. Wilson, D. R. Montgomery, and J. McKean (1993), Analysis of erosion thresholds, channel networks, and landscape morphology using a digital terrain model, *The Journal of Geology*, 259-278.

Dietrich, W. E., C. J. Wilson, D. R. Montgomery, J. McKean, and R. Bauer (1992), Erosion thresholds and land surface morphology, *Geology*, *20*(8), 675-679.

Dunne, T., and L. Leopold (1978), Water in environment planning, edited, Freeman: San Francisco.

Genc, L., S. Smith, and B. Dewitt (2005), Using satellite imagery and LIDAR data to corroborate an adjudicated ordinary high water line, *International journal of remote sensing*, *26*(17), 3683-3693.

Godsey, S., and J. Kirchner (2014), Dynamic, discontinuous stream networks: hydrologically driven variations in active drainage density, flowing channels and stream order, *Hydrological Processes*, *28*(23), 5791-5803.

Goulsbra, C., M. Evans, and J. Lindsay (2014), Temporary streams in a peatland catchment: pattern, timing, and controls on stream network expansion and contraction, *Earth Surface Processes and Landforms*, *39*(6), 790-803.

Hedman, E., and W. Osterkamp (1982), Streamflow characteristics related to channel geometry of streams in western United States, Water Supply Papers-US Geological Survey (USA).

Hewlett, J. D. (1982), *Principles of forest hydrology*, University of Georgia Press.

Höfle, B., M. Vetter, N. Pfeifer, G. Mandlburger, and J. Stötter (2009), Water surface mapping from airborne laser scanning using signal intensity and elevation data, *Earth Surface Processes and Landforms*, *34*(12), 1635-1649.

Hooshyar, M., S. Kim, D. Wang, and S. C. Medeiros (2015), Wet channel network extraction by integrating LiDAR intensity and elevation data, *Water Resources Research*, *51*(12), 10029-10046.

Hopkinson, C., N. Crasto, P. Marsh, D. Forbes, and L. Lesack (2011), Investigating the spatial distribution of water levels in the Mackenzie Delta using airborne LiDAR, *Hydrological Processes*, *25*(19), 2995-3011.

Horton, R. E. (1932), Drainage-basin characteristics, *Eos, Transactions American Geophysical Union*, *13*(1), 350-361.

Horton, R. E. (1945), Erosional development of streams and their drainage basins; hydrophysical approach to quantitative morphology, *Geological society of America bulletin*, *56*(3), 275-370.

Howard, A. D. (1994), A detachment-limited model of drainage basin evolution, *Water resources research*, *30*(7), 2261-2285.

Howard, A. D., and G. Kerby (1983), Channel changes in badlands, *Geological Society of America Bulletin*, *94*(6), 739-752.

Huang, C., Y. Peng, M. Lang, I.-Y. Yeo, and G. McCarty (2014), Wetland inundation mapping and change monitoring using Landsat and airborne LiDAR data, *Remote Sensing of Environment*, *141*, 231-242.

Ijjasz-Vasquez, E. J., and R. L. Bras (1995), Scaling regimes of local slope versus contributing area in digital elevation models, *Geomorphology*, *12*(4), 299-311.

Jaboyedoff, M., T. Oppikofer, A. Abellán, M.-H. Derron, A. Loye, R. Metzger, and A. Pedrazzini (2012), Use of LIDAR in landslide investigations: a review, *Natural hazards*, *61*(1), 5-28.

Lang, M. W., and G. W. McCarty (2009), Lidar intensity for improved detection of inundation below the forest canopy, *Wetlands*, *29*(4), 1166-1178.

Lashermes, B., E. Foufoula-Georgiou, and W. E. Dietrich (2007), Channel network extraction from high resolution topography using wavelets, *Geophysical Research Letters*, *34*(23), L23S04.

Le, P. V., and P. Kumar (2014), Power law scaling of topographic depressions and their hydrologic connectivity, *Geophysical Research Letters*, *41*(5), 1553-1559.

Levick, L. R., D. C. Goodrich, M. Hernandez, J. Fonseca, D. J. Semmens, J. C. Stromberg, M. Tluczek, R. A. Leidy, M. Scianni, and D. P. Guertin (2008), *The ecological and hydrological significance of ephemeral and intermittent streams in the arid and semi-arid American southwest*, US Environmental Protection Agency, Office of Research and Development.

Madduma Bandara, C. M. (1974), Drainage density and effective precipitation, *Journal of Hydrology*, *21*(2), 187-190.

Magirl, C. S., R. H. Webb, and P. G. Griffiths (2005), Changes in the water surface profile of the Colorado River in Grand Canyon, Arizona, between 1923 and 2000, *Water resources research*, *41*(5).

Marks, K., and P. Bates (2000), Integration of high-resolution topographic data with floodplain flow models, *Hydrological Processes*, *14*(11-12), 2109-2122.

Maxa, M., and P. Bolstad (2009), Mapping northern wetlands with high resolution satellite images and LiDAR, *Wetlands*, *29*(1), 248-260.

McGuire, L. A., J. D. Pelletier, and J. J. Roering (2014), Development of topographic asymmetry: Insights from dated cinder cones in the western United States, *Journal of Geophysical Research: Earth Surface*, *119*(8), 1725-1750.

Meinzer, O. E. (1923), Outline of ground-water hydrology, with definitions, US Govt. Print. Off.

Melton, M. A. (1957), An analysis of the relations among elements of climate, surface properties, and geomorphology, DTIC Document.

Mitsch, W. J., and J. G. Gosselink (2007), *Wetlands*, 4th ed., John Wiley and Sons, Inc., N.Y., USA.

Moglen, G. E., E. A. Eltahir, and R. L. Bras (1998), On the sensitivity of drainage density to climate change, *Water Resources Research*, *34*(4), 855-862.

Montgomery, D. R., and W. E. Dietrich (1988), Where do channels begin?, *Nature*, *336*(6196), 232-234.

Montgomery, D. R., and E. Foufoula-Georgiou (1993), Channel network source representation using digital elevation models, *Water Resources Research*, *29*(12), 3925-3934.

NC Division of Water Quality (2010), *Methodology for Identification of Intermittent and Perennial Streams and their Origins, Version 4.11*, North Carolina Department of Environment and Natural Resources, Division of Water Quality. Raleigh, NC.

O'Callaghan, J. F., and D. M. Mark (1984), The extraction of drainage networks from digital elevation data, *Computer Vision, Graphics, and Image Processing*, *28*(3), 323-344.

Passalacqua, P., T. Do Trung, E. Foufoula-Georgiou, G. Sapiro, and W. E. Dietrich (2010), A geometric framework for channel network extraction from lidar: Nonlinear diffusion and geodesic paths, *Journal of Geophysical Research: Earth Surface*, *115*(F1), F01002.

Pelletier, J. D. (2013), A robust, two-parameter method for the extraction of drainage networks from high-resolution digital elevation models (DEMs): Evaluation using synthetic and real-world DEMs, *Water Resources Research*, *49*(1), 75-89.

Peucker, T. K., and D. H. Douglas (1975), Detection of surface-specific points by local parallel processing of discrete terrain elevation data, *Computer Graphics and image processing*, *4*(4), 375-387.

Schumm, S. A. (1956), Evolution of drainage systems and slopes in badlands at Perth Amboy, New Jersey, *Geological society of America bulletin*, *67*(5), 597-646.

Smeeckaert, J., C. Mallet, N. David, N. Chehata, and A. Ferraz (2013), Large-scale classification of water areas using airborne topographic lidar data, *Remote Sensing of Environment*, *138*, 134-148.

Sofia, G., P. Tarolli, F. Cazorzi, and G. Dalla Fontana (2011), An objective approach for feature extraction: distribution analysis and statistical descriptors for scale choice and channel network identification, *Hydrol. Earth Syst. Sci.*, *15*(5), 1387-1402.

Stanley, E. H., S. G. Fisher, and N. B. Grimm (1997), Ecosystem expansion and contraction in streams, *BioScience*, 427-435.

Swisher, G. (2002), Southern Illinois University Carbondale Patent and Copyright Committee meeting, March 8.

Tarboton, D. G., R. L. Bras, and I. Rodriguez-Iturbe (1991), On the extraction of channel networks from digital elevation data, *Hydrological Processes*, *5*(1), 81-100.

Texas Forest Service (2000), Texas Forestry Best Management Practices, online report, http://txforestservice.tamu.edu/uploadedFiles/Sustainable/bmp/Publications/BMP%20Manual_Aug2010%20-%20web.pdf.

Tiner, R. W. (1999), *Wetland indicators: A guide to wetland identification, delineation, classification, and mapping*, CRC Press.

Wang, D., and L. Wu (2013), Similarity of climate control on base flow and perennial stream density in the Budyko framework, *Hydrol. Earth Syst. Sci.*, *17*(1), 315-324.

Whiting, J. A., and S. E. Godsey (2016), Discontinuous headwater stream networks with stable flowheads, salmon river basin, Idaho, *Hydrological Processes*, n/a-n/a.

Wigington, P., T. Moser, and D. Lindeman (2005), Stream network expansion: a riparian water quality factor, *Hydrological Processes*, *19*(8), 1715-1721.

Willgoose, G., R. L. Bras, and I. Rodriguez-Iturbe (1991), A coupled channel network growth and hillslope evolution model: 1. Theory, *Water Resources Research*, *27*(7), 1671-1684.

Wolfe, W., and G. Zissis (1985), The infrared handbook: , Environmental research institute of Michigan for the ofilce of naval research, department of the Navy, Washington, DC.

Wu, H., C. Liu, Y. Zhang, W. Sun, and W. Li (2013), Building a water feature extraction model by integrating aerial image and lidar point clouds, *International journal of remote sensing*, *34*(21), 7691-7705.

Zimmer, M. A., S. W. Bailey, K. J. McGuire, and T. D. Bullen (2013), Fine scale variations of surface water chemistry in an ephemeral to perennial drainage network, *Hydrological Processes*, *27*(24), 3438-3451.

CHAPTER 2: EVALUATING THE DEPENDENCE OF DRAINAGE DENSITY ON CLIMATE AND DRAINAGE AREA BY LIDAR DATA

2.1 Introduction

The drainage network in a watershed is an important geomorphological and hydrological feature with significant control on runoff generation which is vitally important for practical water resource management. A drainage network is composed of unchannelized valleys and channels [*Montgomery and Foufoula-Georgiou*, 1993]. At a valley head, flow changes from unconfined sheet flow on hillslope to confined flow in a valley. Localized confined flow dominates in valleys as a result of convergent topography with positive contour curvature [*Howard*, 1994; *Peucker and Douglas*, 1975]. Drainage or valley lines can be identified based on V-shaped contours *[Pelletier, 2013]*. Drainage density (D_d) is defined as the ratio of the total length of valley in a watershed to its drainage area [*Horton*, 1932; 1945]. Drainage density quantitatively shows the efficiency of a drainage system. Watersheds with denser drainage network usually produce higher peak flow and sediment load [*Dune and Leopold*, 1978].

Drainage density is controlled by various factors including climate, soil, vegetation and topography [*Carlston*, 1963; *Melton*, 1957; *Montgomery and Dietrich*, 1988] as well as through hydrologic processes such as infiltration, soil saturation, runoff, erosion and sediment transport [*Moglen et al.*, 1998]. By analyzing over 80 watersheds in Arizona, New Mexico, Colorado, and Utah, *Melton* [1957] identified a negative correlation between drainage density and precipitation effectiveness (*PE*) index. *PE* index is equal to 10 times the sum of the ratios of monthly precipitation and monthly potential evaporation [*Thornthwaite*, 1931]. Higher *PE* index is

17

corresponding to more humid climate and more available moisture to vegetation. *Madduma Bandara* [1974] presented a positive correlation between drainage density and *PE* index for humid watersheds in Sri Lanka. Combining the data from *Melton* [1957] and *Madduma Bandara* [1974], a U-shaped relationship between D_d and *PE* index is shown in Figure 2-1 by *Abrahams* [1984]. This pattern is explained by the tradeoff between the resistance force of vegetation and the erosion force of runoff [*Abrahams*, 1984].
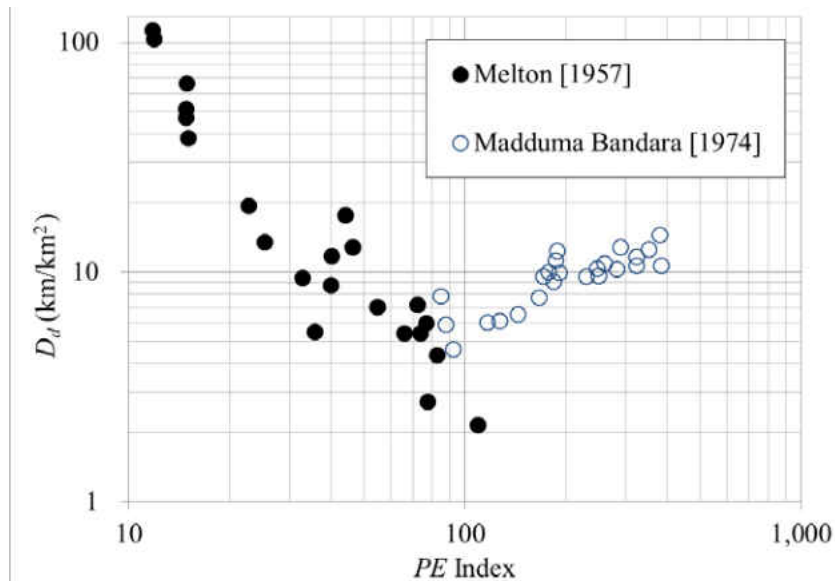
Figure 2-1: Drainage density as a function of precipitation effectiveness (*PE*) index [*Abrahams*, 1984].

Accurate drainage density quantification, depending on the identification of valley heads in watersheds, is important for both hydrology and geomorphology, as well as engineering practices including road design and land development [*Swisher*, 2002]. However, it is a challenging task to map drainage network by field work. Therefore, drainage networks are usually extracted from topographic maps or digital elevation models (DEM). Delineated drainage density is dependent on the resolution of topographic maps [*Morisawa*, 1957; *Schneider*, 1961]. The data

18

points by *Melton* [1957] (black dots in Figure 2-1) were based on the topographic maps with a scale of 1:24,000, which corresponds to a nominal spatial resolution of 30 m. Detailed field investigations were performed in 22 watersheds in Arizona, New Mexico, Colorado, and Utah, where the *PE* index ranges from 12 to 109. The drainage density for the 24 watersheds from Sri Lanka (circles in Figure 2-1) were obtained from maps with a scale of 1:12,672. These watersheds are located in areas with tea plantation and the natural vegetation has been systematically eliminated [*Madduma Bandara*, 1974]. Therefore, the drainage density for humid watersheds in Figure 2-1 is affected by extensive human interferences.

To re-visit the relationship between drainage density and climate, it is important to extract drainage networks in natural watersheds using topographic data with high spatial resolution. Recent technology, such as airborne Light Detection and Ranging (LiDAR), is able to obtain high spatial resolution topographic data that permits direct detection of valleys and provides an opportunity to explore the fundamental questions of geomorphology such as landslides, hillslopes and channelization processes [*Derron and Jaboyedoff*, 2010; *Jaboyedoff et al.*, 2012; *Booth et al.*, 2013]. LiDAR has become an important technique to acquire topographic data in sub-meter resolution and accuracy [*Marks and Bates*, 2000; *Bowen and Waltermire*, 2002]. LiDAR has been utilized to extract openness [*Yokoyama et al.*, 2002], topographic depressions [*Le and Kumar*, 2014], channel network [*Passalacqua et al.*, 2010; *Pelletier*, 2013; *Clubb et al.*, 2014], and wet channels [*Hooshyar et al.*, 2015].

The purpose of this research is to re-visit the drainage density and climate relationship by quantifying the drainage density in natural watersheds using LiDAR data. For this purpose, an

automatic procedure was developed to extract valley network based on 1 m resolution DEM obtained from LiDAR data.

2.2 Methodology

2.2.1 Study Sites and Data Sources

The Center for LiDAR Information, Coordination and Knowledge (CLICK) distributes data tiled by USGS Quarter Quadrangles in LAS and ASCII formats [*Stoker et al.*, 2006]. The LiDAR data were acquired through the CLICK website (http://lidar.cr.usgs.gov). The blue area in Figure 2-2 shows the LiDAR data availability. Red dots show the selected study sites with minimum human interference such as land use change, reservoir, and road construction. The study sites were located in 17 states with various climate conditions. The ground returns of LiDAR data, in which vegetation and buildings are removed by the data provider, were used in this study. The point cloud data were processed to derive 1 m DEM and land surface topography using QCoherent software LP360 for ArcGIS.
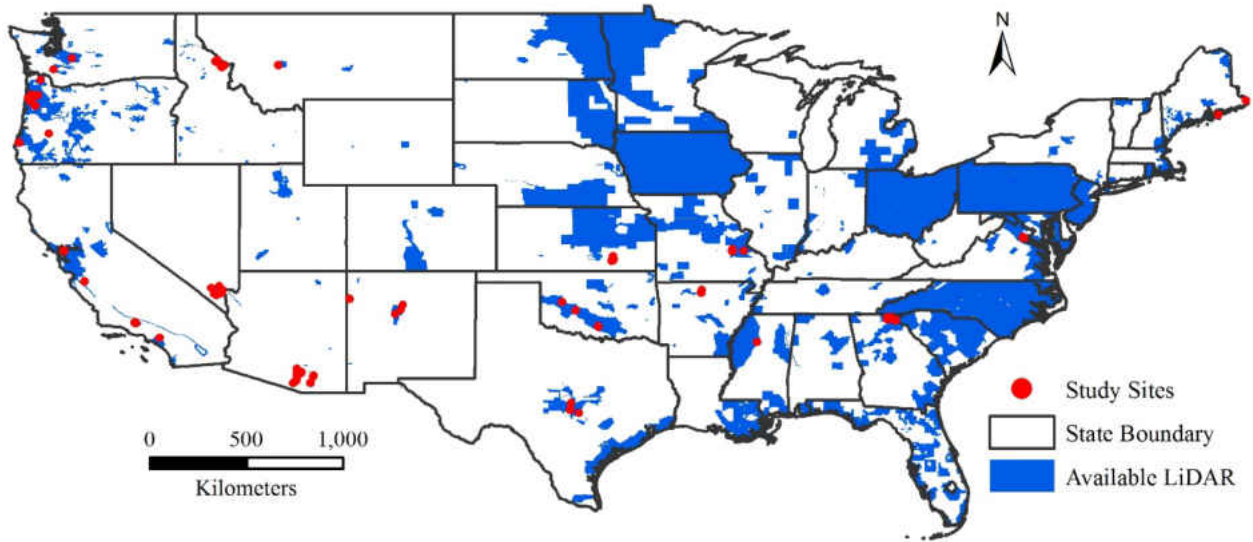
Figure 2-2: Location of study sites and available LiDAR data.

Climate aridity index, defined as the ratio of potential evaporation to precipitation (E_P/P), was used as an indicator of the climate [*Budyko*, 1958; 1974]. This index provided a useful tool to differentiate energy-limited or humid regions, ($E_P/P < 1$) and water-limited or arid regions ($E_P/P > 1$). Monthly potential evaporation data at 8 km spatial resolution, computed by the Priestley-Taylor method [*Priestley and Taylor*, 1972], were obtained from [*Zhang et al.*, 2010] and aggregated into mean annual values. The parameter-elevation regressions on independent slopes model (PRISM) provided the gridded annual, monthly and event-based precipitation data [*Daly et al.*, 1994]. Mean annual precipitation data from PRISM with 4 km spatial resolution for each watershed were used for the period of 1981-2010. Mean annual potential evaporation and precipitation data were averaged to the watershed scale values for computing E_P/P. E_P/P for the selected study watersheds ranged from 0.3 (humid) to 10.4 (arid). The list of all study watershed is given in Table 2-1 in Section 2.4.

For comparison, the *PE* index for the watersheds from *Melton* [1957] and *Madduma Bandara* [1974] were converted to E_P/P. When exploring the climate control on perennial stream density, *Wang and Wu* [2013] reported the inversely monotonic relationship between *PE* index and E_P/P based on 160 watersheds with *PE* < 500. The relationship between *PE* index and E_P/P was derived after removing the outliers from the data by *Wang and Wu* [2013] as shown in Figure 2-3 and is given in Equation (2-1):

$$PE = 176.34 \ E_P/P^{\ -1.224} \tag{2-1}$$

Lower E_P/P indices corresponded to higher *PE* indices. Abraham's curve was regenerated by converting the x-axis from *PE* to E_P/P using Equation (2-1). The U-shaped trend of original Abraham's curve was still visible after converting *PE* to E_P/P. The transition occurred when E_P/P is higher than 2.0. The mean annual rainfall was 640 ~595 mm at the minimum point in Figure 2-4.
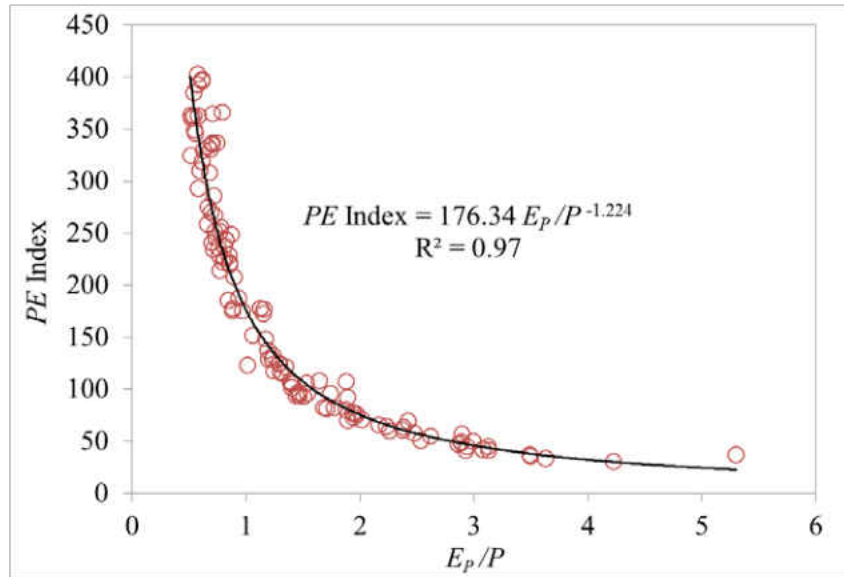
Figure 2-3: The correlation between *PE* index and climate aridity index (E_P/P).
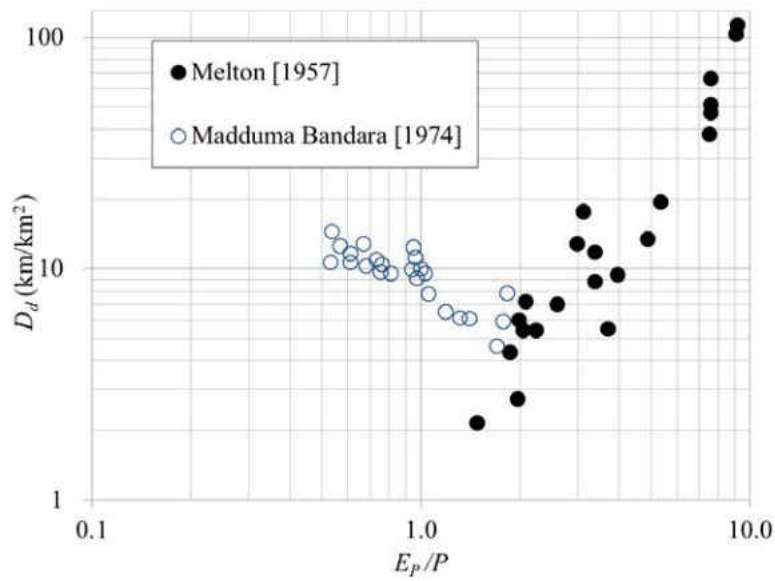
Figure 2-4: Drainage density (D_d) as a function of climate aridity index (E_P/P).

2.2.2 Extracting Valley Network

In this study, the valley network was extracted using a curvature-based method by incorporating both positive and negative curvature information. Curvature-based methods for valley or channel network delineation usually need filtering to reduce noise and insignificant features to obtain a robust curvature grid. Several filtering techniques have been applied for this purpose including Gaussian filter [*Lashermes et al.*, 2007], Perona-Malik filter [*Passalacqua et al.*, 2010], and Optimal Weiner filter [*Pelletier*, 2013]. Considering the robust performance of Perona-Malik filter [*Passalacqua et al.*, 2010; *Passalacqua et al.*, 2012; *Passalacqua and Foufoula-Georgiou*, 2015], we chose this filtering technique. Perona-Malik is a nonlinear diffusive filter that efficiently smooths the DEM while preserving the significant features such as valleys and banks. This filter has one parameter called "time of forward diffusion", which is denoted as T_F and was set to 50 for the study. From the filtered DEM, the curvature was calculated using the following equation [*Mitášová and Hofierka*, 1993]:

$$\kappa = \frac{z_{xx}z_y{}^2 - 2z_{xy}z_xz_y + z_{yy}z_x{}^2}{\left(z_x{}^2 + z_y{}^2\right)\sqrt{1 + z_x{}^2 + z_y{}^2}} \tag{2-2}$$

where κ is the curvature, and z_x and z_{xx} (z_y and z_{yy}) denote the first and second derivatives of elevation (z) with respect to x (y). z_{xy} is the first derivative of z_x with respect to y. Figure 2-5 shows the curvature extracted from original and filtered DEM along with contour lines of a tributary in a study site located in New Mexico.
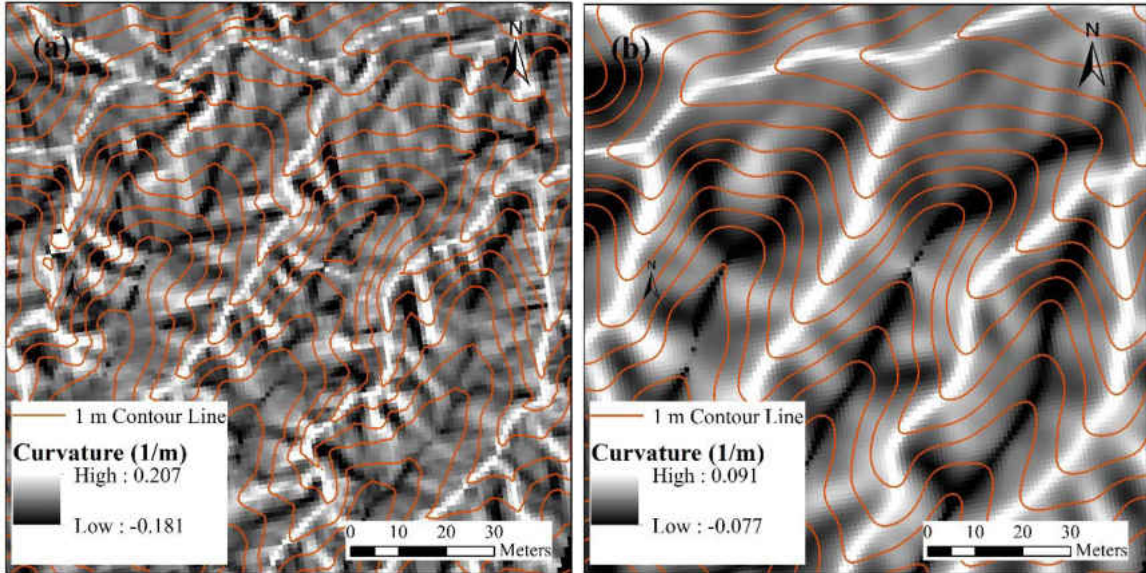
Figure 2-5: 1-m contour lines and the curvature grid for (a) the original DEM; and (b) the smoothed DEM after applying Perona-Malik filter ($T_F = 50$) on # 88 study site located in New Mexico.

Valley network extraction was based on the curvature analysis using positive and negative curvature as indicators of the significance of convergence or divergence. Valleys were defined as convergent surfaces which were associated with positive curvature. Ridges were the segments with negative curvature (i.e., divergent surface) which were typically located between the valleys and were the signature of flow separation lines between tributaries.

In order to differentiate valleys, a positive curvature threshold (κ_v) was automatically derived which was used to cluster the landscape into, convergent ($\kappa > \kappa_v$), divergent ($\kappa < -\kappa_v$), and insignificant ($|\kappa| \le \kappa_v$) pixels. κ_v was calculated through connected component analysis on the curvature grid. Figure 2-6 shows the number of connected component (N_{cc}) for any given curvature threshold, denoted by κ_T. A connected component was a set of connected pixels which are all either convergent or divergent. In order to find N_{cc} for each value of κ_T, the territory was

clustered into convergent (curvature greater than κ_T) and divergent (curvature less than $-\kappa_T$) pixels and then the connected component were counted using a binary labeling algorithm [*Suzuki et al.*, 2003]. As shown in Figure 2-6, decreasing κ_T initially led to more connected components since there were more pixels labeled as convergent or divergent. However, at some point the number of connected components dropped due to the merging process. In other words, the existing components started to merge together resulting in less N_{cc}. The peak of the connected component curve was considered as the curvature threshold for valley extraction since it produced the most separated clusters in the landscape and efficiently identified the local optimums in the curvature grid.
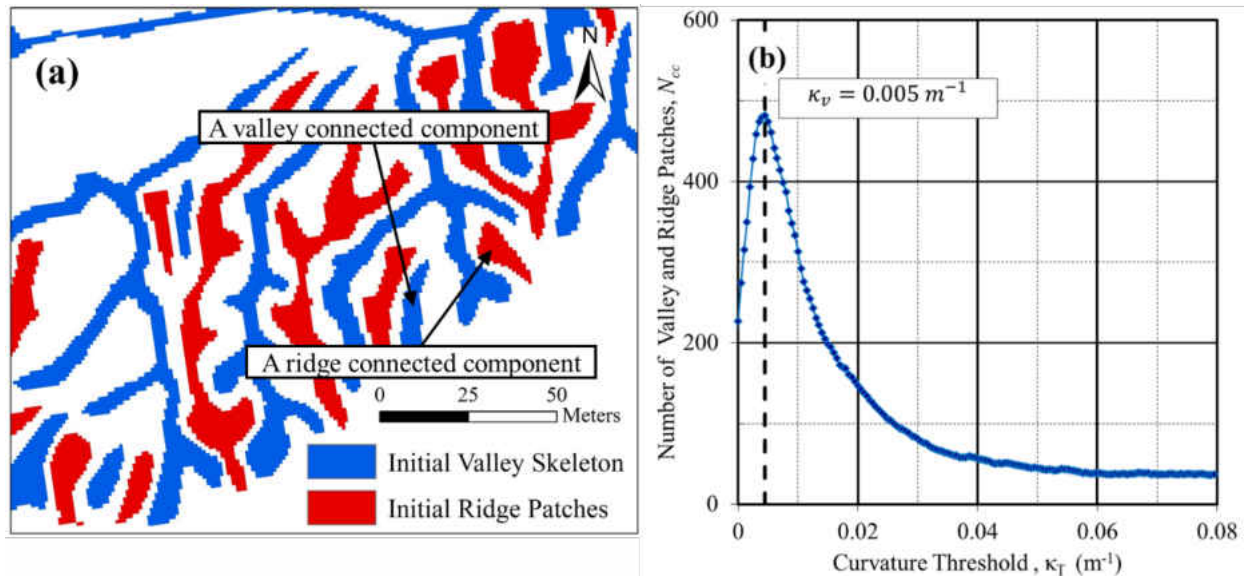
Figure 2-6: (a) Examples of valley and ridge connected components (b) Number of valley and ridge connected component (N_{cc}) vs. curvature threshold (κ_T) in # 88 study site located in New Mexico. The peak value represents the transition from insignificant to significant convergence/divergence features ($\kappa_v = 0.005$ m^{-1}).

Given the obtained κ_v, the initial valley skeleton was generated by imposing $\kappa > \kappa_v$ on the curvature grid. The skeleton was thinned to form a 1-pixel wide valley line. Afterwards, any two

neighboring valleys were checked for existence and at least one ridge (patches with $\kappa < -\kappa_v$) between them. Following this step, only valleys with well-defined banks (reflected as negative curvature patches in the curvature grid) over at least part of their length were kept and the rest were eliminated.

The resulting valley network was further processed to connect isolated valleys when the length of the gap is less than $0.25l_v$, where l_v was the total length of upstream isolated segment. Additionally, the valley network was manually edited based on the 1 m contour to get the best possible accuracy and minimize the effects of missing data and human-made structures such as roads. Figure 2-7a shows the contour curvature image computed from the filtered DEM and Figure 2-7b shows the valley networks delineated using the discussed valley extraction method in # 88 study site located in New Mexico.
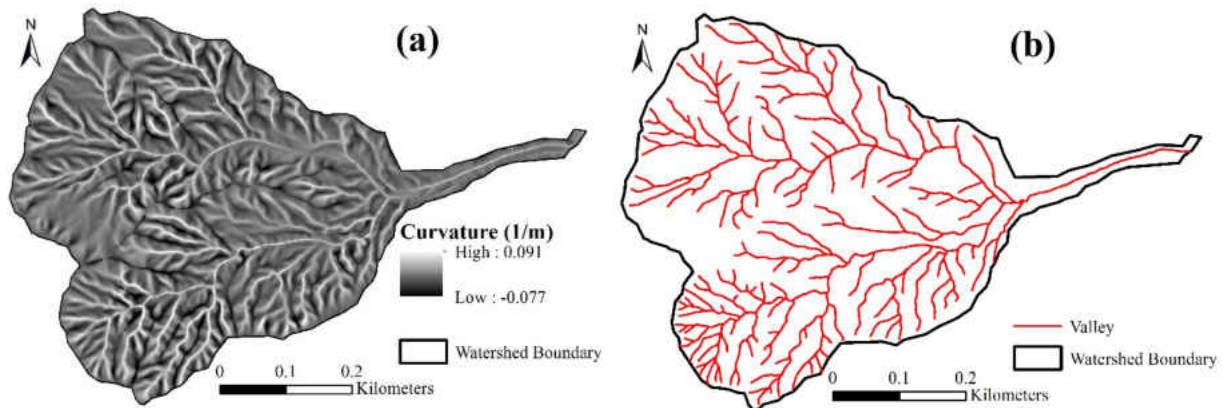
Figure 2-7: (a) Contour curvature computed from the filtered DEM; (b) Extracted valley network based on the curvature threshold in #88 study site located in New Mexico.

2.3 Results and Discussion

2.3.1 Drainage Density versus E_P/P

The valley networks for all the study watersheds were extracted based on 1 m DEM derived from LiDAR data. Figure 2-8 shows the distribution of E_P/P, drainage area (km^2) and drainage density (km/km^2) for the 121 study watersheds. The distribution was represented by normalized frequency, which was defined as the ratio of the number of watersheds in each bin to the total number of watersheds. The values of E_P/P varied from 0.3 to 10.4, and there were no study watersheds located in the range from 5.2 to 7.6 due to the unavailability of LiDAR data. The drainage area of most watersheds was less than 3 km^2, and the average drainage area was 1.31 km^2, with the minimum of 0.04 km^2 and the maximum of 8.19 km^2. The range of D_d was from 6.2 km/km^2 to 41.5 km/km^2. The stream order, location, drainage area, E_P/P, stream length and drainage density (D_d) for each watershed are listed in Table 2-1.
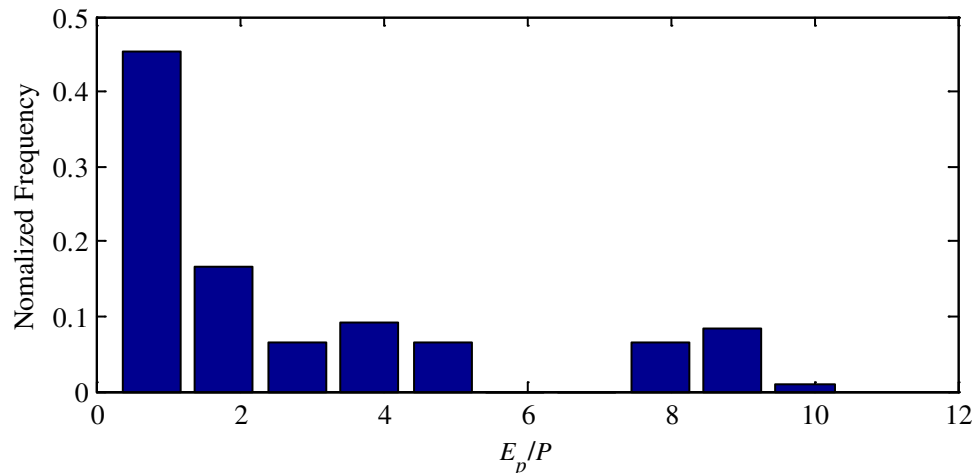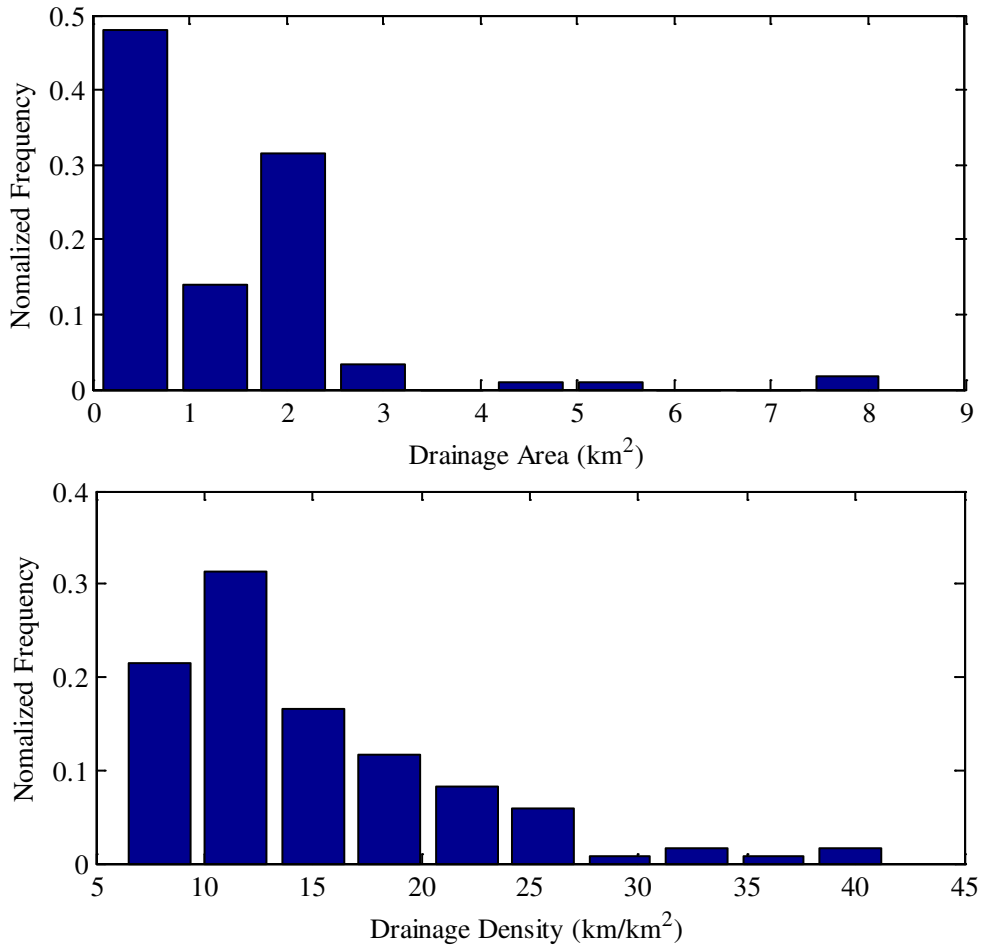
Figure 2-8: Normalized frequency distribution of E_p/P, drainage area (km^2) and drainage density (km/km^2) for the study watersheds.

Table 2-1: Index, location, drainage area, climate aridity index (E_P/P), precipitation (P), stream order, total drainage length, and drainage density for study sites.

Index	State	Drainage Area [km^2]	E_p/P	P [mm]	Stream Order	Total Drainage Length [km]	Drainage Density [km/km^2]
1	Arizona	0.36	4.3	299	4	8.2	23.1
2	Arizona	0.17	4.0	333	4	4.2	24.9
3	Arizona	0.66	4.3	306	5	16.2	24.7

Index	State	Drainage Area [km^2]	E_p/P	P [mm]	Stream Order	Total Drainage Length [km]	Drainage Density [km/km^2]
4	Arizona	0.33	4.4	291	4	4.7	14.0
5	Arizona	0.45	4.5	285	4	6.5	14.4
6	Arizona	0.39	4.0	321	3	6.1	15.5
7	Arizona	0.67	4.1	316	4	10.3	15.4
8	Arizona	0.61	4.1	316	5	11.2	18.3
9	Arizona	0.28	4.1	314	4	4.9	17.9
10	Arizona	0.65	3.0	447	3	8.3	12.8
11	Arizona	0.58	3.0	447	4	6.7	11.5
12	Arizona	0.62	3.3	405	4	9.4	15.2
13	Arizona	2.24	2.6	524	5	44.3	19.8
14	Arizona	0.13	5.1	244	4	3.8	29.0
15	Arizona	0.31	5.1	242	4	7.0	22.8
16	Arizona	0.39	4.6	275	4	8.1	20.7
17	Arizona	0.29	4.4	292	4	5.8	19.8
18	Arizona	0.25	2.7	496	3	3.8	15.2
19	Arkansas	2.43	1.1	1,194	5	25.6	10.6
20	Arkansas	2.00	1.1	1,187	4	17.4	8.7
21	California	0.83	3.0	456	4	12.1	14.5
22	California	1.38	2.4	633	5	19.9	14.4
23	California	0.53	3.4	428	4	9.9	18.5
24	California	2.01	1.8	840	4	23.4	11.7
25	California	2.08	1.8	828	4	24.3	11.7
26	California	1.27	2.1	722	4	18.4	14.5
27	California	2.09	2.1	722	4	23.3	11.1
28	California	2.47	2.1	640	5	27.7	11.2
29	California	2.10	2.1	634	5	25.6	12.2
30	California	2.02	2.3	586	5	28.0	13.9
31	Georgia	2.19	0.8	1,666	4	24.0	11.0
32	Georgia	2.21	0.7	1,739	4	24.9	11.3
33	Georgia	7.45	0.7	1,819	5	45.9	6.2
34	Georgia	5.05	0.8	1,564	5	37.8	7.5
35	Georgia	4.30	0.8	1,588	5	30.6	7.1
36	Georgia	8.19	0.7	1,900	5	52.4	6.4
37	Georgia	1.50	0.7	1,868	3	11.1	7.4
38	Georgia	0.94	0.9	1,500	4	7.5	8.0

Index	State	Drainage Area [km^2]	E_p/P	P [mm]	Stream Order	Total Drainage Length [km]	Drainage Density [km/km^2]
39	Georgia	0.75	0.8	1,588	4	7.9	10.5
40	Georgia	2.02	0.8	1,673	5	28.6	14.2
41	Georgia	2.14	0.8	1,657	5	33.0	15.4
42	Georgia	2.10	0.8	1,631	4	28.4	13.5
43	Idaho	2.93	0.9	1,028	4	26.0	8.9
44	Idaho	2.02	1.0	976	4	16.6	8.2
45	Idaho	2.92	0.7	1,402	4	30.2	10.3
46	Idaho	2.00	0.7	1,402	4	19.9	9.9
47	Idaho	2.32	0.7	1,297	4	18.8	8.1
48	Idaho	2.00	0.8	1,236	4	18.8	9.4
49	Idaho	1.68	0.8	1,249	4	15.7	9.3
50	Idaho	2.00	0.7	1,321	4	12.6	6.3
51	Idaho	2.33	0.6	1,521	5	19.4	8.3
52	Idaho	2.11	0.7	1,394	4	18.5	8.8
53	Idaho	1.95	0.7	1,289	4	14.7	7.5
54	Kansas	2.01	1.3	955	4	14.6	7.3
55	Kansas	1.88	1.3	974	5	18.7	10.0
56	Kansas	1.82	1.3	971	4	16.7	9.2
57	Kansas	1.34	1.3	956	4	13.3	10.0
58	Maine	0.48	0.8	1,223	4	6.4	13.5
59	Maine	0.54	0.7	1,352	4	4.3	8.0
60	Mississippi	0.59	0.9	1,438	4	7.5	12.5
61	Missouri	2.02	1.1	1,155	5	38.9	19.2
62	Missouri	0.41	1.1	1,155	4	8.8	21.4
63	Missouri	0.23	1.1	1,155	4	4.7	21.0
64	Missouri	1.91	1.0	1,169	5	43.2	22.6
65	Missouri	1.96	1.1	1,146	5	28.7	14.7
66	Missouri	1.00	1.1	1,118	4	13.6	13.7
67	Montana	1.37	2.1	436	4	12.8	9.3
68	Montana	2.01	2.1	438	4	14.2	7.1
69	Nevada	0.59	8.1	145	4	10.7	18.1
70	Nevada	0.20	10.4	120	4	3.7	18.3
71	Nevada	0.55	9.3	125	4	13.1	23.8
72	Nevada	0.39	9.2	127	4	7.8	20.1
73	Nevada	0.49	9.2	127	4	12.7	25.8

Index	State	Drainage Area [km²]	E_p/P	P [mm]	Stream Order	Total Drainage Length [km]	Drainage Density [km/km²]
74	Nevada	0.90	8.8	132	4	18.9	21.0
75	Nevada	0.40	8.2	141	4	10.4	26.2
76	Nevada	2.04	8.8	133	6	38.2	18.7
77	Nevada	0.30	7.7	155	3	3.3	11.0
78	Nevada	0.28	7.9	150	4	4.3	15.0
79	Nevada	0.27	8.8	134	4	4.8	17.7
80	Nevada	0.08	8.6	138	3	1.3	16.8
81	Nevada	0.15	8.3	144	4	3.4	23.2
82	Nevada	0.10	8.3	144	4	3.5	34.5
83	Nevada	0.23	8.6	138	4	5.5	23.7
84	Nevada	0.21	8.7	138	4	5.6	26.8
85	Nevada	0.10	8.3	142	4	3.2	31.3
86	Nevada	0.04	8.3	142	3	1.2	31.3
87	Nevada	0.25	9.0	131	4	6.3	25.2
88	New Mexico	0.24	4.6	271	5	9.8	41.5
89	New Mexico	1.96	3.6	339	6	40.1	20.5
90	New Mexico	1.61	3.4	363	5	30.9	19.1
91	New Mexico	0.26	2.9	425	4	4.7	17.7
92	New Mexico	0.04	4.7	261	4	1.4	38.2
93	Oklahoma	0.56	1.4	984	3	6.2	11.1
94	Oklahoma	0.61	1.7	812	4	8.3	13.5
95	Oklahoma	0.74	1.7	785	4	8.7	11.7
96	Oklahoma	2.35	1.4	978	4	31.0	13.2
97	Oregon	3.01	0.7	1,773	5	27.2	9.0
98	Oregon	0.21	0.6	1,789	3	2.5	11.5
99	Oregon	0.38	0.5	2,142	4	3.8	10.1
100	Oregon	0.13	0.3	3,589	3	1.1	8.4
101	Oregon	0.39	0.5	1,597	3	4.7	12.3
102	Oregon	0.41	0.3	3,685	4	4.4	10.7
103	Oregon	1.16	0.3	3,839	5	9.2	7.9
104	Oregon	0.97	0.4	2,764	4	12.6	13.0
105	Oregon	0.79	0.3	3,050	3	8.2	10.4
106	Oregon	0.91	0.3	2,992	4	11.7	12.8
107	Oregon	0.84	0.5	1,973	4	12.8	15.1
108	Oregon	0.98	0.5	1,919	4	12.1	12.3

Index	State	Drainage Area [km²]	E_p/P	P [mm]	Stream Order	Total Drainage Length [km]	Drainage Density [km/km²]
109	Texas	0.19	1.8	815	3	1.6	8.3
110	Texas	1.62	2.0	760	4	16.8	10.3
111	Texas	2.66	2.0	755	4	35.9	13.5
112	Texas	1.17	2.0	735	4	11.8	10.1
113	Virginia	2.25	1.0	1,064	4	23.2	10.3
114	Virginia	1.51	0.9	1,061	5	18.8	12.5
115	Virginia	2.10	0.6	1,061	5	20.7	9.9
116	Virginia	2.01	1.0	1,065	4	23.7	11.8
117	Virginia	1.03	1.0	1,064	4	11.4	11.0
118	Virginia	2.03	1.0	1,063	4	21.1	10.4
119	Virginia	2.09	1.0	1,062	4	21.1	10.1
120	Washington	0.59	0.3	3,308	4	3.8	6.4
121	Washington	0.26	0.7	1,285	4	3.3	13.0

The relationship between E_P/P and mean annual precipitation (MAP) for the study watersheds is shown in Figure 2-9. Higher MAP corresponded to lower E_P/P. The correlation coefficient between MAP and E_P/P was -0.99.
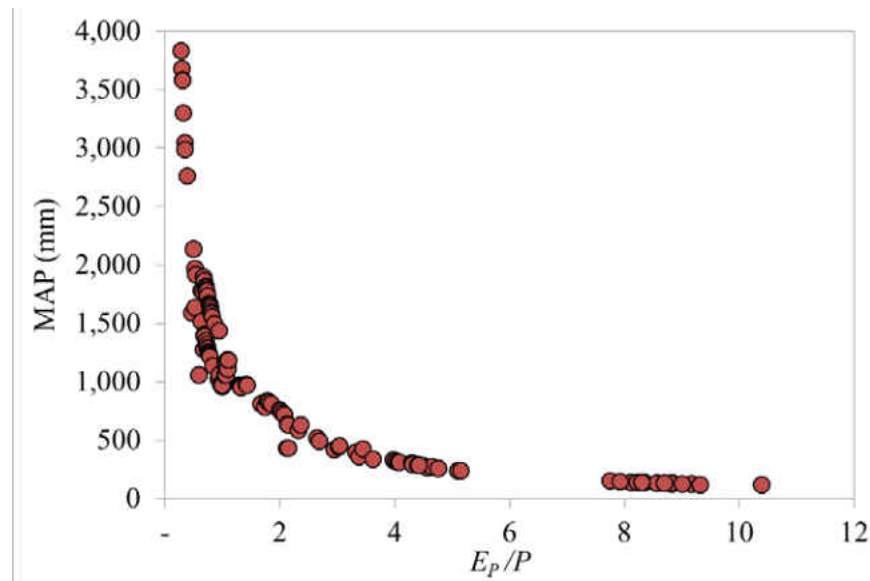
Figure 2-9: The correlation between Mean Annual Precipitation (MAP) and E_P/P for the 121 study watersheds.

Figure 2-10 shows the comparison between the obtained results from this study and the reported data by *Melton* [1957] and *Madduma Bandara* [1974]. When E_P/P was less than 1, the data points by *Madduma Bandara* [1974] showed a decreasing trend for D_d; while such a declining trend did not exist for the watersheds in this study. The decreasing trend by *Madduma Bandara* [1974] continued until E_P/P reaches ~1.8. This discrepancy can be explained by the land use in Madduma Bandara's watersheds, in which the natural land cover has been consistently converted to tea plantation over the past 100 years. Thus, the drainage density has been modified by human interventions.

When E_P/P is between 1 and 6, the drainage densities from both *Melton* [1957] and this study showed increasing trends with E_P/P. However, the magnitude of D_d was higher than those from *Melton* [1957] due to the resolution of topographic maps. The topographic maps with scales

1:24,000 were used for extracting drainage network by *Melton* [1957] for watersheds with E_P/P less than 6. These topographic maps with bare-earth contours were equivalent with DEM at a grid cell size of 30 m [*Kosovich et al.*, 2008], from which small valleys were not detectable. Therefore, the drainage density was underestimated. However, 1 m DEM from LiDAR data was used in this study. This discrepancy in map resolution can create significant differences between valleys mapped in field and extracted from topographic maps [*Morisawa*, 1957; *Schneider*, 1961]. To demonstrate the effect of DEM resolution on drainage density, 1 m DEMs for the study watersheds were resampled to 30 m DEM for generating drainage network. 20 watersheds with E_P/P less than 6 and drainage area larger than 0.2 km^2 were selected. As shown in Figure 2-11, D_d from 1 m DEM was higher than that from 30 m DEM. As a demonstration, Figure 2-12 shows the extracted valley lines from 1 m DEM and 30 m DEM for a watershed from New Mexico.
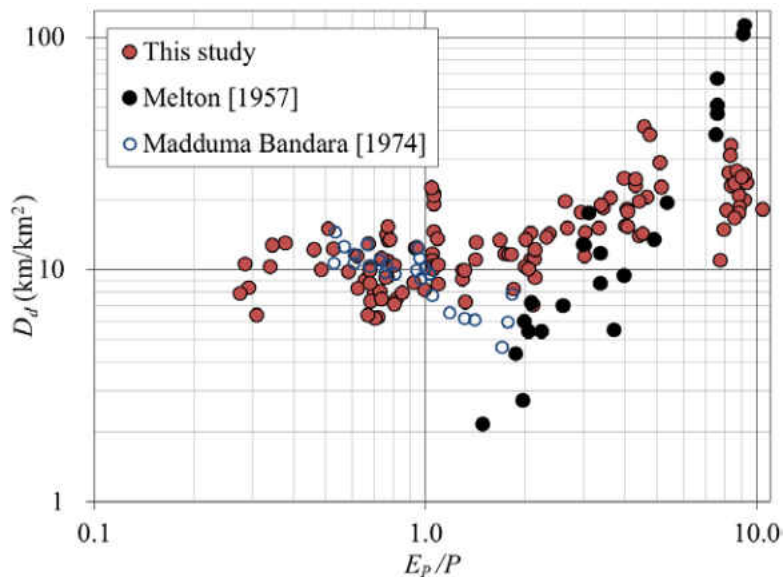
Figure 2-10: Comparison of study watersheds and Abrahams curve (1984) of drainage density (D_d) as a function of climate aridity index (E_P/P).

When E_P/P is larger than 7, the drainage densities from *Melton* [1957] were higher than those in this study (Figure 2-10). These catchments were located in Arizona: two within the Chinle watershed in Cameron, and four within Saguaro National Monument in Tucson. The valley network in these 6 catchments were mapped by field survey. The climate aridity index in the Chinle watershed was 9.0 and D_d is over 100 km/km^2. The valleys in this watershed were mapped by *Schumm* [1956]. The drainage area for the two catchments in Chinle watershed, with fully developed micro-relief, was about 0.0023 km^2 [*Melton*, 1957]. The climate aridity index in the Saguaro National Monument catchments was around 7.5 and the valleys were mapped by *Melton* [1957]. These four catchments were bordered with an average drainage area of 0.013 km^2. The small drainage area of these 6 catchments also contributed to the high drainage density.
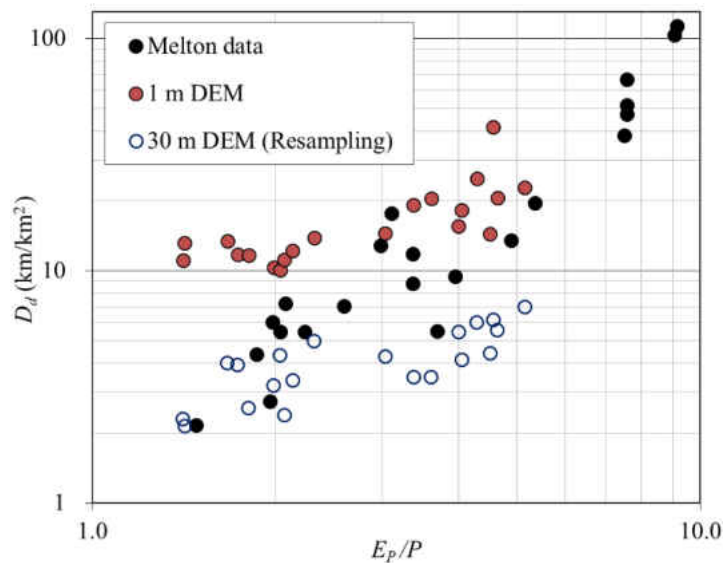
Figure 2-11: Comparison of drainage density (D_d) from 1 m DEM derived by LiDAR data and 30 m DEM using resampling method.
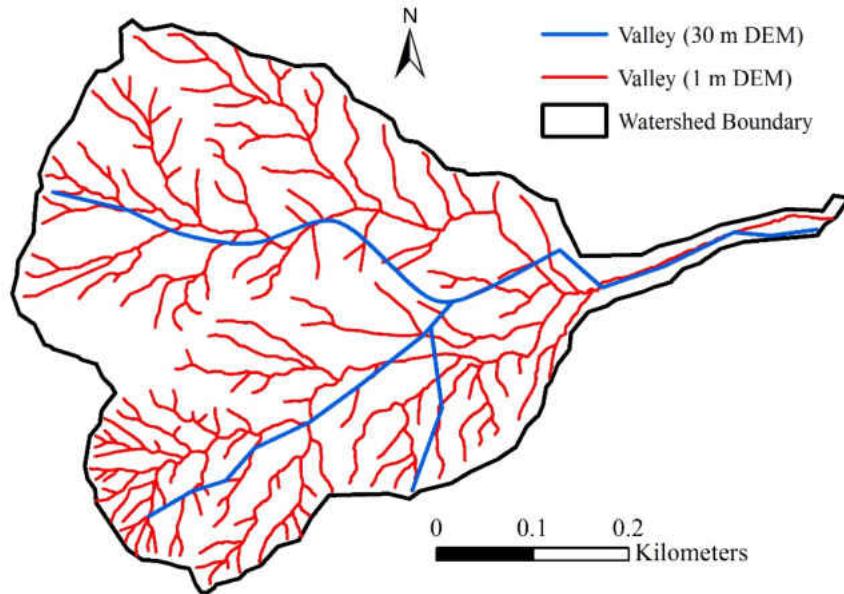
Figure 2-12: Comparison of valley lines from 1 m DEM derived by LiDAR data and 30 m DEM by resampling on #88 study site located in New Mexico.

2.3.2 Drainage Density versus Drainage Area

Besides climate, relationships between drainage area (*A)* and D_d was also reported. *Gregory and Walling* [1973] showed an inverse relationship between D_d and *A*. *Pethick* [1975] presented $D_d = 6.6\,A^{-0.337}$ for 228 watersheds over different climates even though the general consensus was that D_d is independent of *A*.

To demonstrate the influence of drainage area on D_d, Figure 2-13 plots the relationship between D_d and drainage area for: a) 124 watersheds in arid climate from *Melton* [1957]; and b) 121 watersheds from both humid and arid climates in this study. There was a strong negative

37

correlation between drainage density and drainage area for both datasets. The data points in Figure 2-13b are more scattered due to different climates such as the watersheds from humid regions.
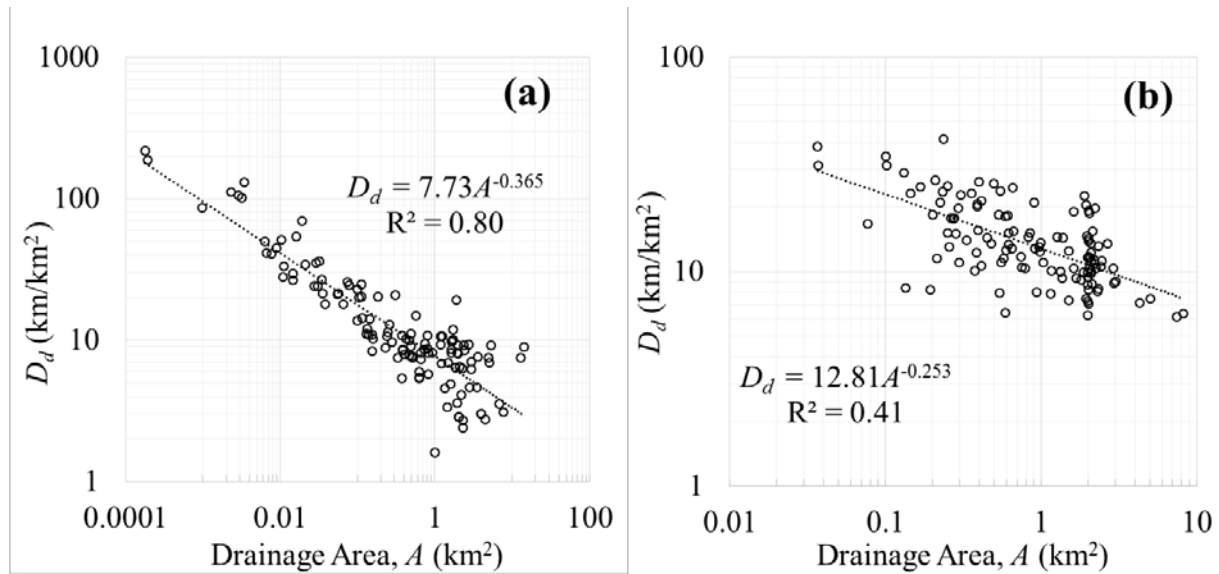
Figure 2-13: The relationship between drainage density (D_d) and drainage area: (a) 124 watersheds in arid climate from *Melton* [1957]; and (b) 121 watersheds from humid to arid climate in this study.

To investigate the climate effect on the relationship between D_d and A, the study watersheds were categorized into two groups: 1) humid ($E_P/P < 1$) and arid ($E_P/P \geq 1$). Figure 2-14 shows the relationship between D_d and A for humid regions (Figure 2-14a) and arid regions (Figure 2-14b). The relationship in humid region was not clear but showed an inverse pattern in arid region. Based on the result, D_d was related to A in arid regions.
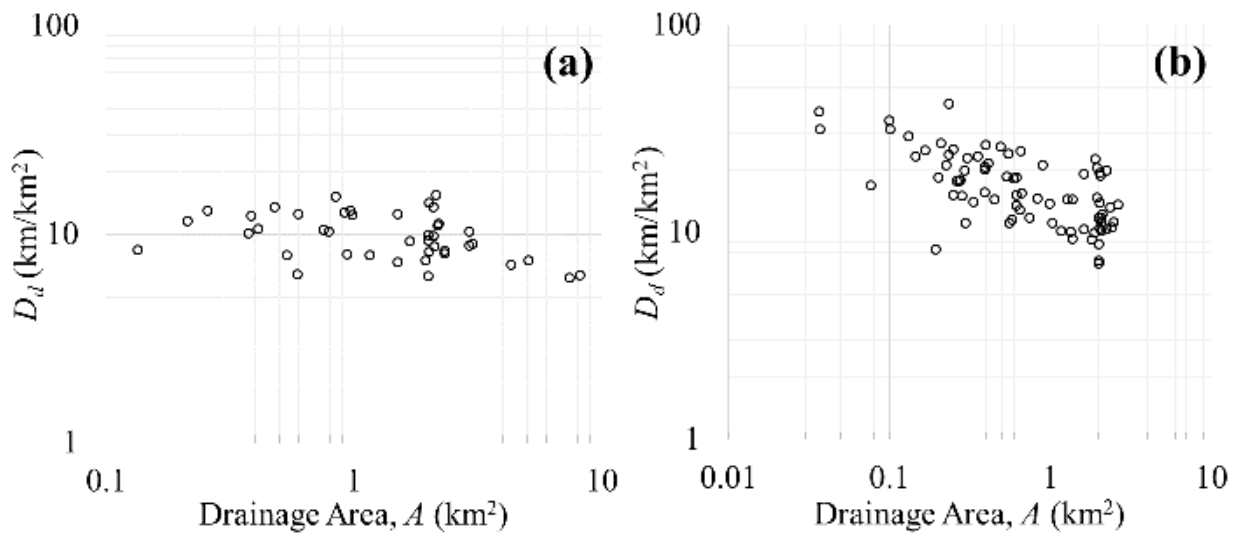
Figure 2-14: The relationship between drainage density (D_d) and drainage area from this study watersheds: (a) 42 watersheds for humid region (E_P/P less than 1); and (b) 79 watersheds for arid region (E_P/P larger than 1).

To better understand the effect of drainage area on D_d, 30 watersheds were selected in our study sites with different climate and each watershed were divided into 3~8 subwatersheds. Taking the study site #88 located in New Mexico as an example, three subwatersheds were delineated as shown in Figure 2-15. The maximum stream order of all subwatersheds was larger than 3 and the range of subwatershed area was 0.01~2.93 km². Figure 2-16 shows the pattern of D_d corresponding to E_P/P; Figure 2-16a shows average, minimum and maximum D_d in terms of subwatersheds with different watershed areas in the selected 30 study sites. The variation of D_d was small in humid regions but large in arid regions. Standard deviation of D_d for subwatersheds in each study site showed an increase pattern in terms of E_P/P in Figure 2-16b. However, the

variation of D_d for some watersheds in arid regions was small because D_d is affected by climate as

well as other controlling factors such as soil, vegetation and topography [*Gardiner et al.*, 1977].
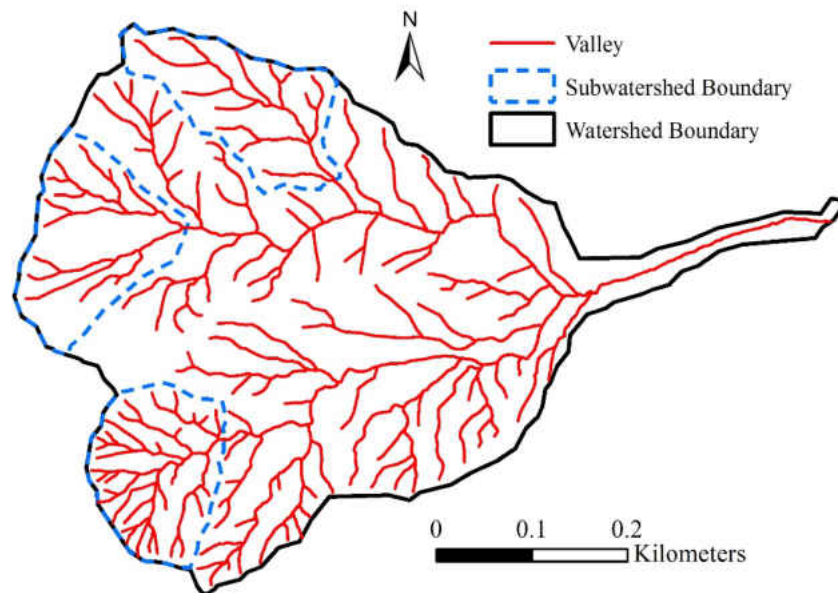
Figure 2-15: Extracted subwatersheds with different watershed areas in the study site #88 located in New Mexico.
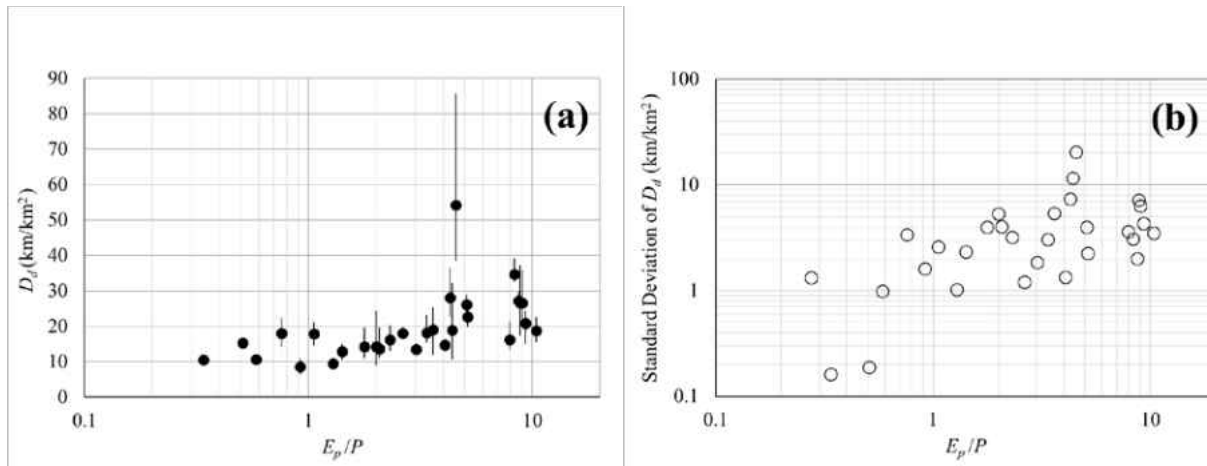
Figure 2-16: The relationship between drainage density (D_d) and climate aridity index (E_P/P): (a) Average, minimum and maximum D_d in terms of subwatersheds with different watershed area in the selected 30 study sites; and (b) Standard deviation of D_d versus E_P/P.

2.4 Conclusion

The aim of this study was to investigate the climate controls on drainage density. 121 watersheds with minimal to no anthropogenic intervention were selected based on LiDAR data availability. Climate aridity index (E_P/P) was used as a quantitative indicator for climate. The range of E_P/P for the study watersheds was from 0.3 (humid) to 10.4 (arid). Using the topographic curvature threshold developed by *Hooshyar et al.* [2016], valley networks were extracted from 1 m DEM derived by LiDAR data and drainage density of each watershed was calculated. The relationship between climate and drainage density was also re-visited. Compared with the U-shape relationship from *Melton* [1957] and *Madduma Bandara* [1974], the results showed a monotonic increasing trend. This discrepancy is explained by two reasons: 1) watersheds from

Madduma Bandara [1974], located in humid regions, were modified by extensive human interventions because the natural vegetation has been converted to tea plantation; 2) the drainage density for watersheds from *Melton* [1957] was underestimated when the drainage networks were extracted from topographic maps with a scale of 1:24,000.

The relation between D_d and A was also investigated and the results showed a negative correlation. The impact of drainage area on D_d was small in humid regions, but significant in arid regions. However, some watersheds in arid region were not affected by drainage area because other environment effects such as soil, rock type, topography and vegetation were also important.

2.5 <u>References</u>

Abrahams, A. D. (1984), Channel networks: a geomorphological perspective, *Water Resources Research*, *20*(2), 161-188.

Booth, A. M., J. J. Roering, and A. W. Rempel (2013), Topographic signatures and a general transport law for deep-seated landslides in a landscape evolution model, *Journal of Geophysical Research: Earth Surface*, *118*(2), 603-624.

Bowen, Z. H., and R. G. Waltermire (2002), Evaluation of light detection and ranging (LIDAR) for measuring river corridor topography, *Journal of the American Water Resources Association*, *38*(1).

Budyko, M. I. (1958), *The heat balance of the earth's surface*, US Department of Commerce, Washington, DC.

Budyko, M. I. (1974), *Climate and Life*, 508 pp., Academic Press, New York.

Carlston, C. W. (1963), *Drainage density and streamflow*, US Govt. Print. Off.

Daly, C., R. P. Neilson, and D. L. Phillips (1994), A statistical-topographic model for mapping climatological precipitation over mountainous terrain, *Journal of applied meteorology*, *33*(2), 140-158.

Derron, M.-H., and M. Jaboyedoff (2010), Preface" LIDAR and DEM techniques for landslides monitoring and characterization", *Natural Hazards and Earth System Science*, *10*(9), 1877-1879.

Dune, T., and L. Leopold (1978), Water in environment planning, edited, Freeman: San Francisco.

Gardiner, V., K. Gregory, and D. Walling (1977), Further notes on the drainage density-basin area relationship, *Area*, 117-121.

Gregory, K. J., and D. E. Walling (1973), Drainage basin form and process: A geomorphological approach.

Hooshyar, M., S. Kim, D. Wang, and S. C. Medeiros (2015), Wet Channel Network Extraction by Integrating LiDAR Intensity and Elevation Data, *Water Resources Research*.

Hooshyar, M., D. Wang, S. Kim, S. C. Medeiros, and S. C. Hagen (2016), Valley and channel network extraction based on local topographic curvature and K-means, *Water Resources Research*, Under review.

Horton, R. E. (1932), Drainage-basin characteristics, *Eos, Transactions American Geophysical Union*, *13*(1), 350-361.

Horton, R. E. (1945), Erosional development of streams and their drainage basins; hydrophysical approach to quantitative morphology, *Geological society of America bulletin*, *56*(3), 275-370.

Howard, A. D. (1994), A detachment-limited model of drainage basin evolution, *Water resources research*, *30*(7), 2261-2285.

Jaboyedoff, M., T. Oppikofer, A. Abellán, M.-H. Derron, A. Loye, R. Metzger, and A. Pedrazzini (2012), Use of LIDAR in landslide investigations: a review, *Natural hazards*, *61*(1), 5-28.

Kosovich, J. J., R. W. Schaffranek, M. A. Stewart, D. J. Nowacki, J. R. Degnan, G. J. Walsh, S. Flanagan, and R. C. Burruss (2008), *State of Florida 1: 24,000-and 1: 100,000-Scale Quadrangle Index Map, Highlighting Low-lying Areas Derived from USGS Digital Elevation Models*, US Department of the Interior, US Geological Survey.

Lashermes, B., E. Foufoula-Georgiou, and W. E. Dietrich (2007), Channel network extraction from high resolution topography using wavelets, *Geophysical Research Letters*, *34*(23), L23S04.

Le, P. V., and P. Kumar (2014), Power law scaling of topographic depressions and their hydrologic connectivity, *Geophysical Research Letters*, *41*(5), 1553-1559.

Madduma Bandara, C. M. (1974), Drainage density and effective precipitation, *Journal of Hydrology*, *21*(2), 187-190.

Marks, K., and P. Bates (2000), Integration of high-resolution topographic data with floodplain flow models, *Hydrological Processes*, *14*(11-12), 2109-2122.

Melton, M. A. (1957), An analysis of the relations among elements of climate, surface properties, and geomorphology, DTIC Document.

Mitášová, H., and J. Hofierka (1993), Interpolation by regularized spline with tension: II. Application to terrain modeling and surface geometry analysis, *Math Geol*, *25*(6), 657-669.

Moglen, G. E., E. A. Eltahir, and R. L. Bras (1998), On the sensitivity of drainage density to climate change, *Water Resources Research*, *34*(4), 855-862.

Montgomery, D. R., and W. E. Dietrich (1988), Where do channels begin?, *Nature*, *336*(6196), 232-234.

Montgomery, D. R., and E. Foufoula-Georgiou (1993), Channel network source representation using digital elevation models, *Water Resources Research*, *29*(12), 3925-3934.

Morisawa, M. (1957), Accuracy of determination of stream lengths from topographic maps, *Eos, Transactions American Geophysical Union*, *38*(1), 86-88.

Passalacqua, P., and E. Foufoula-Georgiou (2015), Comment on "Objective extraction of channel heads from high-resolution topographic data" by Fiona J. Clubb et al, *Water Resources Research*, *51*(2), 1372-1376.

Passalacqua, P., P. Belmont, and E. Foufoula-Georgiou (2012), Automatic geomorphic feature extraction from lidar in flat and engineered landscapes, *Water Resources Research*, *48*(3).

Passalacqua, P., T. Do Trung, E. Foufoula-Georgiou, G. Sapiro, and W. E. Dietrich (2010), A geometric framework for channel network extraction from lidar: Nonlinear diffusion and geodesic paths, *Journal of Geophysical Research: Earth Surface*, *115*(F1), F01002.

Pelletier, J. D. (2013), A robust, two-parameter method for the extraction of drainage networks from high-resolution digital elevation models (DEMs): Evaluation using synthetic and real-world DEMs, *Water Resources Research*, *49*(1), 75-89.

Pethick, J. (1975), A note on the drainage density-basin area relationship, *Area*, 217-222.

Peucker, T. K., and D. H. Douglas (1975), Detection of surface-specific points by local parallel processing of discrete terrain elevation data, *Computer Graphics and image processing*, *4*(4), 375-387.

Priestley, C., and R. Taylor (1972), On the assessment of surface heat flux and evaporation using large-scale parameters, *Monthly weather review*, *100*(2), 81-92.

Schneider, W. J. (1961), A note on the accuracy of drainage densities computed from topographic maps, *Journal of Geophysical Research*, *66*(10), 3617-3618.

Schumm, S. A. (1956), Evolution of drainage systems and slopes in badlands at Perth Amboy, New Jersey, *Geological society of America bulletin*, *67*(5), 597-646.

Stoker, J. M., S. K. Greenlee, D. B. Gesch, and J. C. Menig (2006), CLICK: The new USGS center for lidar information coordination and knowledge, *Photogrammetric Engineering and Remote Sensing*, *72*(6), 613-616.

Suzuki, K., I. Horiba, and N. Sugie (2003), Linear-time connected-component labeling based on sequential local operations, *Computer Vision and Image Understanding*, *89*(1), 1-23.

Swisher, G. (2002), Southern Illinois University Carbondale Patent and Copyright Committee meeting, March 8.

Thornthwaite, C. W. (1931), The climates of North America: according to a new classification, *Geographical Review*, 633-655.

Wang, D., and L. Wu (2013), Similarity of climate control on base flow and perennial stream density in the Budyko framework, *Hydrol. Earth Syst. Sci.*, *17*(1), 315-324.

Yokoyama, R., M. Shirasawa, and R. J. Pike (2002), Visualizing topography by openness: a new application of image processing to digital elevation models, *Photogrammetric engineering and remote sensing*, *68*(3), 257-266.

Zhang, K., J. S. Kimball, R. R. Nemani, and S. W. Running (2010), A continuous satellite-derived global record of land surface evapotranspiration from 1983 to 2006, *Water Resources Research*, *46*(9).

CHAPTER 3: WET CHANNEL NETWORK IDENTIFICATION BASED ON INTENSITY OF LIDAR RETURNS

3.1 Introduction

Wet channel networks expand in response to rainfall events and contract during streamflow recession periods. The temporal and spatial dynamics of wet channel networks are one of the key features for revealing the links between hydrology and geomorphology driven by climate [*Abrahams*, 1984; *Wang and Wu*, 2013], mechanisms on individual hydrologic processes [*Biswal and Marani*, 2010], and stream ecosystem expansion and contraction [*Stanley et al.*, 1997]. Perennial streams have continuous flow during years of normal rainfall [*Meinzer*, 1923]. Temporal streams, including intermittent and ephemeral streams, are defined as waterways that cease flowing at some points in space and time along their course and support high biodiversity and important ecosystem processes [*Acuña et al.*, 2014]. The drying and wetting dynamics usually occur in temporal streams located in headwater catchments. Therefore, it will benefit both hydrology and stream ecology to understand and monitor these short-time changes in wet channel networks. However, the data availability on wetting and drying dynamics of ephemeral streams is limited. Reliable streamflow gauges operated by United States Geologic Survey (USGS) are generally sited on relatively large perennial streams and rivers [*EPA*, 2010].

Remotely sensed images from satellites have been used to identify the water surface of open water bodies and large rivers. Near-infrared (NIR) radiation is absorbed by water but reflected by vegetation and dry soil. This characteristic of NIR has been utilized to identify ponds and lakes [*Work and Gilmer*, 1976]. Based on the reflectance of water and vegetation to NIR and

green light, the normalized difference water index (NDWI) has been developed and used for differentiating water surface features from soil and vegetation [*McFeeters*, 1996; *Xu*, 2006]. *Beeson et al.* [2011] used night/day temperatures, as a proxy for soil moisture, from advanced spaceborne thermal emission and reflection radiometer (ASTER) images with 15 meter resolution to identify ephemeral and perennial stream reaches. Since headwater streams are typically narrower, shallower, and heavily vegetated, this presents a challenge in using satellite imagery to detect water surfaces due to the relatively low spatial resolution and vegetation interference.

Airborne light detection and ranging (LiDAR) provides an opportunity to map wet channel networks. LiDAR has become an important technique to acquire topographic data at sub-meter resolution and accuracy [*Marks and Bates*, 2000; *Bowen and Waltermire*, 2002] and has been utilized to extract channel networks [*Passalacqua et al.*, 2010; *Pelletier*, 2013] and topographic depressions [*Le and Kumar*, 2014] in the past. LiDAR has also been used to retrieve water surface information including flood inundation extent [*Genc et al.*, 2005] and water levels and gradients [*Magirl et al.*, 2005; *Hopkinson et al.*, 2011]. As an active remote sensing technique, the airborne LiDAR sensor emits NIR laser pulses with a wavelength of 1064 nm which cannot penetrate water. Most of the infrared laser light is effectively absorbed in the water column or reflected specularly away from the field of view of the discrete echo recording system [*Wolfe and Zissis*, 1993; *Brzank et al.*, 2008]. The signal intensity, which is a relative strength measurement of the return pulse by the LiDAR sensor, is lower from the water surface compared with land areas. The intensity characteristics of the water surface have previously been used to derive water-land boundaries in river segments [*Höfle et al.*, 2009]. With high airborne LiDAR acquisition altitudes and incidence angles, the intensities of water surface returns arriving at the receiver are too small to be detected.

Therefore, laser shot dropouts may occur and the point density is typically lower on water surfaces [*Höfle et al.*, 2009]. Even though bathymetric LiDAR using green and infrared spectrums has the ability to generate returns at both the water and bottom surfaces, point densities are still lower than those of topographic LiDAR over land, affecting the minimum detectable size of water body systems [*Hilldale and Raff*, 2008; *Mallet and Bretar*, 2009].

Intensity information from single wavelength topographic LiDAR (i.e., NIR) systems has been used to map many types of water surfaces including rivers, wetlands, ponds, and lakes [*Smeeckaert et al.*, 2013; *Wu et al.*, 2013; *Höfle et al.*, 2009]. *Antonarakis et al.* [2008] identified a water surface in a river segment when the height range of the returns is less than 0.5 m and an average intensity value in a local domain is less than a threshold. *Lang and McCarty* [2009] demonstrated the ability of LiDAR intensity data for mapping inundated areas beneath a forest canopy. *Brzank et al.* [2008] developed a supervised classification method for identifying laser points on the water surface of Wadden Sea using elevation, intensity, and 2D point density. These studies are successful in delineating water-land boundary of large continuous water areas (i.e., geometrical assessment of water bodies), including those with canopy issues.

The objective of this paper was to map wet channel networks using the elevation and intensity information in the point cloud generated by topographic LiDAR systems. Wet channels were identified along the channel network based on a statistical detection framework. Topographic LiDAR data with single wavelength NIR were used to identify dry or wet channels in headwater catchments, acting as an extension of previous work for water body identification. This topographic LiDAR data is now available to the public in many areas [*Stoker et al.*, 2006]. Lake Tahoe area was considered as the case study due to availability of high resolution LiDAR data

with intensity information and two data acquisitions (in separate years) in some watersheds. Based on the identified wet channel network, the relationship between streamflow and wet channel length was explored and evaluated. The developed method provides an opportunity to investigate wet channel network dynamics.

3.2 Study Sites and Data Sources

3.2.1 Study Sites

Lake Tahoe is located in the high mountain area at the state border of California and Nevada. The lake surface area is 496 km^2 and drainage area is 1,310 km^2 [*Dettinger*, 2013]. The Lake Tahoe drainage basin was formed by uplift creating the Carson Range on the east and the Sierra Nevada on the west with an average surface elevation of 1,897 m above mean sea level. The area has cold and wet winters with an average temperature of -1 ^{o}C in January, and warm and dry summers with an average temperature of 18 ^{o}C in June [*Taylor and Beaty*, 2005]. Mean annual precipitation is 1400 mm and 670 mm on the west and east sides of the lake, respectively. Precipitation mainly occurs as snow from November and April, and most runoff occurs during the spring snowmelt period from April to June [*Coats and Goldman*, 2001].

This study focused on five watersheds around Lake Tahoe as shown in Figure 3-1a. Four watersheds, including Blackwood Creek, Ward Creek, General Creek and Trout Creek, are located in California; Incline Creek is located in Nevada. There are two streamflow gages in the Incline Creek watershed as shown in Figure 3-1b, and the upstream and downstream gage identification numbers are 103366993 and 10336700, respectively. The human effects such as reservoir

51

operations and urbanization are minimal in these watersheds. The drainage area of the seven gages varies from 7.4 km^2 to 28.9 km^2 (Table 3-1). The climate aridity index, defined as the ratio of potential evaporation to precipitation, varies from 0.99 to 1.61 in these watersheds. Most of the watersheds are covered by intact forest and shrub area; as an example, the forest land is 70% and the shrub land is 28% in Blackwood Creek watershed.
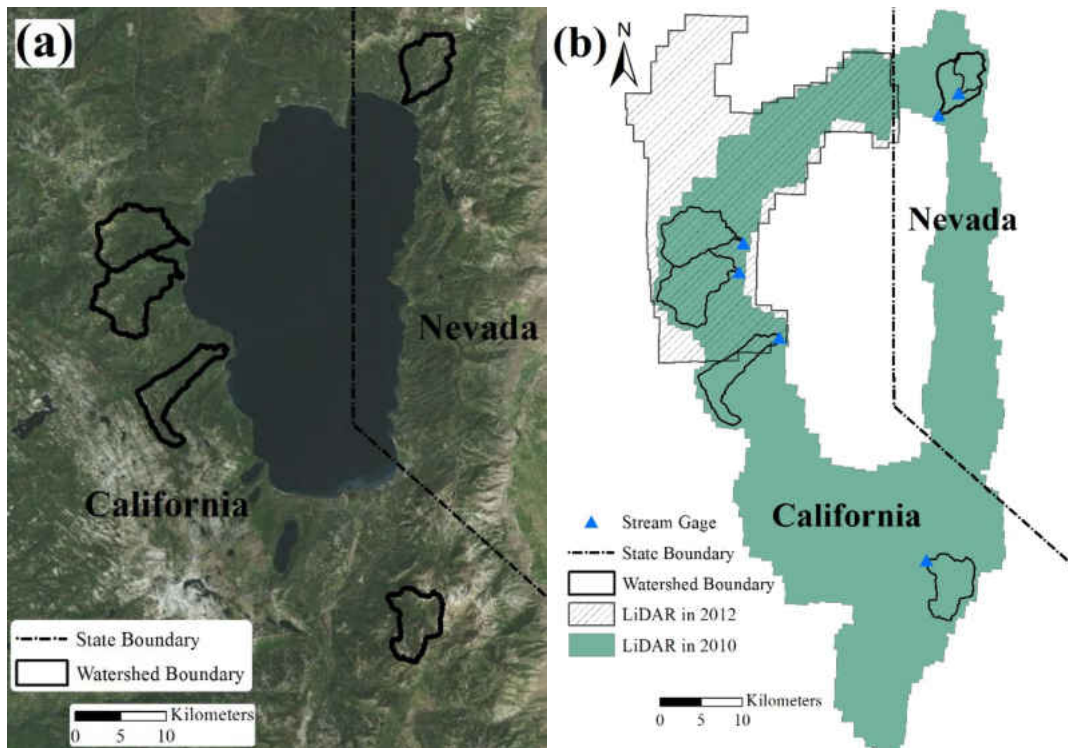
Figure 3-1: Map for the study sites: (a) five study watersheds around Lake Tahoe; and (b) six streamflow gages and the spatial coverage of LiDAR data sets.

Table 3-1: USGS gage identification number, drainage area, streamflow and its variations during the LiDAR surveys, and the corresponding exceedance probability for six streamflow gages.

Watershed	Gage Number	Drainage Area [km²]	LiDAR Acquisition Date	Streamflow [m³/s]	Streamflow Exceedance Probability [%]
Blackwood Creek, CA	10336660	28.9	8/20/2010-8/23/2010	0.10±0.01	73
			6/20/2012-6/21/2012	0.52±0.01	40
Ward Creek, CA	10336676	24.9	8/14/2010	0.06	72
			6/20/2012-6/21/2012	0.27±0.01	43
General Creek, CA	10336645	19.2	8/20/2010-8/23/2010	0.02	95
Trout Creek, CA	10336770	19.1	8/23/2010	0.16	54
Incline Creek, NV	10336700	17.3	8/12/2010	0.10	66
Incline Creek, NV	103366993	7.4	8/12/2010	0.04	74

3.2.2 LiDAR and Streamflow Data

These watersheds were selected for this study based on the availability of simultaneous streamflow observations and LiDAR data. Streamflow observations were obtained from the USGS National Water Information System and the gage identification numbers are shown in Figure 3-1b and Table 3-1. The Center for LiDAR Information, Coordination and Knowledge (CLICK) provided LiDAR data tiled by USGS Quarter Quadrangles in LAS and ASCII format [*Stoker et al.*, 2006]. The LiDAR data were obtained through the CLICK website (http://lidar.cr.usgs.gov, Last Accessed July 15, 2014). The bare earth LiDAR data, with vegetation and buildings removed by the data provider, from 2010 and 2012 were used in this study.

The LiDAR data in 2010 (from August 11 to August 24) were acquired using a Leica ALS50-II LiDAR System. Each return (data point) included a Global Positioning System (GPS) time stamp, spatial coordinates (*X*, *Y*, *Z*), intensity representing for the strength of the reflected signal, flightline, scan angle, and return number (first/last return). The data were collected from

an altitude of approximately 900~1300 m. The average spacing and average point density of irregularly-spaced LiDAR points for ground returns were 0.67 meters and 2.26 points/m^2, respectively. The range of scan angle was ± 20° and the vertical accuracy was 16 cm [*Romsos*, 2011].

The LiDAR data in 2012 (from March 25 to June 29) were acquired by using an Optech ALTM Gemini LiDAR system. The data were collected from an altitude of approximately 915 m. The average spacing and average point density of irregularly-spaced LiDAR points for ground return were 0.72 meters and 1.94 points/m^2, respectively. The range of scan angle was ± 19° and the vertical accuracy was 18 cm [*Dewberry*, 2012]. The point cloud data were processed to derive the 1 m contour lines and intensity raster, and the land surface topography using QCoherent software LP360 for ArcGIS.

As shown in Figure 3-1b, two sets of LiDAR data were available in 2010 and 2012. There was an overlap between these two LiDAR data sets for Blackwood Creek watershed and Ward Creek watershed. Therefore, two snapshots of LiDAR data were available for these two watersheds. Wet channel networks are identified in 2010 and 2012, respectively. The LiDAR acquisition date(s) for each watershed were listed in Table 3-1. The acquisition dates covered four consecutive days for Blackwood Creek and General Creek watersheds in 2010 and one or two days in the other snapshots.

The streamflow and its variation during the LiDAR acquisition dates are listed in Table 3-1. All LiDAR data in Table 3-1 were acquired during hydrograph recession periods. For example, the rainfall and hydrograph for Blackwood Creek during the LiDAR acquisition periods are plotted in Figure 3-2. Streamflow declined during the recession period from June to

September. The LiDAR survey for 2010 was located at the recession stage in August (Figure 3-2a) and the recession stage in June for 2012 (Figure 3-2b). Based on 53 years of daily streamflow records for Blackwood Creek, the exceedance probability during LiDAR survey was 73% in 2010 and 40% in 2012, respectively. As shown in Table 3-1, the exceedance probability of streamflow for all the snapshots was more than 40%. Particularly, the exceedance probability for General Creek was 95%, indicating low flows; therefore, dry channels were expected during the LiDAR acquisition period.
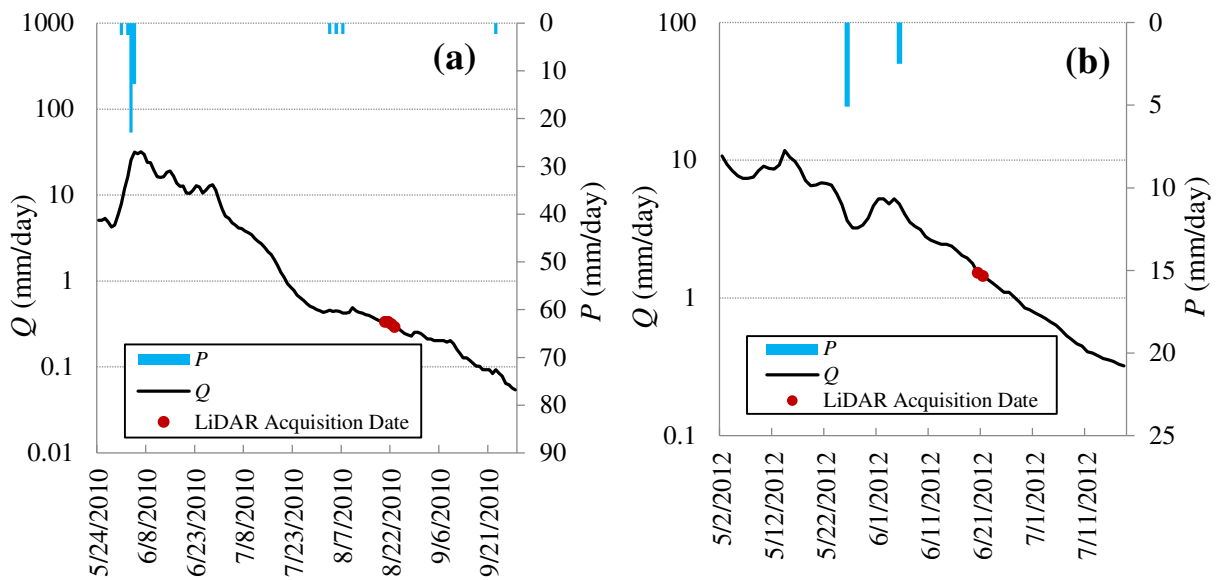
Figure 3-2: Rainfall, hydrograph for Blackwood Creek, and the LiDAR acquisition periods during (a) 8/20/2010-8/23/2010; and (b) 6/20/2012-6/21/2012.

3.3 Methodology

The signal intensity of ground returns was the main information used for identifying wet and dry channels. LiDAR intensities on water surfaces are usually lower than those on the dry land surface because of the strong absorption of the light energy by the water. The point cloud returns for water surfaces are usually associated with low signal intensities, dropouts, and a high relative variation of intensity [*Höfle et al.*, 2009]. The specular reflection from the water surface also contributes to low intensity of signal. When the signal intensity is lower than a threshold, the data point is dropout which was processed by the data acquisition provider; therefore, point density decreases with more dropouts on water surface. Figure 3-3a shows the 2010 intensity image for a headwater catchment in the Blackwood Creek watershed; Figure 3-3b shows the 2012 intensity image of the same area. The intensity value varied from 1 DN (digital number) to 245 DN for 2010 LiDAR and from 1 DN to 520 DN for 2012 LiDAR. As shown in Figure 3-3, the intensity in the wet channel was much lower than that on hillslopes and dry channels. The wet channel heads (i.e. upstream limits of wet channels) were identified visually and marked by blue dots. In this paper, a systematic procedure was developed to map the wet channel network based on the LiDAR returns. The first step was to quantify the intensity characteristics of wet and dry surfaces from sample sites; the second step was to filter ground returns by scan angles; third, the intensity threshold for differentiating wet and dry channels was identified based on the LiDAR return intensities on the sample sites; lastly, wet and dry channels were identified based on the identified intensity thresholds.
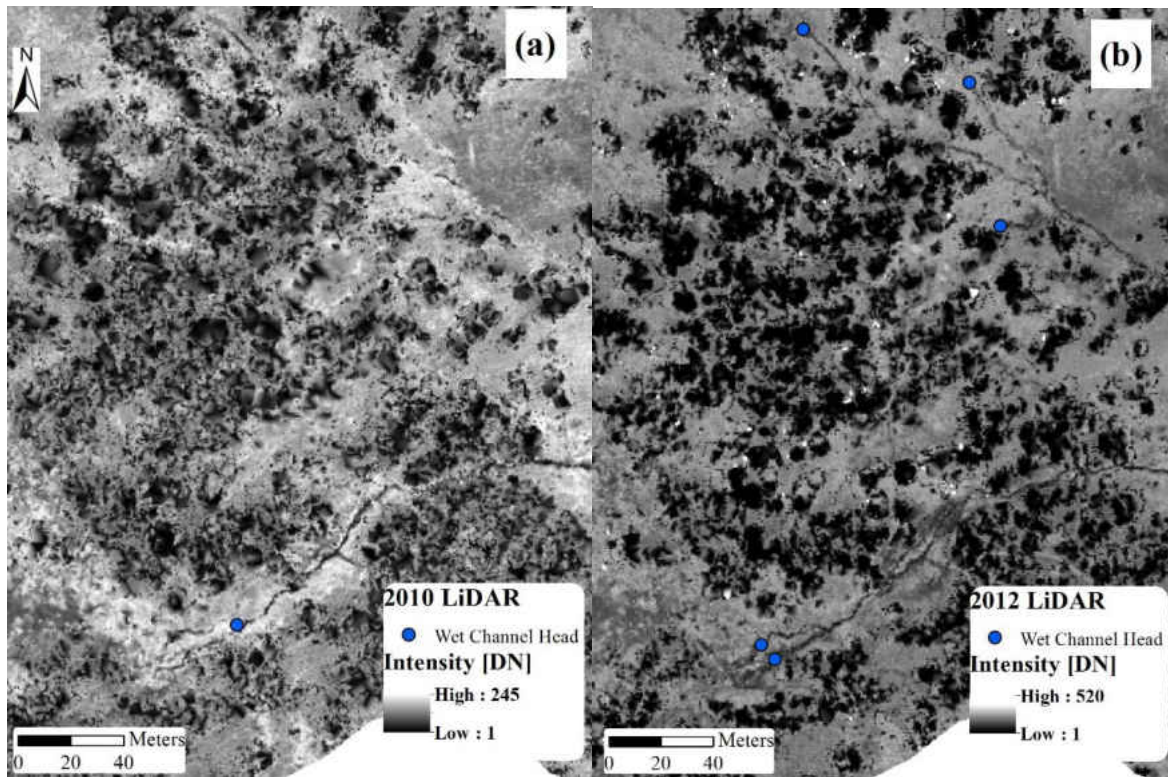
Figure 3-3: LiDAR intensity in the Blackwood Creek watershed: (a) 2010 LiDAR intensity for the zoom-in area; and (b) 2012 LiDAR intensity for the zoom-in area.

3.3.1 Sample Sites

Multiple sample sites were generated to explore the characteristics of intensity on wet and dry surfaces based on the following information 1) triangular irregular network (TIN) for the land surface topography; 2) morphologic drainage network (Figure 3-4a) derived from the LiDAR-based topography by the crenulation method using V-shaped contours [*Morisawa*, 1957]; 3) intensity image generated from point-based data shown in Figure 3-3; 4) 3D point clouds to determine channel segments that were not covered by trees; and 5) perennial and temporal streams

from National Hydrography Dataset (NHD) shown in Figure 3-4b. As shown in Figure 3-4, the

NHD temporal streams were underestimated as reported in other regions [e.g., *Elmore et al.*, 2013].

The sample sites for wet channels were generated on the perennial streams from NHD (Figure 3-4b) with a continuous low intensity pattern in the LiDAR returns moving downstream. The dry channel sample sites were generated at the tips of the head channels or on the temporal streams with high intensity.
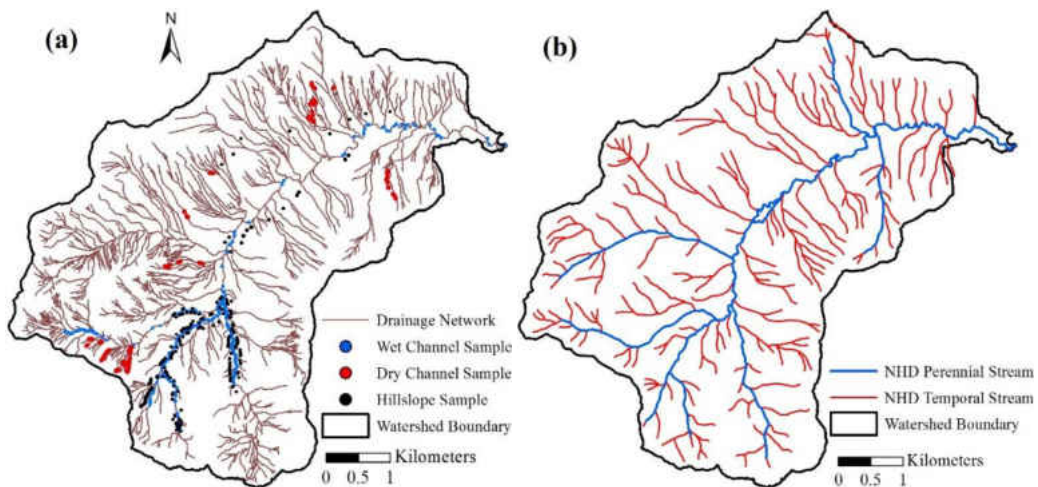
Figure 3-4: Blackwood Creek watershed: (a) the location of sample sites; (b) NHD perennial and temporal streams.

Polygons were generated for each sample site as shown in Figure 3-5. The TIN for the topography and drainage network was used to constrain the wet and dry channel samples between their banks. The point density in wet channels, particularly the main channel, was generally low due to the dropouts when the intensity of return was lower than a threshold (Figure 3-5a). The average area of the generated polygons for sample sites was 16 m^2. Average intensity was

computed within each polygon of the sample sites. 546 sample sites (265 on wet channels, 104 on dry channels, and 177 on dry hillslopes) were generated for analysis in the Blackwood Creek watershed (Figure 3-4a).
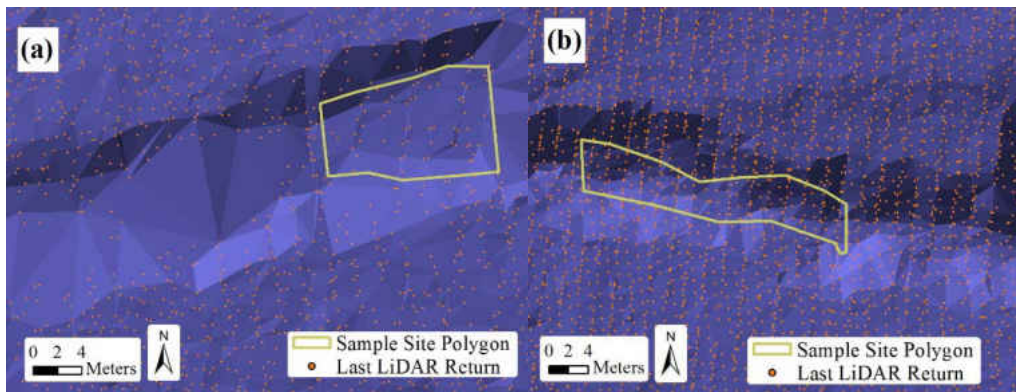
Figure 3-5: Blackwood Creek watershed: (a) a sample site on a wet channel segment; (b) a sample site on a dry channel segment.

3.3.2 Scan Angle Effect on Intensity

The intensity statistics of the identified wet and dry samples were quantified for each LiDAR snapshot. In general, LiDAR return intensities on water surfaces can be relatively high when laser pulses are at the nadir (directly beneath the aircraft and normal to the water surface) scan angle. Such signal saturation has the potential to introduce error into the estimation of wet and dry channels. For Blackwood Creek watershed, the intensities of some returns on water surface in 2012 were higher than 200 DN when the scan angles were less than 5°. This type of water surface return with high intensity can increase the average intensity of sample sites.

Therefore, for the case of Blackwood Creek watershed LiDAR data in 2012, the returns with scan angle less than 5° and intensity higher than 200 DN were removed when computing the average intensities of the sample sites.

3.3.3 Classification of Wet and Dry Channels

The distribution of intensity over wet channels, dry channels, and dry hillslope samples were obtained based on the ground returns within the polygons for sample sites. The average signal intensity within the polygons of each sample site was computed, and the point density for each sample site was calculated as the ratio between number of usable returns and the corresponding polygon area. The number of sample sites in each intensity bin was also counted for the three types of land surface. The probability distribution of intensity was represented by the normalized frequency, which is defined as the ratio of the number of samples in each bin to the total number of samples. For example, Figure 3-6a shows the normalized frequency histogram for intensity from sample sites of wet channels, dry channels, and dry hillslopes based on the 2012 LiDAR data in the Blackwood Creek watershed. The intensities in dry channels and hillslopes were generally higher than those in wet channels. The dry channels and dry hillslopes were grouped into one dry category as shown in Figure 3-6b where the blue and red histograms represent wet channels and dry channel/hillslopes, respectively.
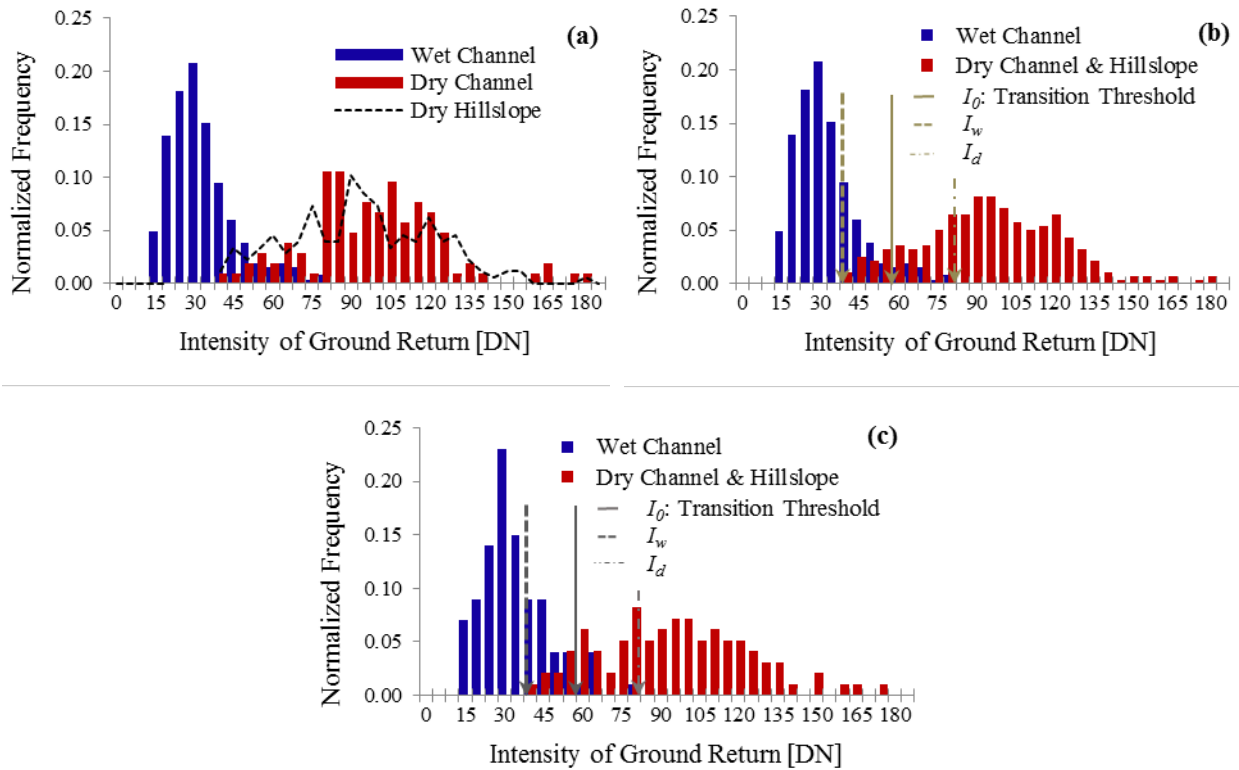
Figure 3-6: Normalized frequency distribution of intensity in the Blackwood Creek watershed based on the 2012 LiDAR data: (a) wet channel, dry channel and dry hillslope from all the samples; (b) wet channel, dry channel & hillslope, and the intensity thresholds for differentiating wet and dry channels from all the samples; and (c) wet channel, dry channel & hillslope from 100 randomly selected samples.

A threshold for wet channel identification was derived from the constructed intensity distributions of sample sites. As shown in Figure 3-6b, the transition threshold (I_0) was identified as the intensity value where the probability represented by normalized frequency for wet channel was equal to the probability for dry channels and hillslopes. There were two other thresholds identified: I_w was the lower bound of intensity for dry channels and hillslopes; I_d was the upper bound of intensity for wet channels. Wet channels are identified when intensity was less than I_0. When the intensity for a channel segment was less than I_w, the wet channel was classified as W_1;

61

when the intensity for a channel segment was between I_w and I_0, the wet channel segment was classified as W_2 and an uncertainty was associated with the classification. Similarly, the identified dry channel was classified as D_2 for channel segments with intensity between I_0 and I_d, and D_1 for channel segments with intensity higher than I_d.

3.4 Results and Discussion

3.4.1 Intensity Thresholds

The methodology described above was applied to the study watersheds and LiDAR surveys shown in Table 3-1. Table 3-2 shows the three identified thresholds for the Blackwood Creek watershed in 2012 and 2010. The intensity threshold for differentiating wet and dry channels was 55 DN in 2012 and 35 DN in 2010. The discrepancy between the thresholds of two surveys in a watershed can be attributed to the different LiDAR sensors, variations in path length resulting from the elevation changes, scan angle, surface specularity, atmospheric conditions, and the soil moisture conditions. A channel segment was identified as wet channel with high confidence level (W_1) when the intensity (I) was less than 36 DN, and wet channel with 91% confidence level (W_2) when I was greater than 36 DN but less than 55 DN. A channel segment was identified as dry channel with high confidence (D_1) when I was greater than 80 DN and with 80% confidence (D_2) when I was greater than 55 DN and less than 80 DN. These thresholds were obtained from the normalized frequency of sample sites in the Blackwood Creek watershed shown in Figure 3-6b.

Table 3-2: Thresholds for identifying wet and dry channels and the associated confidence level based on the intensity data in Blackwood Creek watershed, CA.

LiDAR	Thresholds [DN]			Wet channel confidence level		Dry channel confidence level	
Year	I_w	I_0	I_d	$W_1: I<I_w$	$W_2: I_w<I<I_0$	$D_2: I_0<I<I_d$	$D_1: I>I_d$
2012	36	55	80	100	91	80	100
2010	28	35	39	100	85	64	100

To assess the impact of samples on the identified thresholds, 100 samples were randomly selected from the wet channel and dry channel/hillslope sites, respectively. Figure 3-6c shows the distributions of intensity for the randomly selected samples for 2012 LiDAR. The distributions from Figure 3-6c were similar to the corresponding ones from all the samples shown in Figure 3-6b; the identified thresholds were 38 for I_w, 55 for I_0, and 77 for I_d. For 2010 LiDAR, the identified thresholds from randomly selected samples were 33 for I_w, 35 for I_0, and 39 for I_d. These thresholds were similar to the corresponding values from all the samples shown in Table 3-2. Therefore, the identified thresholds were robust with respect to the generated samples.

The number of wet and dry samples and thresholds of intensity for wet channels (I_0) were also identified for other watersheds as shown in Table 3-3. More than 150 wet or dry channel samples were generated for each watershed. The intensity threshold I_0 for the Ward Creek watershed was 35 DN in 2010 survey and 55 DN in 2012 survey. The intensity thresholds varied from 35 DN to 50 DN over the five watersheds during the survey in 2010; the intensity thresholds were 55 DN for the two surveys in 2012. The impact of samples on thresholds was evaluated using randomly selected samples for these watersheds, and no significant variation was observed.

Table 3-3: Intensity thresholds for each snapshot, the identified wet channel length and density based on the thresholds.

Watershed	Year	Number of wet samples	Number of dry samples	Intensity Threshold I_0 [DN]	Wet Channel Length [km]
Blackwood Creek, CA	2010	265	281	35	26.5
	2012	265	284	55	53.2
Ward Creek, CA	2010	167	167	35	23.0
	2012	167	167	55	46.3
General Creek, CA	2010	200	182	50	12.3
Trout Creek, CA	2010	178	193	45	31.0
Incline Creek, NV	2010	155	193	50	33.4
Incline Creek (Up), NV	2010	155	193	50	18.7

3.4.2 Wet Channel Network

Wet and dry surfaces were classified based on the point cloud of ground returns and the identified thresholds from sample sites. Intensity images for the study watersheds were generated with a spatial resolution of 0.5 m by 0.5 m as shown in Figure 3-7a for a selected area in the Blackwood Creek watershed. The road and the channel segment in the image had lower intensities than the surrounding environment. This intensity image was classified into four categories (W_1, W_2, D_1 and D_2) based on the intensity thresholds shown in Table 3-2. Figure 3-7b shows the classified land surface based on the intensity image shown in Figure 3-7a: W_1 represents wet surface; W_2 represents wet surface with a confidence level of 91% (Table 3-2); D_2 is dry surface with a confidence level of 80%; and D_1 is dry surface. Most of the area in Figure 3-7b was classified as dry (D_1), and some isolated patches were classified as wet (W_1) which were likely areas under dense canopy, wetlands or surface impoundments. The channel segment and road were classified as W_2 although some pixels were classified as W_1.

64
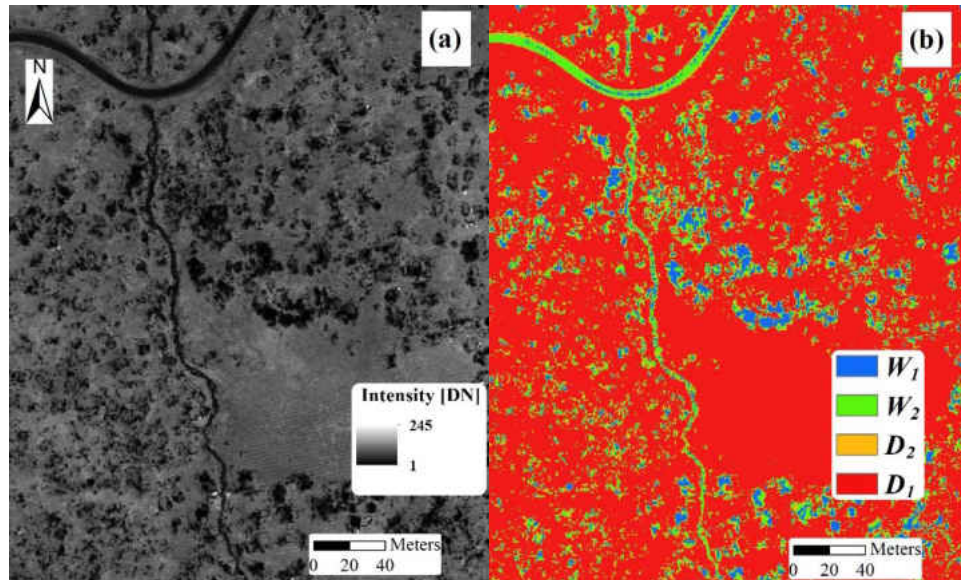
Figure 3-7: (a) intensity image for a selected region in the Blackwood Creek watershed based on the 2012 LiDAR data; and (b) classified four categories of land surface (W_1 is wet surface; W_2 is wet surface with 91% confidence; D_2 is dry surface with 80% confidence; D_1 is dry surface).

Channel networks with four categories (W_1, W_2, D_2 and D_1) were delineated by combining the classified intensity image and LiDAR-based topography. A triangulated irregular network (TIN) and contours with 1 meter interval were generated based on the elevation of LiDAR ground returns. Drainage networks were delineated by the crenulation method using *V*-shaped contours [*Morisawa*, 1957]. The TIN was also used to identify the channel widths. Then, the wet or dry conditions of the identified channels were determined based on the classified intensity image. Wet channels were exemplified by a continuous low intensity pattern shown in Figure 3-7a, even though dry channels may have isolated low intensity segments due to dense vegetation. Figure 3-8 shows the classified channel network based on the 2012 LiDAR data in the Blackwood Creek

watershed. The channel lengths for W_1, W_2, D_2, D_1 were 22 km, 31 km, 34 km, and 159 km, respectively. The ratio of wet channel length (W_1+W_2) to total channel length was 0.22.
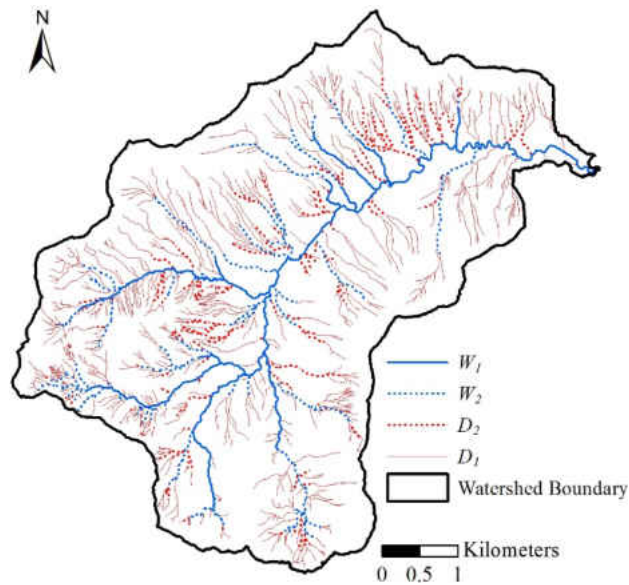
Figure 3-8: The identified wet channels with 100% confidence (W_1), wet channels with 91% confidence (W_2), dry channels with 80% confidence (D_2), and dry channels with 100% confidence (D_1) based on the 2012 LiDAR data in the Blackwood Creek watershed.

Two snapshots of identified wet channel network (W_1+W_2) were compared for the Blackwood Creek watershed (Figure 3-9) and the Ward Creek watershed (Figure 3-10). As shown in Figure 3-9, there were more wet channels during the 2012 survey compared with the 2010 survey. The total wet channel length was 53.2 km during the 2012 survey and 26.5 km during the 2010 survey; the corresponding wet channel density, which is defined as the ratio between wet channel length and total drainage area, was 1.84 km/km^2 and 0.92 km/km^2, respectively. The total wet channel length in the 2012 survey was almost twice that of the 2010 survey. As shown in

66

Table 3-1, the streamflow during the 2012 survey (0.52 m^3/s) was higher compared with the streamflow during the 2010 survey (0.10 m^3/s); and the streamflow exceedance probability was 40% and 73% during the 2012 and 2010 LiDAR surveys, respectively. It should be noted that the streamflow during the 2012 survey was about 5 times that of the 2010 survey. This indicated the nonlinear relationship between streamflow and wet channel length. Similarly for the Ward Creek watershed, the identified wet channel length during the 2012 survey (46.3 km) was twice the wet channel length (23.0 km) during the 2010 survey (Table 3-3). Correspondingly, the streamflow during the 2012 survey was about 4.5 times the streamflow during the 2010 survey (Table 3-1).
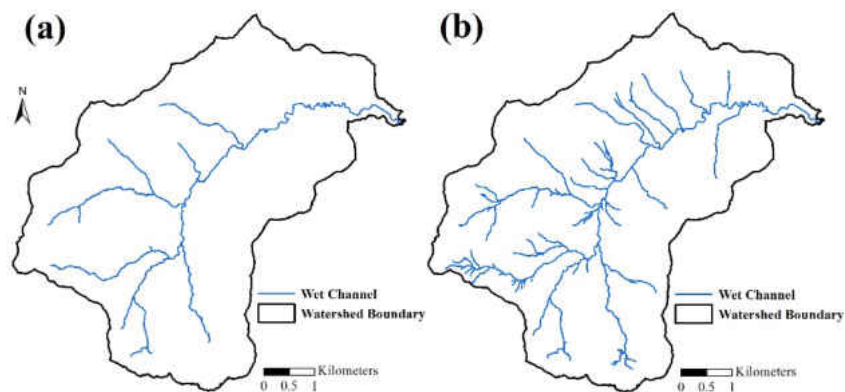
Figure 3-9: Blackwood Creek watershed: (a) identified wet channels during the 2010 LiDAR survey; and (b) identified wet channels during the 2012 LiDAR survey.
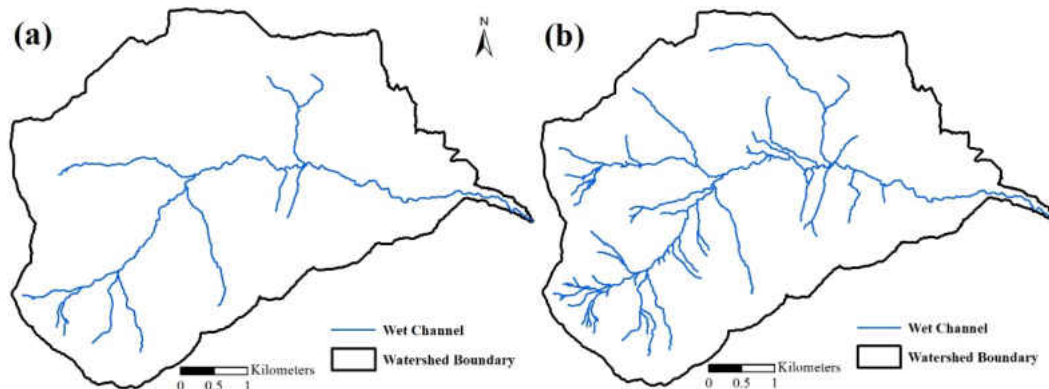
Figure 3-10: Ward Creek watershed: (a) identified wet channels during the 2010 LiDAR survey; and (b) identified wet channels during the 2012 LiDAR survey.

The identified wet channels (W_1+W_2) for the other four watersheds during the 2010 survey are presented in Figure 3-11: a) General Creek; b) Trout creek; and c) Incline Creek. These wet channel networks were delineated based on the intensity thresholds shown in Table 3-3. The wet channel for the General Creek in Figure 3-11a was only located in the main stream and the total wet channel length was 12.3 km. The corresponding wet channel density was 0.64 km/km^2, which was the smallest among all the watershed surveys. This indicated a dry condition during the LiDAR survey date as shown by the streamflow exceedance probability of 95% in Table 3-1. The total wet channel length in the Trout Creek watershed shown in Figure 3-11b was 31.0 km and the wet channel density was 1.62 km/km^2; the streamflow exceedance probability was 54%. The Incline Creek watershed has two main tributaries and there are two streamflow gage stations in the watershed (Figure 3-11c). One gage (#10336700) is located in the watershed outlet with a drainage area of 17.3 km^2 and the other one (#103366993) is located in one of the main tributaries with a drainage area of 7.4 km^2. The wet channel density was 1.93 km/km^2 for the gage #10336700 and 2.53 km/km^2 for the gage #103366993. This discrepancy was due to the different wetness in the

two main tributaries as explained by the streamflow exceedance probabilities in the two gages: 66% for #10336700 and 74% for #103366993.
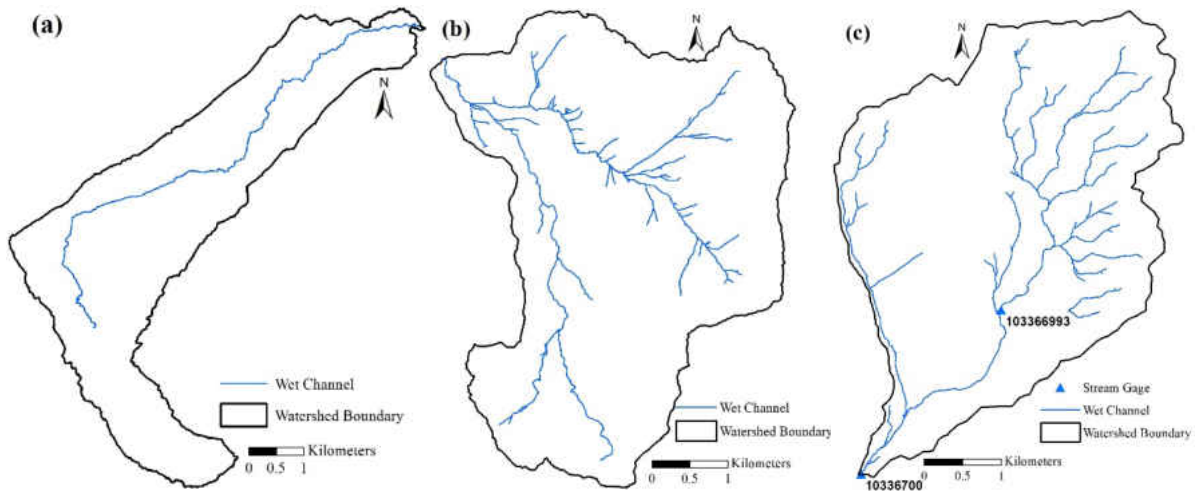
Figure 3-11: Identified wet channels from the 2010 LiDAR survey: (a) General Creek; (b) Trout creek; and (c) Incline Creek with two gage stations.

3.4.3 Streamflow and Wet Channel Length Relationship

As mentioned above, one of the goals of this paper was to investigate the relationship between wet channel length and streamflow. The availability of two LiDAR surveys for Blackwood Creek watershed and Ward Creek watershed (Table 3-1) provided the means to study wet channel length and streamflow in these two watersheds. Figure 3-12a shows wet channel length from LiDAR data versus streamflow for the Blackwood Creek and Ward Creek watersheds. For Blackwood Creek, wet channel length (and streamflow) was 53.2 km (0.52 m^3/s) on 6/20/2012 and 26.5 km (0.10 m^3/s) on 8/20/2010, respectively. For Ward Creek, wet channel length (and

69

streamflow) was 46.3 km (0.27 m^3/s) on 6/20/2012 and 23.0 km (0.06 m^3/s) on 8/14/2010, respectively. The wet channel length shrunk to half from 2012 to 2010 LiDAR surveys, while streamflow decreased to about 20% in both watersheds. Generally, streamflow is expected to decrease with wet channel length for a given watershed. Also, it was apparent that the rate of streamflow decrease was higher than that of wet channel length.
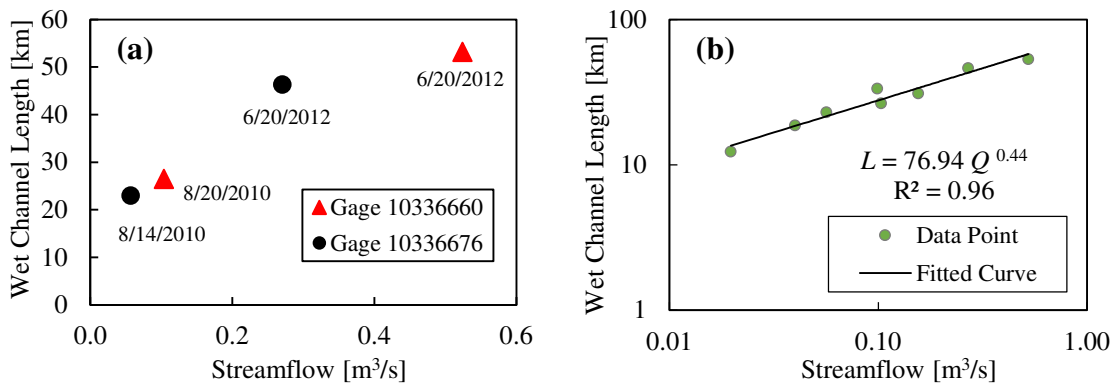
Figure 3-12: (a) Identified wet channel length and measured streamflow in the Blackwood Creek watershed (red triangle) and Ward Creek watershed (black circle); and (b) Relationship between streamflow and wet channel length across all study watersheds in the Lake Tahoe area.

Wet channel lengths are generally correlated with streamflow, and power-law relationships are usually identified [*Gregory and Walling*, 1968; *Godsey and Kirchner*, 2014]. More than two snapshots of wet channel length are required to construct the relationship between streamflow and wet channel length for a given watershed. However, it was reasonable to assume that the wet channel and discharge relationships for the five study watersheds are similar since they are around the Lake Tahoe with similar hydro-geomorphologic conditions. The climate aridity index, defined as the ratio between mean annual potential evaporation to precipitation [*Budyko*, 1974], ranged

from 1 to 1.6 for the 5 watersheds. The relation between wet channel length and discharge during recession periods for all the six stream gages are plotted in Figure 3-12b. A power-law relationship, $L = 76.94Q^{0.44}$ (or $Q \propto L^{2.3}$) was the best fit to the data with $R^2=0.96$ as shown in Figure 3-12b. The scaling exponent of the power-law relationship (i.e., 0.44) was within the range of reported values from fieldwork in other regions [e.g., *Gregory and Walling*, 1968]. *Godsey and Kirchner* [2014] re-analyzed the data published in other studies and found the broadly similar scaling exponents in catchments with varying geologic, topographic and climatic characteristics.

It should be noted that the wet channel length and streamflow in a watershed may be not a one-to-one relationship due to the spatial heterogeneity of runoff generation. Stream network expansion and contraction are related to the local watershed characteristics including the amount, intensity, and spatial distribution of rainfall, antecedent moisture contents, vegetation, rock type, and topography [*Morgan*, 1972; *Day*, 1978; *Gurnell*, 1978; *Goulsbra et al.*, 2014]. The exponent of the power relationship may also vary with wet/dry seasons [*Blyth and Rodda*, 1973; *Wigington et al.*, 2005] and rising/recession limbs [*Roberts and Archibold*, 1978]. At a given streamflow, the wet channel length during the rising limb can be different from that during the recession limb in that the relative contribution from surface runoff and base flow can vary greatly. The relationship shown in Figure 3-12b may be only applicable at the recession limbs through June to August for the study watersheds.

3.5 Summary and Future Research

The temporal dynamics of stream networks are of great importance to understand the hydrologic processes including stream and groundwater interactions, hydrograph recession, and

saturation excess runoff generation. The study of stream network dynamics is constrained by lack of temporal high-resolution observations on wet channel networks especially in non-perennial streams. The spatial resolution of satellite remote sensing image is currently insufficient to identify wet channel heads that are approximately 1 meter-wide. Moreover, wet channel heads are frequently obscured by canopies and not detectable in satellite images.

LiDAR provides an opportunity for mapping the wet channel network because of the high spatial resolution and the signal penetration through the canopy. To that end, a systematic method was developed for mapping the wet channel network based on LiDAR data. The method was based on the strong absorption of the light energy by the water surface and the corresponding differences between LiDAR return intensities from water and dry surfaces. Using selected sample sites with known wetness conditions, the signal intensities of ground returns were extracted from the LiDAR point data, and the frequency distributions of wet surface and dry surface were constructed. Three signal intensity thresholds were identified for differentiating wet and dry surfaces from the frequency distribution plots. Wet channels and dry channels were mapped through the generated intensity image and the identified thresholds, as well as the topographic TIN and 1 meter contour for channel identification.

The regional relationship between streamflow and wet channel length was obtained for the Lake Tahoe area based on eight LiDAR surveys in five watersheds. A power-law relationship between the discharge and wet channel length was obtained during the recession periods when LiDAR data were acquired. The scaling exponent was consistent with the reported findings from field work in other regions.

The proposed method for identifying wet channels can be applied to other watersheds with varying climatic and topographic gradients. Ideally, field surveys on wet channels would proceed simultaneously with a LiDAR acquisition flight. Still, we acknowledge that the NIR LiDAR signal is not able to penetrate water to measure the wet channel bed morphology. Alternatively, green LiDAR can penetrate the water surface and the LiDAR returns can provide water depth information, which can be combined with the intensity of NIR LiDAR to enhance the accuracy of wet channel network mapping.

3.6 <u>Acknowledgements</u>

3.7 <u>References</u>

Abrahams, A. D. (1984), Channel Networks: A Geomorphological Perspective, *Water Resour. Res.*, 20, 161–188, doi:10.1029/WR020i002p00161.

Acuña, V., T. Datry, J. Marshall, D. Barceló, C. N. Dahm, A. Ginebreda, G. McGregor, S. Sabater, K. Tockner, and M. A. Palmer (2014), Why Should We Care About Temporary Waterways?, *Science*, 343(6175), 1080-1081.

Antonarakis, A. S., K. S. Richards, and J. Brasington (2008), Object-based land cover classification using airborne LiDAR, *Remote Sens. Environ.*, *112*(6), 2988-2998.

Beeson, P. C., D. A. Miller and C. J. Duffy (2011), Identifying ephemeral and perennial stream reaches using apparent thermal inertia of an ungauged basin in Central New Mexico, *Geocarto International*, 26(3), 183-194.

Biswal, B., and M. Marani (2010), Geomorphological origin of recession curves*, Geophys. Res. Lett.,* 37, L24403, doi:10.1029/2010GL045415.

Blyth, K. and J. C. Rodda (1973), A stream length study, *Water Resour. Res.*, *9*, 1454–1461, doi:10.1029/WR009i005p01454.

Bowen, Z. H., and R. G. Waltermire (2002), Evaluation Of Light Detection And Ranging (LIDAR) For Measuring River Corridor Topography, *Journal of the American Water Resources Association*, *38*(1), 33-41.

Brzank, A., C. Heipke, J. Goepfert, and U. Soergel (2008), Aspects of generating precise digital terrain models in the Wadden Sea from lidar–water classification and structure line extraction, *ISPRS J. Photogramm. Remote Sens.*, *63*(5), 510-528.

Budyko, M. I. (1974), *Climate and Life*, 508 pp., Academic Press, New York.

Coats, R. N., and C. R. Goldman (2001), Patterns of nitrogen transport in streams of the Lake Tahoe basin, California-Nevada. *Water Resour. Res*. 37(2), 405–415.

Day, D. G. (1978), Drainage density changes during rainfall, *Earth Surface Processes, 3*, 319–326.

Dettinger, M. D. (2013), Projections and downscaling of 21st century temperatures, precipitation, radiative fluxes and winds for the Southwestern US, with focus on Lake Tahoe, *Climatic Change*, 116(1), 17-33, doi:10.1007/s10584-012-0501-x.

Dewberry (2012), *USGS/ FEMA Region IX –Placer County, CA LiDAR*, Report Produced for U.S. Geological Survey, USGS Contract: G10PC00013.

Elmore, A. J., J. P. Julian, S. M. Guinn, and M. C. Fitzpatrick (2013), Potential Stream Density in Mid-Atlantic US Watersheds, *PloS one*, *8*(8), e74819, doi:10.1371/journal.pone.0074819.

EPA (2010), *High and low stream flows*, Online Report, http://cfpub.epa.gov/eroe/index.cfm?fuseaction=detail.viewInd&lv=list.listbyalpha&r=21 9660&subtop=200

Genc, L., S. E. Smith, B. A. Dewitt (2005), Using satellite imagery and lidar data to corroborate an adjudicated ordinary high water line, *Int. J. Remote Sens.*, 26(17), 3683–3693.

Godsey S. E., and J. W. Kirchner (2014), Dynamic, discontinuous stream networks: hydrologically driven variations in active drainage density, flowing channels and stream order, *Hydrol. Process.*, *28*, 5791–5803, doi: 10.1002/hyp.10310.

Goulsbra, C., M. Evans and J. Lindsay (2014), Temporary streams in a peatland catchment: pattern, timing, and controls on stream network expansion and contraction, *Earth Surf. Process. Landforms*, *39*(6), 790-803, doi: 10.1002/esp.3533.

Gregory, K. J. and D. E. Walling (1968), The variation of drainage density within a catchment, *Hydrol. Sci. J*, *13*(2), 61–68.

Gurnell, A. M. (1978), The dynamics of a drainage network, *Nordic Hydrology, 9*, 293–306.

Hilldale, R. C., and D. Raff (2008), Assessing the ability of airborne LiDAR to map river bathymetry, *Earth Surf. Processes Landforms*, *33*(5), 773-783.

Höfle, B., M. Vetter, N. Pfeifer, G. Mandlburger, and J. Stötter (2009), Water surface mapping from airborne laser scanning using signal intensity and elevation data, *Earth Surf. Processes Landforms*, *34*(12), 1635-1649.

Hopkinson, C., N. Crasto, P. Marsh, D. Forbes, and L. Lesack (2011), Investigating the spatial distribution of water levels in the Mackenzie Delta using airborne LiDAR, *Hydrol. Processes*, *25*(19), 2995-3011.

Lang, M. W., and G. W. McCarty (2009), Lidar intensity for improved detection of inundation below the forest canopy, *Wetlands*, *29*(4), 1166-1178.

Le, P. V. V., and P. Kumar (2014), Power law scaling of topographic depressions and their hydrologic connectivity, *Geophys. Res. Lett.*, 41, 1553–1559, doi:10.1002/2013GL059114.

Magirl, C. S., R. H. Webb, and P. G. Griffiths (2005), Changes in the water surface profile of the Colorado River in Grand Canyon, Arizona, between 1923 and 2000, *Water Resour. Res.*, 41, W05021, doi:10.1029/2003WR002519.

Mallet, C., and F. Bretar. (2009), Full-waveform topographic lidar: State-of-the-art, *ISPRS J. Photogramm. Remote Sens.*, *64*(1), 1-16.

Marks, K., and P. Bates (2000), Integration of high-resolution topographic data with floodplain flow models, *Hydrol. Processes*, *14*(11-12), 2109-2122.

McFeeters, S. K. (1996), The use of the Normalized Difference Water Index (NDWI) in the delineation of open water features, *Int. J. Remote Sens.*, 17(7), 1425-1432, doi.org/10.1080/01431169608948714.

Meinzer, O. E. (1923), *Outline of ground-water hydrology, with definitions*, Washington, DC, US Geological Survey, Water Supply Paper 494.

Morgan, R. P. C. (1972), Observations on factors affecting the behaviour of a first-order stream. Trans. Ins. Brit. Geogr., *56*, 171-185.

Morisawa, M. (1957), Accuracy of determination of stream lengths from topographic maps, *Water Resour. Res.*, 38(1), 86-88.

Passalacqua, P., T. Do Trung, E. Foufoula-Georgiou, G. Sapiro, and W. E. Dietrich (2010), A geometric framework for channel network extraction from lidar: Nonlinear diffusion and geodesic paths, *J. Geophys. Res.*, 115, F01002, doi:10.1029/2009JF001254.

Pelletier, J. D. (2013), A robust, two-parameter method for the extraction of drainage networks from high-resolution digital elevation models (DEMs): Evaluation using synthetic and real-world DEMs, *Water Resour. Res.*, 49, doi:10.1029/2012WR012452.

Roberts, M. and P. Klingeman (1972), The relationship between drainage net fluctuation and discharge, *International Geography, Proceedings of the 22nd International Geographical Congress*, 189–191.

Roberts, M. C., O. W. Archibold (1978), Variation of drainage density in a small British Columbia watershed, AWRA Water Resources Bulletin, *14*(2), 470–476.

Romsos, J. S. (2011), *LiDAR Remote Sensing; Lake Tahoe Watershed California/Nebada*, Watershed Sciences, Tahoe Regional Planning Agency.

Smeeckaert, J., C. Mallet, N. David, N. Chehata, and A. Ferraz (2013), Large-scale classification of water areas using airborne topographic lidar data, *Remote Sens. Environ.*, *138*, 134-148.

Stanley, E. H., S. G. Fisher, and N. B. Grimm (1997), Ecosystem expansion and contraction in streams, *BioScience*, 47, 427-435.

Stoker, J. M., S. K. Greenlee, D. B. Gesch, and J. C. Menig (2006), CLICK: The new USGS center for lidar information coordination and knowledge, *Photogramm. Eng. Remote Sens*, *72*(6), 613-616.

Taylor, A. H., and R. M. Beaty (2005), Climatic influences on fire regimes in the northern Sierra Nevada mountains, Lake Tahoe Basin, Nevada, USA. *J. Biogeogr.* 32(3), 425-438.

Wang, D. and L. Wu (2013), Similarity of climate control on base flow and perennial stream density in the Budyko framework, *Hydrol. Earth Syst. Sci.*, 17, 315-324, doi:10.5194/hess-17-315-2013.

Wigington, P. J., T. J. Moser and D. R. Lindeman (2005), Stream network expansion: a riparian water quality factor, *Hydrol. Process.*, *19*, 1715–1721, doi: 10.1002/hyp.5866.

Wolfe, W. L., G. J. Zissis (1993), *The Infrared Handbook*, Environmental Research Institute of Michigan, IRIA Series in Infrared and Electro Optics, Ann Arbor, MI.

Work, E. A. and D. S. Gilmer (1976), Utilization of satellite data for inventorying prairie ponds and lakes, *Photogramm. Eng. Remote Sens.*, 42, 685-694.

Wu, H., C. Liu, Y. Zhang, W. Sun, and W. Li (2013), Building a water feature extraction model by integrating aerial image and lidar point clouds, *Int. J. Remote Sens.*, *34*(21), 7691-7705, doi:10.1080/01431161.2013.823674.

Xu, H. (2006), Modification of normalized difference water index (NDWI) to enhance open water features in remotely sensed imagery, *Int. J. Remote Sens.*, 27(14), 3025-3033, doi.org/10.1080/01431160600589179.

CHAPTER 4: ASSESSING THE STREAMFLOW CHARACTERISTICS OF PERENNIAL STREAMS BASED ON A WET CHANNEL NETWORK EXTRACTED FROM LIDAR DATA

4.1 Introduction

Wet channel networks expand during rainfall events, contract during recession periods, as well as disconnect and reconnect hydrologically [*Schumm*, 1956; *Howard and Kerby*, 1983]. Channels are categorized as perennial, intermittent, and ephemeral streams based on the flow durations. Perennial streams flow most of the time during normal years and are maintained by groundwater discharge [*Meinzer*, 1923; *NC Division of Water Quality*, 2010]. Perennial streams are usually defined based on a certain threshold of flow duration. However, there are discrepancies in the perennial stream definitions in the literature. *Hedman and Osterkamp* [1982] defined channels with flowing water for more than 80% of the time as perennial streams; *Hewlett* [1982] and *Texas Forest Service* [2000] used 90% as the threshold. Intermittent (i.e., seasonal) streams flow during certain times of the year receiving water from surface sources such as melting snow or from groundwater sources such as springs [*Meinzer*, 1923; *Levick et al.*, 2008]. Variations in water table affect the characteristics of intermittent streams that are supplied by groundwater sources [*Meinzer*, 1923]. Ephemeral streams flow only in direct response to precipitation without continuous surface flow [*Meinzer*, 1923]. The total volume of flow under the annual hydrograph of an ephemeral stream watershed is the result of direct runoff from large rainfall events [*Chow et al.*, 1988]. Some ephemeral streams flow only for several hours annually [*Blasch et al.*, 2002].

Intermittent and ephemeral streams flow with temporal and spatial variability [*Levick et al.*, 2008], and are generally referred to as "temporary" streams that support high biodiversity and important ecosystem processes [*Acuña et al.*, 2014].

United States Geological Survey (USGS) Quadrangle topographic ''blue line'' maps classify perennial, intermittent and ephemeral streams based on aerial photo interpretation. These classifications are confirmed by USGS field surveys when the maps are compiled [*Simley*, 2003]. Although USGS monitors perennial streams regularly to generate flood and water supply information, they rarely check intermittent or ephemeral streams. The map delineation between perennial-intermittent and intermittent-ephemeral streams is performed with very little information and their reliability is uncertain [*Svec et al.*, 2005].

The introduction of airborne light detection and ranging (LiDAR) provides an opportunity to accurately study drainage networks. LiDAR provides topographic data at sub-meter resolution and accuracy [*Marks and Bates*, 2000; *Bowen and Waltermire*, 2002] and has been applied to extract channel networks [*Lashermes et al.*, 2007; *Orlandini and Moretti*, 2009; *Passalacqua et al.*, 2010; *Orlandini et al.*, 2011; *Sofia et al.*, 2011; *Pelletier*, 2013; *Clubb et al.*, 2014].

In addition to the elevation data, LiDAR provides signal intensity information which is a relative measurement of the return strength of the laser pulse. The intensity return from water surfaces is relatively low compared with dry lands. LiDAR intensity has been utilized to map relatively large and continuous water bodies such as flood inundation extent, rivers, wetlands, ponds and lakes [*Genc et al.*, 2005; *Höfle et al.*, 2009; *Smeeckaert et al.*, 2013; *Wu et al.*, 2013]. *Hooshyar et al.* [2015] developed an extraction method for wet channel network extraction by

integrating LiDAR intensity and digital elevation model (DEM) for detecting narrow, disconnected and shallow streams located in headwater catchments.

The objective of this research was to explore the definition of perennial streams using the non-dimensional relationship between streamflow exceedance probability and wet channel ratio, defined as the wet channel length divided by the total valley length. The valley network and wet channels were extracted from LiDAR topographic data and signal intensity of ground returns with 1-m spatial resolution using the method developed by *Hooshyar et al.* [2015]. The obtained wet channel ratios of perennial streams in the study watersheds were compared with the definitions of perennial streams in the literature.

4.2 Methodology

4.2.1 Data

The total of 30 study watersheds, located across 10 states in the U.S., were selected based on the availability of both streamflow observations and LiDAR data as shown in Figure 4-1. The LiDAR data were obtained through the USGS Center for LiDAR Information, Coordination and Knowledge (CLICK) website (http://lidar.cr.usgs.gov). The LiDAR acquisition dates for each watershed were obtained from digital flight logs provided by the LiDAR survey companies listed in Table 4-1. The LiDAR survey years for the study watersheds were from 2009 to 2012. The intensity map and the land surface topography were derived by the LiDAR point cloud data using the QCoherent LP360 toolbox for ArcGIS.
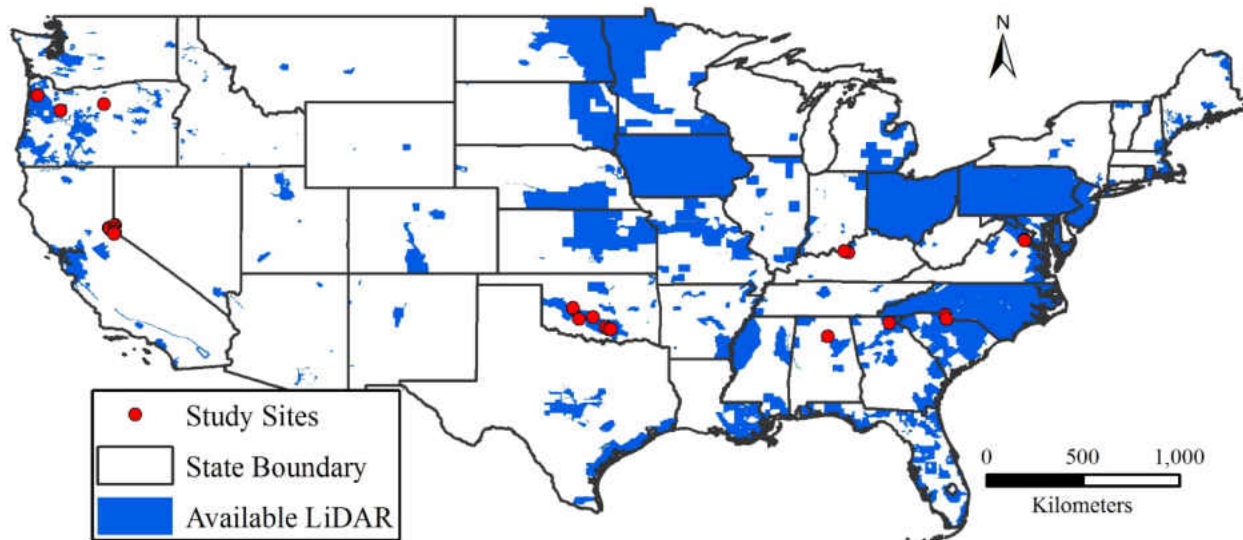
Figure 4-1: Location of study sites and available LiDAR data.

The drainage area, climate aridity index (E_P/P), streamflow, variation and streamflow exceedance probability (E_Q) during the LiDAR acquisition dates are listed in Table 4-1. Streamflow observations were acquired from the USGS National Water Information System (http://waterdata.usgs.gov/nwis). E_Q was defined as the probability that a specific streamflow will be exceeded and achieved for each watershed through generating a flow duration curve based on the daily streamflow records from USGS gages. The range of E_Q for study watersheds ranged from 7% (high flow) to 98% (low flow). For example, E_Q of Shafer Creek and General Creek were 98% and 95% respectively, indicating a low flow condition when extensive dry channels were expected.

The climate aridity index, defined as the ratio of potential evaporation to precipitation (E_P/P), was used as a numerical indicator of the climate in a watershed [*Budyko*, 1958; 1974].

82

Except for Tucca Creek (0.3), Schafer Creek (0.4) and Pine Creek (2.7), the climate aridity index varied from 0.8 to 2.1 for the study watersheds.

Perennial streams were obtained from the National Hydrograph Dataset (NHD). The flowing channel networks corresponding to certain streamflow exceedance probabilities were compared with the NHD perennial stream to evaluate the determination of perennial stream.

Table 4-1: USGS gage identification number, drainage area, climate aridity index, streamflow and its exceedance probability during the LiDAR surveys for the study watersheds.

Watershed	USGS gage	Drainage Area [km^2]	E_P/P	LiDAR Acquisition Date	Streamflow [m^3/s]	E_Q [%]
Tucca Creek, OR	14303200	6.0	0.3	5/9/2010 ~5/13/2010	0.481±0.11	28
Schafer Creek, OR	14188610	5.5	0.4	10/9/2012	0.001	98
Chattahoochee River, GA	02330450	116.2	0.8	3/30/2010	4.474	27
Ward Creek, CA (Upstream)	10336674	12.0	0.9	8/14/2010	0.074	54
Blue Springs Creek, AL	02449882	31.4	0.9	2/26/2010	0.481	26
Cedar Creek, KY	03297800	31.2	1.0	3/21/2009	0.136	51
Brier Creek, KY	03302050	10.5	1.0	3/20/2009	0.037	47
Blackwood Creek, CA	10336660	28.9	1.0	8/20/2010 ~8/23/2010	0.103±0.01	73
				6/20/2012 ~6/21/2012	0.524±0.01	40
Ward Creek, CA	10336676	24.9	1.0	8/14/2010	0.057	72
				6/20/2012 ~6/21/2012	0.27±0.01	43
S F Quantico Creek, VA	01658500	19.4	1.0	4/7/2011 ~4/14/2011	0.194±0.03	22
M Chopawamsic Creek, VA	01659500	11.4	1.1	4/7/2011	0.096	28
N Chopawamsic Creek, VA	01659000	15.0	1.1	4/7/2011	0.125	26
S Chopawamsic Creek, VA	01660000	6.5	1.1	4/6/2011 ~4/7/2011	0.057±0.01	45
General Creek, CA	10336645	19.2	1.1	8/20/2010 ~8/23/2010	0.020	95
Allison Creek, SC	021457492	104.0	1.1	3/12/2012	0.425	34
Wildcat Creek, SC	021473428	76.6	1.1	3/8/2011	0.453	20
Pennington Creek, OK	07331295	85.2	1.3	12/22/2009 ~12/26/2009	0.580±0.04	28

Watershed	USGS gage	Drainage Area [km²]	E_P/P	LiDAR Acquisition Date	Streamflow [m³/s]	E_Q [%]
Mill Creek, OK	07331200	120.9	1.3	12/22/2009	0.255	26
Rock Creek, OK	07329852	114.3	1.3	12/22/2009	0.651	33
Incline Creek, NV (Upstream)	103366993	7.4	1.4	8/12/2010	0.040	74
North Criner Creek, OK	07328180	18.6	1.5	12/20/2009	0.006	67
Incline Creek, NV	10336700	17.3	1.5	8/12/2010	0.099	66
Trout Creek, CA	10336770	19.1	1.6	8/23/2010	0.156	54
Little Washita River, OK	07327442	36.5	1.6	12/17/2009	0.071	41
Little Washita River,OK (Upstream)	073274406	9.3	1.6	12/17/2009	0.015	45
Lake Creek, OK	07325840	49.4	1.7	12/13/2009	0.176	18
Logan House Creek, NV	10336740	5.3	1.9	8/16/2010 ~8/17/2010	0.002	87
Glenbrook Creek, NV	10336730	10.3	2.1	8/16/2010 ~8/18/2010	0.005	88
Eagle Rock Creek, NV	103367592	1.5	2.1	8/16/2010 ~8/17/2010	0.014	75
Pine Creek near Clarno, OR	14046890	336.9	2.7	5/19/2011 ~5/20/2011	0.368	7

4.2.2 LiDAR Data Processing

The key component of the LiDAR data for identifying wet channels was the signal intensity of ground returns. The signal intensity is a relative measurement of the return strength of laser pulse received by the LiDAR sensor. Generally, LiDAR systems operate in the near-infrared (NIR) range and the absorption of NIR by water is significantly higher than that by dry land [*Wolfe and Zissis*, 1989]. This characteristic of NIR leads to the fact that LiDAR return intensities over water surfaces are relatively low compared with dry lands such as dry channels and hillslopes.

Figure 4-2 shows the intensity map for a headwater catchment in Ward Creek. Wet channels show consistently lower intensities and a continuous pattern relative to other locations

such as hillslopes and dry channels. Wet channel heads, which are starting points of wet channels, are visually detectable and marked by blue dots.
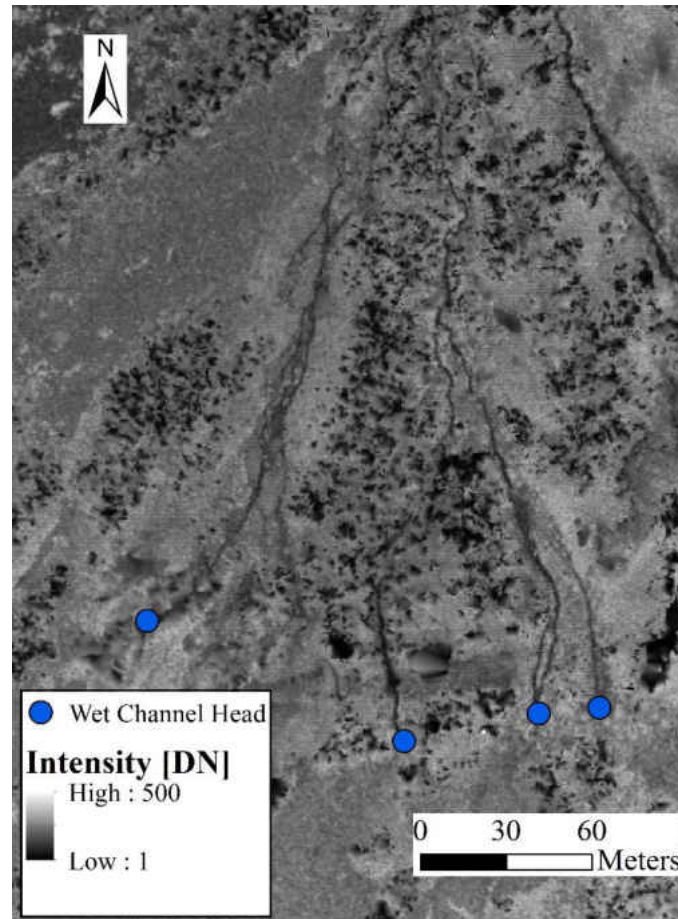

Figure 4-2: Intensity image during 2012 LiDAR survey for a headwater area in Ward Creek watershed and the visually identified wet channel heads.

Hooshyar et al. [2015] developed a systematic method for wet channel network extraction by integrating LiDAR intensity with the digital elevation model (DEM). In this study, intensity maps and DEMs were generated with a spatial resolution of 1-m. This method was based on several major steps. First, densely vegetated areas in the intensity map were filtered out because the return intensity from ground points under canopy is typically low regardless of wetness and

their inclusion could lead to false positives. This was accomplished by filtering out any pixels in which the difference between the ground and canopy elevations was more than 2 m. The second step was to extract the valley network and extent from the LiDAR-based 1-m DEM. Wet channels are located within the valley network where individual valleys are associated with positive contour curvature. A small positive curvature threshold (0.025 m^{-1}) was used to generate the valley extent from the DEM. Figure 4-3 shows a contour curvature map and the identified valley extent determined by the curvature threshold in a sub-catchment of Ward Creek watershed. The third step was to decompose the composite probability distribution function (PDF) of intensity. The general PDF of intensity consists of several Gaussian distributions and each distribution corresponds to a category of ground surface such as wet or dry condition. The intensity thresholds for classifying wet pixels were extracted from the PDF analysis on points within the valley extent using a Gaussian mixture model [*Rasmussen*, 1999]. Figure 4-4 graphically shows the individual PDFs and two thresholds, I_w for wet pixels and I_d for dry pixels, that were identified to differentiate wet, transition, and dry surfaces. The forth step was to detect edges corresponding to high gradient pixels in the intensity map using Canny's method [*Canny*, 1986] to improve the identification of small wet channels. Finally, the wet channel network was generated by combining wet pixels based on the intensity thresholds and the detected edges. Isolated segments of the resulting wet channels were manually connected.

Figure 4-5a shows the identified wet pixels and Figure 4-5b shows the connected wet channel network and the valley network after processing isolated wet channel segments in the Ward Creek watershed. The wet channel and valley network of all study watersheds are shown in Appendix A.
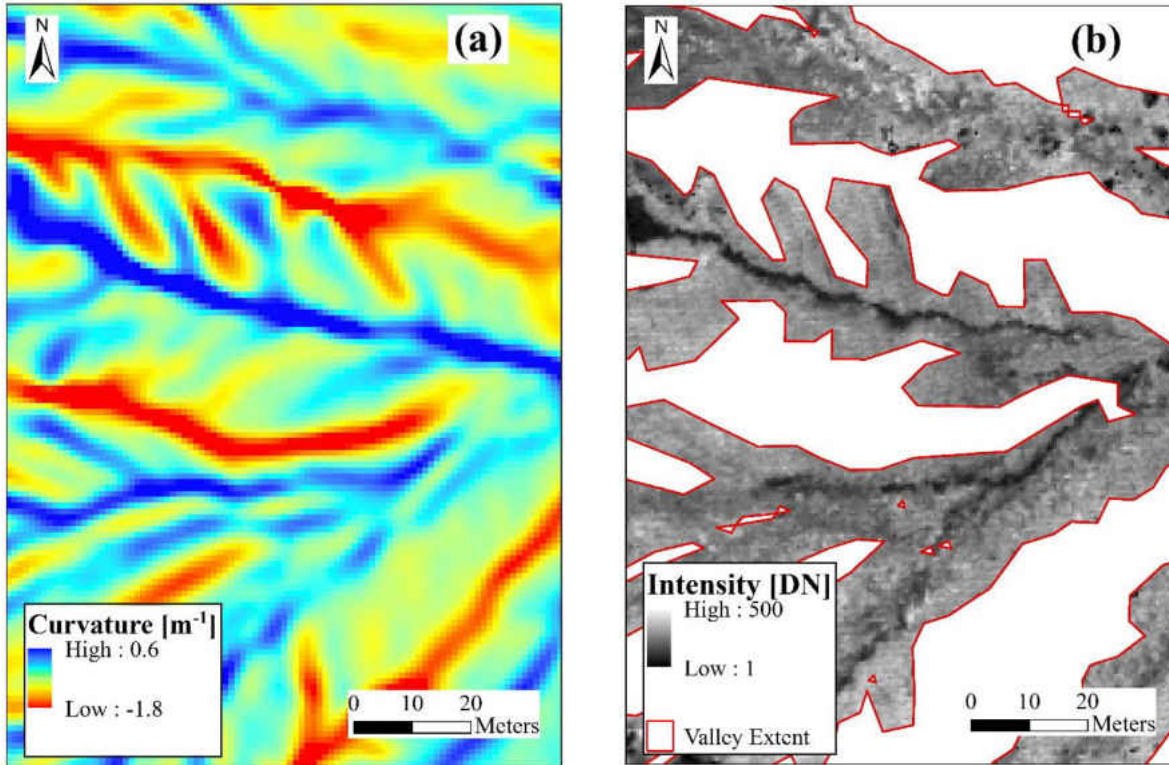
Figure 4-3: (a) Contour curvature and the visible detection of drainage path by blue color pixels. (b) The intensity returns within the valley extent determined by the curvature threshold in the Ward Creek watershed for 2012 LiDAR survey.
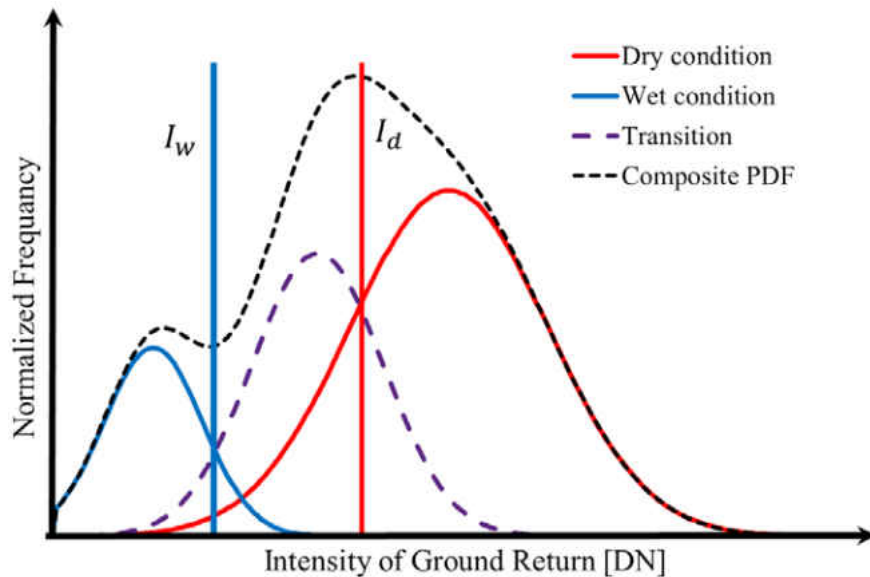
Figure 4-4: A schematic illustration of the individual and the composite PDFs of intensity along with the wet (I_w) and dry (I_d) thresholds.
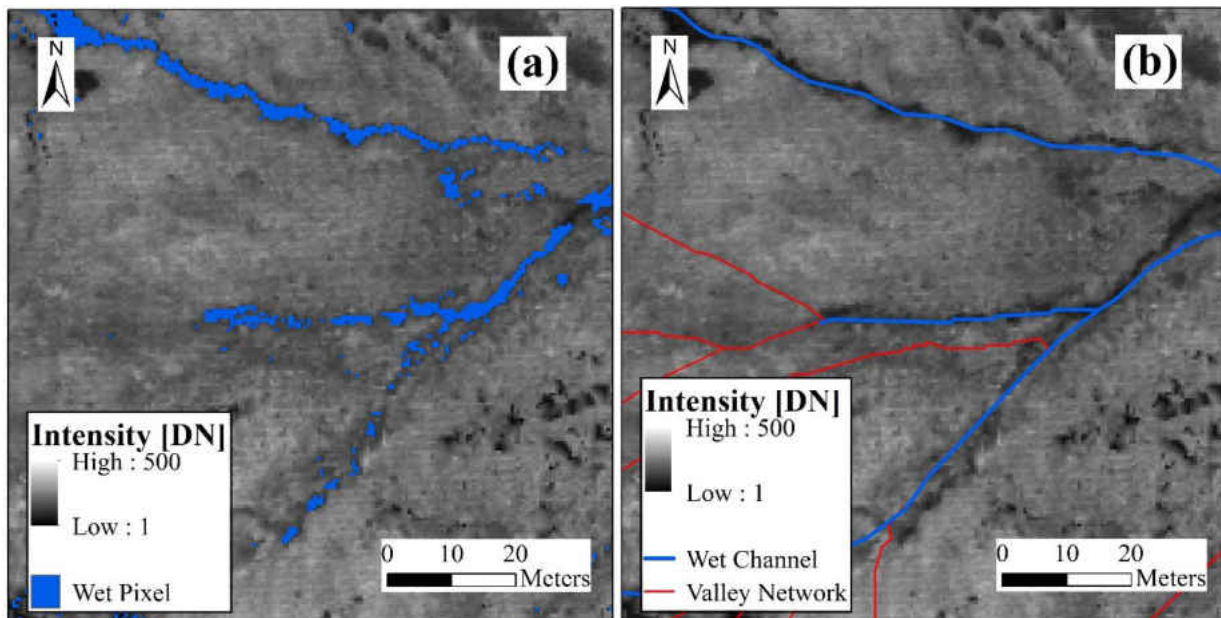

Figure 4-5: (a) The identified wet pixels based on intensity thresholds. (b) The connected wet channel network with the valley network after processing isolated wet channel segments for based on 2012 LiDAR survey in the Ward Creek watershed.

4.3 <u>Results and discussion</u>

Hooshyar et al. [2015]'s method was applied to all study watersheds using LiDAR-based DEM and intensity data in order to extract valley network and identify wet channels.

4.3.1 L-Q Relationship

Wet channel length generally increases with streamflow and has been described by an empirical power law function based on field observations. This has been proven to be effective in quantifying this relationship as reported by *Blyth and Rodda* [1973], *Godsey and Kirchner* [2014], and *Whiting and Godsey* [2016]. *Hooshyar et al.* [2015] also corroborated that the power law relationship holds when using wet channels identified by integrating LiDAR intensity and elevation data. The scaling exponent of the power law relationship can be unique to the season (e.g., wet or dry) [*Blyth and Rodda*, 1973; *Wigington et al.*, 2005] and the position in the hydrograph (e.g., rising or recession limb) [*Roberts and Archibold*, 1978]. This is due to the dependence of the wet channel network on the local watershed properties such as precipitation, soil, vegetation and topography [*Morgan*, 1972; *Day*, 1978; *Gurnell*, 1978; *Goulsbra et al.*, 2014].

The relation between wet channel length (L_W) and streamflow (Q) for study watersheds is plotted in Figure 4-6, and total valley length, wet channel length and wet channel ratio are listed in Table 4-2. Three watersheds were excluded from the data for being excessively humid (E_P/P: 0.3~0.4) and arid (E_P/P: 2.7) since they displayed uncharacteristic patterns of wet channel length and streamflow. The range of E_P/P was 0.8 to 2.1 for remaining 27 watersheds with 29 LiDAR snapshots and the best fit function was $L_W = 161.22Q^{0.623}$ with $R^2 = 0.74$ shown in Figure 4-6. The scaling exponent of the power-law relationship (i.e., 0.623) was within the range of reported values

(i.e., 0.042~0.688) in the literature from fieldwork for 14 watersheds in other regions [*Godsey and Kirchner*, 2014].
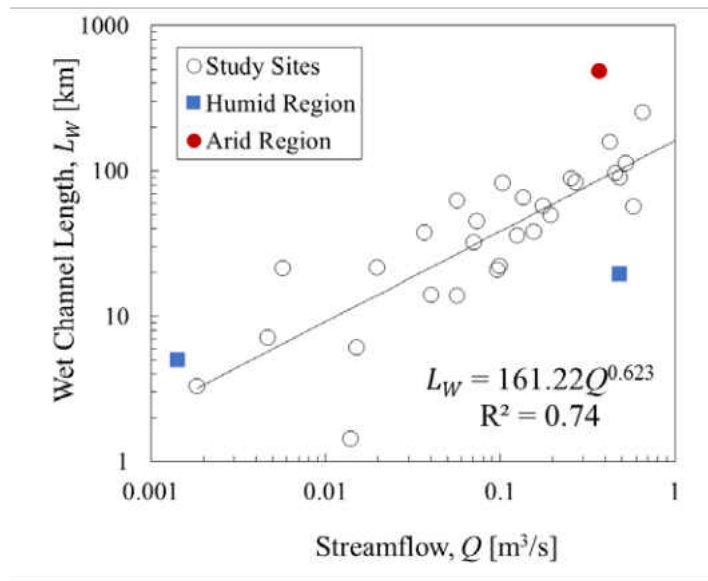

Figure 4-6: The relationship between streamflow (Q) and wet channel length (L_W) in study watersheds.

Table 4-2: Total valley length, wet channel length and wet channel ratio for the study watersheds.

Watershed	E_P/P	Total Valley Length [km]	Wet Channel Length [km]	Wet Channel Ratio (%)
Tucca Creek, OR	0.3	62.7	19.6	31.3
Schafer Creek, OR	0.4	87.1	5.0	5.8
Chattahoochee River, GA	0.8	1241.1	327.1	26.4
Ward Creek, CA (Upstream)	0.9	164.2	45.6	27.7
Blue Springs Creek, AL	0.9	188.2	90.6	48.1
Cedar Creek, KY	1.0	193.1	65.7	34.0
Brier Creek, KY	1.0	165.9	37.7	22.7
Blackwood Creek, CA (2010)	1.0	416.8	82.9	19.9
Blackwood Creek, CA (2012)	1.0	417.4	113.2	27.1

Ward Creek, CA (2010)	1.0	257.5	62.8	24.4
Ward Creek, CA (2012)	1.0	257.5	83.9	32.6
S F Quantico Creek, VA	1.0	92.6	49.7	53.7
M Chopawamsic Creek, VA	1.1	52.9	20.9	39.4
N Chopawamsic Creek, VA	1.1	79.5	35.9	45.2
S Chopawamsic Creek, VA	1.1	31.2	13.8	44.3
General Creek, CA	1.1	218.4	21.6	9.9
Allison Creek, SC	1.1	376.1	158.2	42.1
Wildcat Creek, SC	1.1	176.7	96.7	54.7
Pennington Creek, OK	1.3	101.7	57.3	56.3
Mill Creek, OK	1.3	114.9	89.4	77.8
Rock Creek, OK	1.3	436.8	252.8	57.9
Incline Creek, NV (Upstream)	1.4	55.5	14.1	25.4
North Criner Creek, OK	1.5	84.6	21.4	25.3
Incline Creek, NV	1.5	134.4	22.1	16.5
Trout Creek, CA	1.6	208.4	38.4	18.4
Little Washita River, OK	1.6	62.1	32.3	52.0
Little Washita River,OK (Upstream)	1.6	10.2	6.1	60.4
Lake Creek, OK	1.7	120.8	57.5	47.6
Logan House Creek, NV	1.9	22.3	3.3	14.8
Glenbrook Creek, NV	2.1	51.1	7.2	14.1
Eagle Rock Creek, NV	2.1	14.9	1.4	9.6
Pine Creek near Clarno, OR	2.7	1436.0	486.2	33.9

4.3.2 Non-dimensional Analysis

To better understand the definition of perennial streams, relations between two non-dimensional variables were investigated (Figure 4-7): streamflow exceedance probability (E_Q), and wet channel ratio (α_W), defined as the ratio of wet channel length to the total valley length. E_Q values of 0% and 100% represented the highest and lowest streamflow respectively. An E_Q of 0% was likely an underestimation since it was evaluated based on limited streamflow data. Despite this fact, it was assumed that all stream networks was flowing (i.e., α_W=100%) when the maximum

streamflow occurred (i.e., E_Q =0%).   Under this assumption, the best fit function was an exponential function, $\alpha_W = 100e^{-0.024E_Q}$ with $R^2 = 0.73$ as shown in Figure 4-7.

From the fitted equation, an E_Q of 100% (i.e., minimum streamflow) corresponded to an α_W of 9.1 %. Using the definition of perennial stream from the literature, E_Q of 90% and 80% corresponded to α_W values of 11.4% and 14.7%, respectively. *Wang and Wu* [2013] showed that perennial stream density declines from around 0.6 km/km^2 to 0.2 km/km^2 since the minimum streamflow decreases when E_P/P increases from 0.8 to 2.1 (i.e., less rainfall). The drainage density slightly increases (around 9~13 km/km^2) for $0.8 \leq E_P/P \leq 2.1$ based on the dependence of drainage density on climate from Chapter 2. Therefore, perennial stream ratio (*PSR*), defined as perennial stream length over the total valley length, for perennial stream declines with E_P/P.
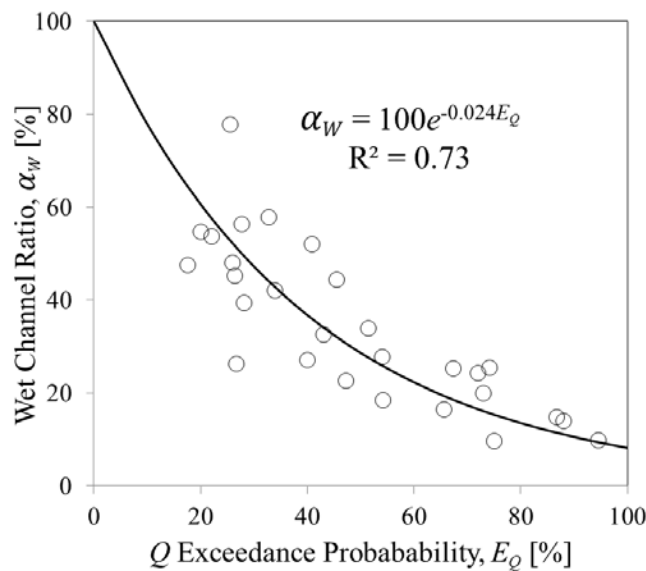

Figure 4-7: The relationship between streamflow exceedance probability, E_Q and wet channel ratio (α_W) in the study watersheds.

The perennial stream length of each watershed was obtained from the National Hydrography Dataset (NHD); and perennial stream ratio (*PSR*) was computed. As shown in Figure 4-8a, E_Q of perennial streamflow for each watershed was calculated using the relationship between E_Q and α_W shown in Figure 4-7. The range of *PSR* for study watersheds was 1.2% to 29.4% with a mean of 11.0%; the range of E_Q corresponding to perennial streamflow was from 49% to 100% and the average value was 86%. Figure 4-8b shows the distribution of perennial streamflow E_Q for the study watersheds. The distribution was represented by normalized frequency, defined as the ratio of the number of watersheds in each bin to the total number of watersheds. 71% of study watersheds had E_Q values greater than 80% corresponding to perennial streamflow.

Perennial streamflow for each watershed was directly calculated from perennial stream length using the relationship between streamflow (Q) and wet channel length (L_W) in Figure 4-6. Afterward, another E_Q of perennial streamflow was computed using the flow duration curve of each watershed. The range of E_Q regarding perennial streamflow was from 51% to 100% and average value was 88%.

The range of E_Q associated with perennial streamflow was similar using both relationships and the mean values were 86% and 88%, respectively, which were in the range of reported values (i.e., 80 and 90%) from the literature [*Hedman and Osterkamp*, 1982; *Hewlett*, 1982; *Texas Forest Service*, 2000]. However, one should use caution when using the mean E_Q value to define perennial streams because E_Q values associated with perennial streamflow depends on the watershed characteristics such as groundwater, land use, soil, vegetation and topography. The

NHD perennial stream length, perennial stream ratio, perennial streamflow and E_Q of perennial streamflow for the study watersheds are listed in Table 4-3.
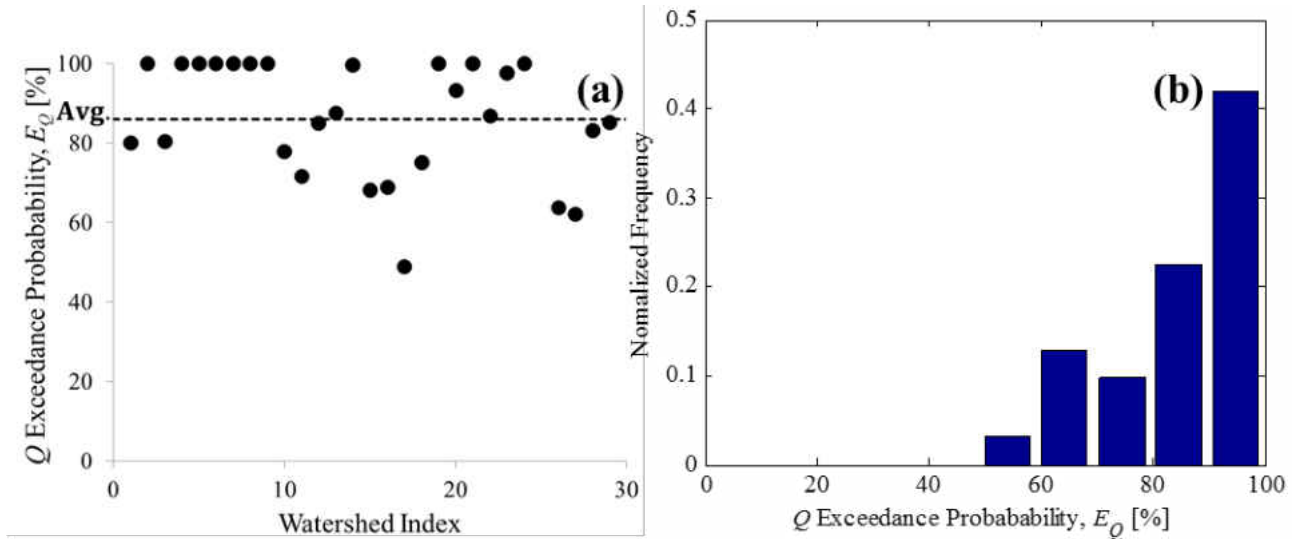

Figure 4-8: (a) Streamflow exceedance probability, E_Q of perennial stream in study watersheds using the relationship between wet channel ratio (α_W) and E_Q; and (b) normalized frequency distribution of E_Q for the all study sites.

Table 4-3: NHD perennial stream length, stream ratio, streamflow and E_Q of perennial streamflow for the study watersheds.

Watershed	NHD Perennial Stream Length [km]	Perennial Stream Ratio [%]	Perennial Streamflow [m³/s]	(i) E_Q of Perennial Streamflow [%]	(ii) E_Q of Perennial Streamflow [%]
Chattahoochee River, GA	167.5	13.50	1.1541	80	90
Ward Creek, CA (Upstream)	5.5	3.33	0.0037	100	97
Blue Springs Creek, AL	25.2	13.40	0.0478	80	78
Cedar Creek, KY	2.3	1.22	0.0009	100	100
Brier Creek, KY	7.1	4.27	0.0056	100	72
Blackwood Creek, CA (2010)	24.8	5.96	0.0466	100	95
Blackwood Creek, CA (2012)	24.8	5.95	0.0466	100	95
Ward Creek, CA (2010)	15.0	5.81	0.0199	100	90

Ward Creek, CA (2012)	15.0	5.81	0.0199	100	90
S F Quantico Creek, VA	13.2	14.27	0.0161	78	80
M Chopawamsic Creek, VA	8.8	16.69	0.0082	72	90
N Chopawamsic Creek, VA	9.5	11.95	0.0092	85	87
S Chopawamsic Creek, VA	3.5	11.18	0.0017	88	99
General Creek, CA	18.1	8.27	0.0272	100	84
Allison Creek, SC	68.3	18.16	0.2551	68	51
Wildcat Creek, SC	31.6	17.87	0.0698	69	72
Pennington Creek, OK	29.9	29.38	0.0636	49	96
Mill Creek, OK	17.5	15.25	0.0259	75	96
Rock Creek, OK	9.9	2.26	0.0099	100	100
Incline Creek, NV (Upstream)	5.4	9.70	0.0036	93	100
North Criner Creek, OK	3.8	4.46	0.0020	100	77
Incline Creek, NV	15.3	11.42	0.0207	87	100
Trout Creek, CA	18.1	8.68	0.0273	98	100
Little Washita River, OK	1.6	2.51	0.0004	100	95
Lake Creek, OK	24.5	20.28	0.0455	64	59
Logan House Creek, NV	4.7	21.18	0.0028	62	73
Glenbrook Creek, NV	6.4	12.49	0.0047	83	88
Eagle Rock Creek, NV	1.8	11.86	0.0005	85	100

(i) E_Q of perennial stream using the relationship between wet channel ratio (α_W) and streamflow exceedance probability, E_Q.

(ii) E_Q of perennial stream using the relationship between streamflow (Q) and wet channel length (L_W).

4.4 Conclusion

The purpose of this study was to assess the streamflow characteristics of perennial streams using the relationship between streamflow exceedance probability (E_Q) and wet channel ratio (α_W) based on wet channel networks extracted from LiDAR data. 30 watersheds were selected based on the available LiDAR data and streamflow observations. A method developed by *Hooshyar et al.* [2015] was utilized for extracting valley and wet channel networks based on LiDAR topographic and intensity information with a spatial resolution of 1-meter.

Using observed streamflows and identified wet channels, the power law relationship between wet channel length and streamflow was derived and the scaling exponent of this relationship was within the range of reported values in the literature. This relationship was converted into non-dimensional form using E_Q and α_W and the previous definition of perennial streams using E_Q values of 90% and 80% corresponded to α_W values of 11% and 15%, respectively. The perennial stream ratio of each study watershed was computed to validate the derived α_W associated with the perennial stream definition and its mean value (i.e., 11%) was within the range of the α_W associated with the definition of perennial streams in this study. Also, the E_Q of perennial streamflow for each watershed was calculated and its mean value (86%) was similar to previous definition values (i.e., 80% and 90%).

Non-dimensional analysis based on the relationship between E_Q and α_W showed results that were consistent with previous research on perennial stream definitions, and demonstrated the potential to apply the α_W as another parameter to define a perennial stream. Also, the relationships found in this study are likely to be applicable in similar climates (e.g., E_P/P: 0.8~2.1). Additional research is needed to develop specific guidelines, including a consistent definition of perennial streams, and how the derived relationships apply to intermittent and ephemeral streams, as well as other climates (e.g. humid and arid).

4.5 References

Abrahams, A. D. (1984), Channel networks: a geomorphological perspective, *Water Resources Research*, *20*(2), 161-188.

Acuña, V., T. Datry, J. Marshall, D. Barceló, C. Dahm, A. Ginebreda, G. McGregor, S. Sabater, K. Tockner, and M. Palmer (2014), Why should we care about temporary waterways, *Science*, *343*(6175), 1080-1081.

Blasch, K. W., T. Ferré, A. H. Christensen, and J. P. Hoffmann (2002), New field method to determine streamflow timing using electrical resistance sensors, *Vadose Zone Journal*, *1*(2), 289-299.

Blyth, K., and J. Rodda (1973), A stream length study, *Water Resources Research*, *9*(5), 1454-1461.

Bowen, Z. H., and R. G. Waltermire (2002), Evaluation of light detection and ranging (LIDAR) for measuring river corridor topography, *Journal of the American Water Resources Association*, *38*(1).

Budyko, M. I. (1958), *The heat balance of the earth's surface*, US Department of Commerce, Washington, DC.

Budyko, M. I. (1974), *Climate and Life*, 508 pp., Academic Press, New York.

Canny, J. (1986), A computational approach to edge detection, *Pattern Analysis and Machine Intelligence, IEEE Transactions on*(6), 679-698.

Chow, V. T., D. R. Maidment, and L. W. Mays (1988), *Applied hydrology*.

Clubb, F. J., S. M. Mudd, D. T. Milodowski, M. D. Hurst, and L. J. Slater (2014), Objective extraction of channel heads from high-resolution topographic data, *Water Resources Research*, *50*(5), 4283-4304.

Day, D. (1978), Drainage density changes during rainfall, *Earth Surface Processes*, *3*(3), 319-326.

Godsey, S., and J. Kirchner (2014), Dynamic, discontinuous stream networks: hydrologically driven variations in active drainage density, flowing channels and stream order, *Hydrological Processes*, *28*(23), 5791-5803.

Goulsbra, C., M. Evans, and J. Lindsay (2014), Temporary streams in a peatland catchment: pattern, timing, and controls on stream network expansion and contraction, *Earth Surface Processes and Landforms*, *39*(6), 790-803.

Gurnell, A. (1978), The dynamics of a drainage network, *Nordic Hydrology*, *9*(5), 293-306.

Hedman, E., and W. Osterkamp (1982), Streamflow characteristics related to channel geometry of streams in western United States, Water Supply Papers-US Geological Survey (USA).

Hewlett, J. D. (1982), *Principles of forest hydrology*, University of Georgia Press.

Hooshyar, M., S. Kim, D. Wang, and S. C. Medeiros (2015), Wet channel network extraction by integrating LiDAR intensity and elevation data, *Water Resources Research*, *51*(12), 10029-10046.

Howard, A. D., and G. Kerby (1983), Channel changes in badlands, *Geological Society of America Bulletin*, *94*(6), 739-752.

Lashermes, B., E. Foufoula-Georgiou, and W. E. Dietrich (2007), Channel network extraction from high resolution topography using wavelets, *Geophysical Research Letters*, *34*(23), L23S04.

Levick, L. R., D. C. Goodrich, M. Hernandez, J. Fonseca, D. J. Semmens, J. C. Stromberg, M. Tluczek, R. A. Leidy, M. Scianni, and D. P. Guertin (2008), *The ecological and hydrological significance of ephemeral and intermittent streams in the arid and semi-arid American southwest*, US Environmental Protection Agency, Office of Research and Development.

Madduma Bandara, C. M. (1974), Drainage density and effective precipitation, *Journal of Hydrology*, *21*(2), 187-190.

Marks, K., and P. Bates (2000), Integration of high-resolution topographic data with floodplain flow models, *Hydrological Processes*, *14*(11-12), 2109-2122.

Meinzer, O. E. (1923), Outline of ground-water hydrology, with definitions, US Govt. Print. Off.

Melton, M. A. (1957), An analysis of the relations among elements of climate, surface properties, and geomorphology, DTIC Document.

Morgan, R. (1972), Observations on factors affecting the behaviour of a first-order stream, *Transactions of the Institute of British Geographers*, 171-185.

NC Division of Water Quality (2010), *Methodology for Identification of Intermittent and Perennial Streams and their Origins, Version 4.11*, North Carolina Department of Environment and Natural Resources, Division of Water Quality. Raleigh, NC.

Orlandini, S., and G. Moretti (2009), Determination of surface flow paths from gridded elevation data, *Water resources research*, *45*(3).

Orlandini, S., P. Tarolli, G. Moretti, and G. Dalla Fontana (2011), On the prediction of channel heads in a complex alpine terrain using gridded elevation data, *Water Resources Research*, *47*(2), W02538.

Passalacqua, P., T. Do Trung, E. Foufoula-Georgiou, G. Sapiro, and W. E. Dietrich (2010), A geometric framework for channel network extraction from lidar: Nonlinear diffusion and geodesic paths, *Journal of Geophysical Research: Earth Surface*, *115*(F1), F01002.

Pelletier, J. D. (2013), A robust, two-parameter method for the extraction of drainage networks from high-resolution digital elevation models (DEMs): Evaluation using synthetic and real-world DEMs, *Water Resources Research*, *49*(1), 75-89.

Rasmussen, C. E. (1999), The infinite Gaussian mixture model, paper presented at NIPS.

Roberts, M. C., and O. Archibold (1978), Variation of drainage density in a small british columbia watershed, edited, Wiley Online Library.

Schumm, S. A. (1956), Evolution of drainage systems and slopes in badlands at Perth Amboy, New Jersey, *Geological society of America bulletin*, *67*(5), 597-646.

Simley, J. (2003), National Hydrography Dataset Newsletter, US Geological Survey Report, Vol. 2.

Sofia, G., P. Tarolli, F. Cazorzi, and G. Dalla Fontana (2011), An objective approach for feature extraction: distribution analysis and statistical descriptors for scale choice and channel network identification, *Hydrol. Earth Syst. Sci.*, *15*(5), 1387-1402.

Svec, J. R., R. Kolka, and J. Stringer (2005), Defining perennial, intermittent, and ephemeral channels in eastern Kentucky: application to forestry best management practices, *Forest Ecology and Management*, *214*(1), 170-182.

Texas Forest Service (2000), Texas Forestry Best Management Practices, online report, http://txforestservice.tamu.edu/uploadedFiles/Sustainable/bmp/Publications/BMP%20Ma nual_Aug2010%20-%20web.pdf.

Whiting, J. A., and S. E. Godsey (2016), Discontinuous headwater stream networks with stable flowheads, salmon river basin, Idaho, *Hydrological Processes*, n/a-n/a.

Wigington, P., T. Moser, and D. Lindeman (2005), Stream network expansion: a riparian water quality factor, *Hydrological Processes*, *19*(8), 1715-1721.

Wolfe, W. L., and G. J. Zissis (1989), *The infrared handbook, ERIM*, 1124-1127 pp.

CHAPTER 5: WETLAND IDENTIFICATION IN THE BARRIER ISLANDS OF EAST-CENTRAL FLORIDA BASED ON THE INTENSITY OF LIDAR RETURNS

5.1 Introduction

Wetlands are vital natural resources for biological diversity and ecosystem processes. Wetlands can recharge groundwater, mitigate flooding, remove pollutants, retain nutrients, and provide wildlife habitat and recreational functions [*Dugan*, 1992]. Wetland hydrology is the most significant factor in its ecosystem function and extent [*Nestler and Long*, 1997]. Small changes in water levels can affect the hydrologic regime and lead to significant changes in ecosystem function and characteristics [*Mitsch and Gosselink*, 2007]. Water levels in wetlands have seasonal variations depending on rainfall events and evapotranspiration, and many wetland areas contain standing water for short periods [*Mitsch and Gosselink*, 2007; *Tiner*, 1999]. Wetland extent and type can vary with climate, topography, land use, and vegetation [*Maxa and Bolstad*, 2009]. Wetlands need to be monitored consistently in order to understand their inundation dynamics, function and health, and wetland mapping is a foundational part of any monitoring programs [*Lang and McCarty*, 2009; *Huang et al.*, 2014].

Despite the importance of wetlands, there are many poorly mapped or totally unmapped wetlands and the minimum area of mapped wetlands are typically 0.5 ha or larger [*Kudray and Gale*, 2000; *Hirano et al.*, 2003]. The U.S. Fish and Wildlife Service began to survey wetlands for the first time in 1954 and classified 20 wetland types using the depth of water or frequency of inundation [*Shaw and Fredine*, 1956]. The National Wetland Inventory (NWI) program has been

providing geospatial wetland data in 1:24,000 scale since the mid -1970s [*Wilen and Bates*, 1995; *Tiner*, 2009]. NWI, generated by aerial photographs and field verification, is one of the most common U.S. wetland maps [*Tiner*, 1999]. The mapping method for NWI requires staff trained in photointerpretation techniques and extensive fieldwork to meet the acceptable accuracy [*Maxa and Bolstad*, 2009] and requires intensive time and effort [*Lang et al.*, 2013]. The vegetation cover is also an important factor in wetland mapping; for instance, palustrine forested wetlands are one of the most difficult wetland types to map because the ground surface is obscured by the canopy [*Tiner*, 1990].

Recent advances in remote sensing technology provide an opportunity to enhance wetland mapping and inventory. Near-infrared (NIR) radiation is reflected by vegetation and dry soil but absorbed by water. Based on the characteristics of NIR and green light, the normalized difference water index (NDWI) was proposed by *McFeeters* [1996] and used for identifying open water features [*Xu*, 2006]. Airborne light detection and ranging (LiDAR) has the potential to improve our understanding of the location and characteristics of wetlands, especially in locations where wetlands are difficult to identify using optical data (e.g., aerial photography) and field work. LiDAR is capable of producing fine spatial resolution data products and its canopy penetration ability helps to detect the properties of the underlying surface. The airborne LiDAR sensor is an active remote sensing technique and emits NIR laser pulses, which are absorbed by or specularly reflected away from the sensor when they strike the water surface [*Wolfe and Zissis*, 1993; *Brzank et al.*, 2008]. The LiDAR return intensity is the relative strength of the reflected signal and the intensity from water surface returns is typically lower than that from dry land surface.

There are a number of recent studies for wetland detection using LiDAR data [*Hogg and Holland*, 2008; *Julian et al.*, 2009; *Lang and McCarty*, 2009; *Maxa and Bolstad*, 2009; *Leonard et al.*, 2012; *Lang et al.*, 2013]. *Lang and McCarty* [2009] showed the potential of LiDAR intensity data for the detection of inundation area beneath a forest canopy. *Maxa and Bolstad* [2009] demonstrated a method for mapping wetland and identifying wetland types from high resolution satellite images and LiDAR-based elevation data. *Leonard et al.* [2012] identified isolated small wetlands using LiDAR data coupled with local relief models that emphasize curvature. *Lang et al.* [2013] developed a wetland mapping method based on a threshold of enhanced topographic wetness index including relief information. The previous research has shown that LiDAR data is very useful as a preliminary result for wetland determinations [*Gillrich and Lichvar*, 2014].

The objective of this paper was to develop a framework to detect wet areas with specific application to wetland identification using the geometric and intensity information in the point cloud generated by LiDAR systems. After masking out areas of dense vegetation, wet areas were identified based on signal intensity of ground returns in barrier islands in East-Central Florida.

5.2 Study Site and Data Sources

5.2.1 Study Site

The 56 km^2 study site is located in northern Merritt Island on the east coast of central Florida as shown in Figure 5-1. Human interventions such as reservoir construction, agriculture, and urbanization are minimal in this area and the dominant upland communities are scrub and pine flat woods [*Provancha et al.*, 1986; *Larson*, 1992]. The climate is generally warm and humid; the

mean maximum temperature is 33 °C in July and the mean minimum temperature is 10 °C in January [*Mailander*, 1990]. Mean annual precipitation from 1888 to 1987 was 1366 ± 256 mm (mean ± SD); the amount of annual rainfall varies broadly from 848 mm to 2075 mm and the wet season occurs from May to October [*Mailander*, 1990].

Figure 5-1: The location and aerial image of the study area in barrier islands in East-Central Florida.

Merritt Island is a barrier island located in broad and flat lowlands, which generally have slow runoff and shallow water tables. Figure 5-2a shows the elevation range in the area, which is

varies between -0.7 m to 7.6 m with an average elevation of 2.3 m relative to sea level datum. The topographic variation in the study area is small and the average slope is 2.2 %.

Most of study area is covered by wetlands, water and non-forested uplands. Non-forested uplands consist of herbaceous and shrub/scrub lands. Figure 5-2b shows the spatial distribution of land-use and land-cover in the study area. The undeveloped area (water, wetland, forest, and non-forested uplands) and developed area (urban and transportation) cover 95% and 5% of the study area, respectively. Developed area is dominated by the runway for Kennedy Space Center (KSC) and roads connected to the runway.
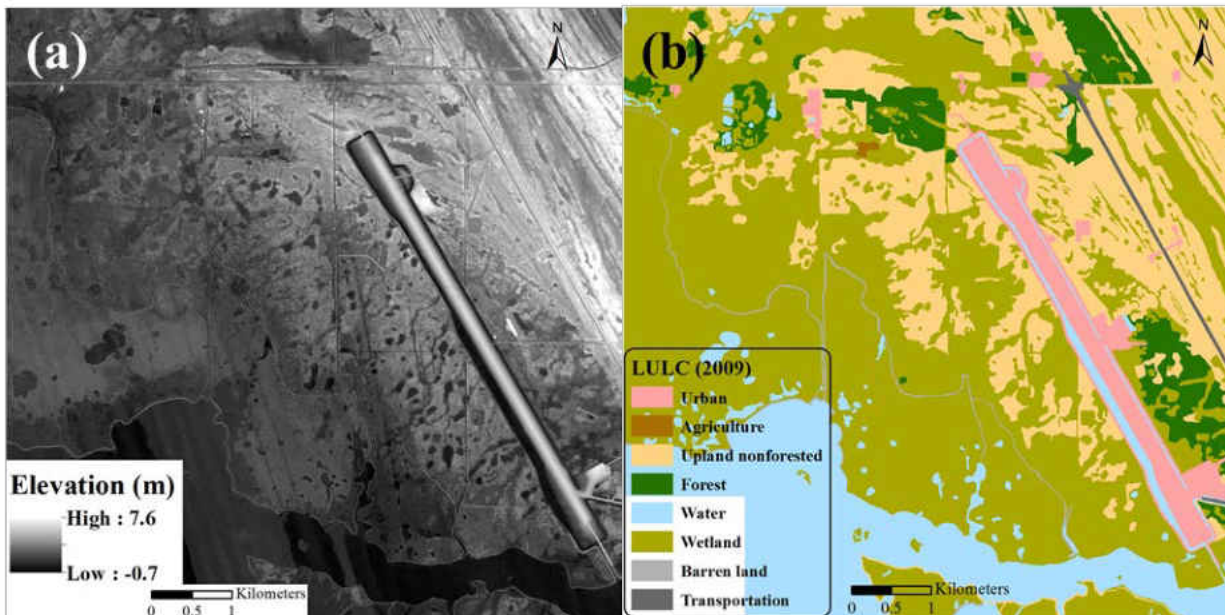
Figure 5-2: (a) Elevation in the study area; and (b) land-use and land-cover map in study area.

5.2.2 LiDAR Data

The study area was selected based on the heavy wetland presence and availability of LiDAR data. The LiDAR survey in this area was conducted on September 16, 2007 using an Optech 3100EA system at an average altitude of 970 m above ground level. There was no precipitation recorded in the 10 days prior to LiDAR acquisition in the study area as shown in Figure 5-3. The relevant attributes of the LiDAR data points used herein included a Global Positioning System (GPS) time stamp, spatial coordinates (X, Y, Z), intensity, scan angle, and return number (first/last return). The average point spacing and average point density of the entire LiDAR point cloud were 0.5 m and 4.0 points/m^2, respectively. The total angular coverage was ±16° and the vertical accuracy was 24 cm [*Dewberry*, 2009]. The bare earth LiDAR points, in which structural components above the Earth's surface such as vegetation and buildings were filtered out by the data provider, were used. The intensity raster and the land surface topography in the study area were derived by processing the bare earth point cloud data using the QCoherent LP360 toolbox for ArcGIS.
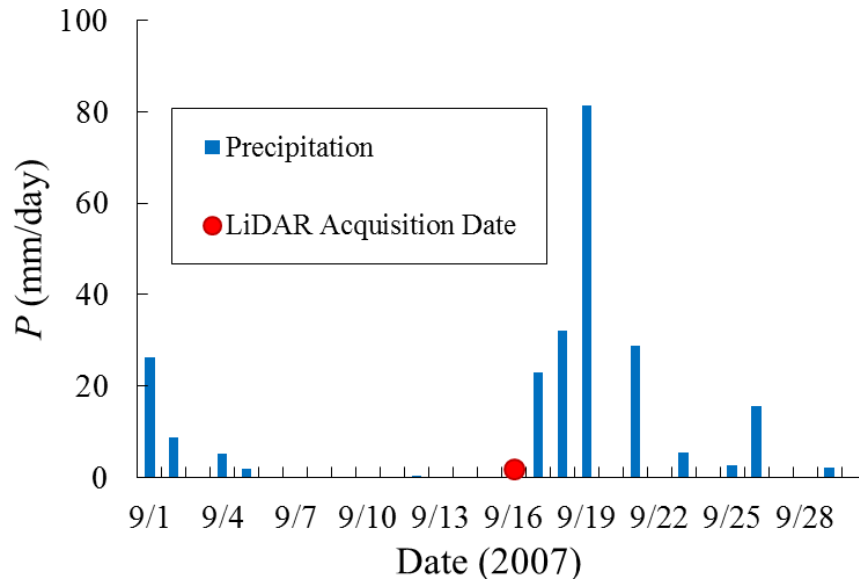
Figure 5-3: Precipitation and LiDAR acquisition date.

5.3 <u>Methodology</u>

The main information used for identifying wet and dry areas was the signal intensity of LiDAR ground returns. LiDAR intensities on water surfaces are typically lower than those on the dry land surface because of the strong absorption of the light energy by water. The returns for water surfaces are usually associated with low signal intensities, dropouts (laser pulse is sent but no or very weak echo is received), and a high relative variation of intensity [*Höfle et al.*, 2009]. The specular reflection from the water surface also contributes to low signal intensity. When the return signal intensity is lower than a threshold, the data point is classified as a dropout and the point density decreases; areas with low point densities are often associated with water surface. Intensity is usually encoded as a DN (digital number) which is a dimensionless measure of the

amount of the relative energy being radiated by a point on a surface. Figure 5-4 shows the intensity image of ground returns for the study area. The intensity value varied from 1 DN (digital number) to 100 DN. As shown in Figure 5-4, the intensity in the wetland, river and canal was much lower than that on road and dry land. In this paper, a systematic procedure was developed to map wetlands based on the intensity of LiDAR ground returns. The first step was to evaluate and exclude the scan angle effect on intensity (section 5.3.1); in the second step dense vegetation was masked out of the intensity maps (section 5.3.2); and the last step was to decompose the composite probability distribution function of intensity and identify the wet areas based on the intensity threshold [*Hooshyar et al.*, 2015].
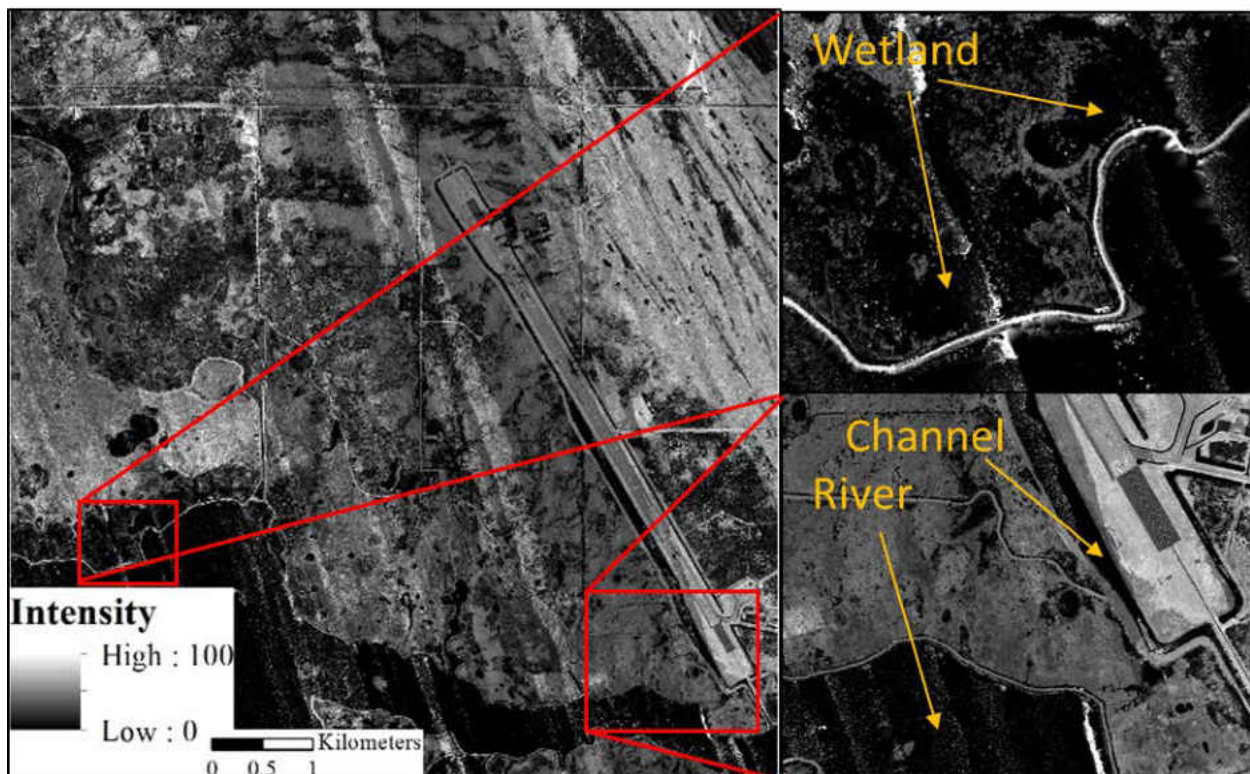
Figure 5-4: LiDAR intensity map and zoom-in area for wetland, cannel and river in the study area.

5.3.1 Scan Angle Effect on Intensity

LiDAR intensity on water surfaces generally can be relatively high when the scan angle is at nadir (directly beneath the aircraft and normal to the water surface). Such signal saturation has the potential to introduce error into the estimation of wet and dry areas. In order to evaluate the scan angle effect on intensity in the study area, multiple sample sites were generated to explore the characteristics of intensity on wet and dry surfaces. Polygons were generated for each sample sites as shown in Figure 5-5a. The sample sites for wet areas were generated on stream and canal areas because they exhibit a predictable, continuous low intensity pattern. The sample sites for dry areas were selected on the road, dry ground or places where it was unclear whether the site was dry or wet. Figure 5-5b and Figure 5-5c illustrates the sample site selection methodology. A total 730 sample sites (395 wet and 335 dry) were generated for analysis in this study (Figure 5-5a).
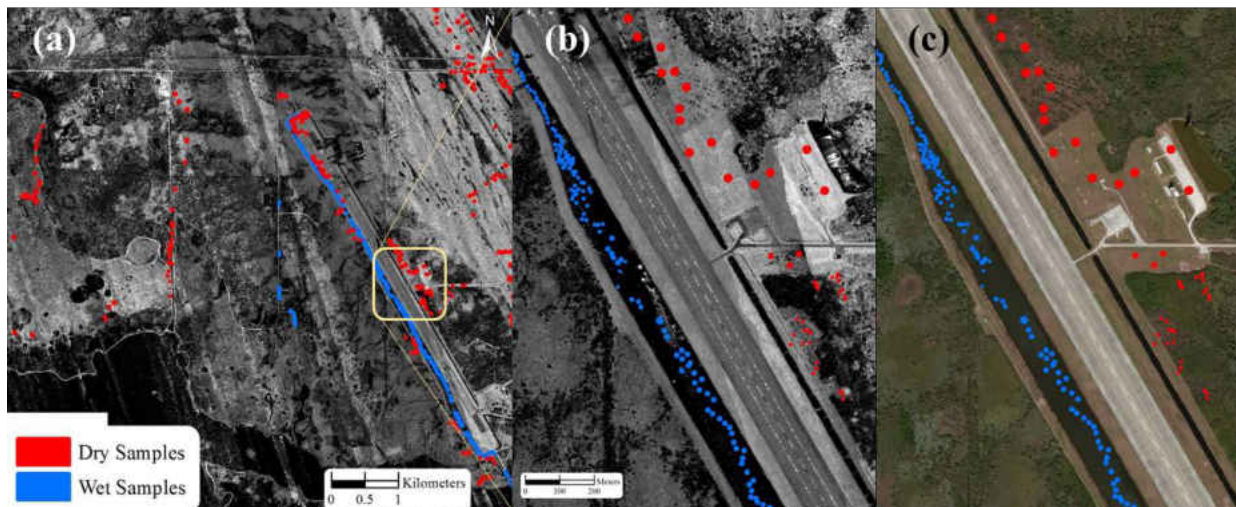
Figure 5-5: (a) location of total sample sites; (b) sample sites for the zoom-in area; (c) aerial image for the zoom-in area.

The intensity statistics of the identified wet and dry samples were collected for the LiDAR snapshot. Figure 5-6 shows that the intensity values in wet areas (Figure 5-6a) as a function of scan angle on water surface in the study area is more significant than in dry areas (Figure 5-6b). The intensities of some returns from the water surface higher than 100 DN when the scan angles were less than 3°. These water surface returns with high intensity will pollute the subsequent statistics and must be filtered out. Therefore, the returns with scan angle less than 3° and intensity higher than 100 DN were removed when the intensity map was generated.
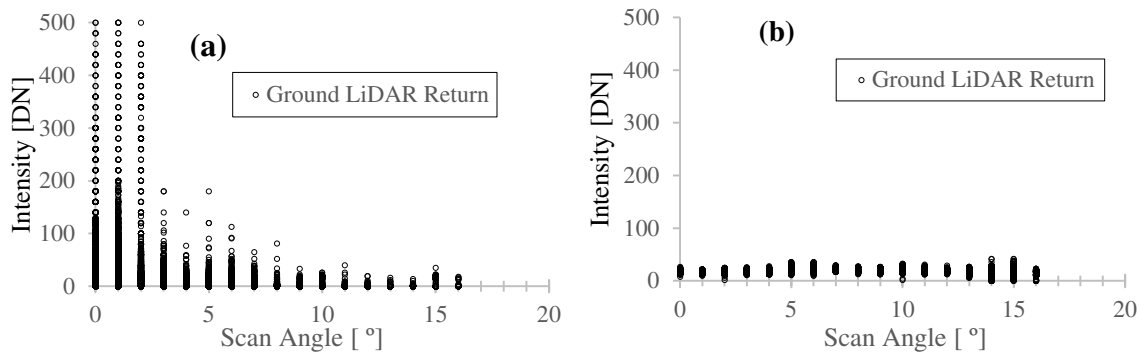
Figure 5-6: Scan angle effect of signal intensity on wet channels in the study area: (a) wet samples; (b) dry samples.

5.3.2 Masking Dense Vegetation in Intensity Maps

LiDAR point cloud data have multiple returns from co-located surfaces at different elevations and each point includes both intensity and elevation information. At a minimum, there

is generally a ground return and canopy return from any laser pulse. For example, Figure 5-7 shows an aerial image of vegetated area (Figure 5-7a) in this study site, intensity from top of the canopy (Figure 5-7b) and ground surface (Figure 5-7c). As shown in Figure 5-7c, the intensity of ground surface under canopy was relatively low and similar to the intensity of wet surface due to the absorption of near-infrared light by vegetation. Therefore, densely vegetated areas can be misleading for classifying wet surfaces and need to be masked from the intensity map to improve the performance of wet surface identification. The densely vegetated areas were classified as such when the ground elevation (h_g) was significantly lower than the canopy elevation (h_c), evaluated using Equation (5-1) where a pixel p is densely vegetated if the following condition is satisfied:

$$h_c(p) \geq h_g(p) + h_T \tag{5-1}$$

where h_T is a minimum height of canopy and is set to 2 m in this study. Figure 5-7d shows the identified densely vegetated areas that were filtered out from the intensity map and excluded for extraction of wet areas.
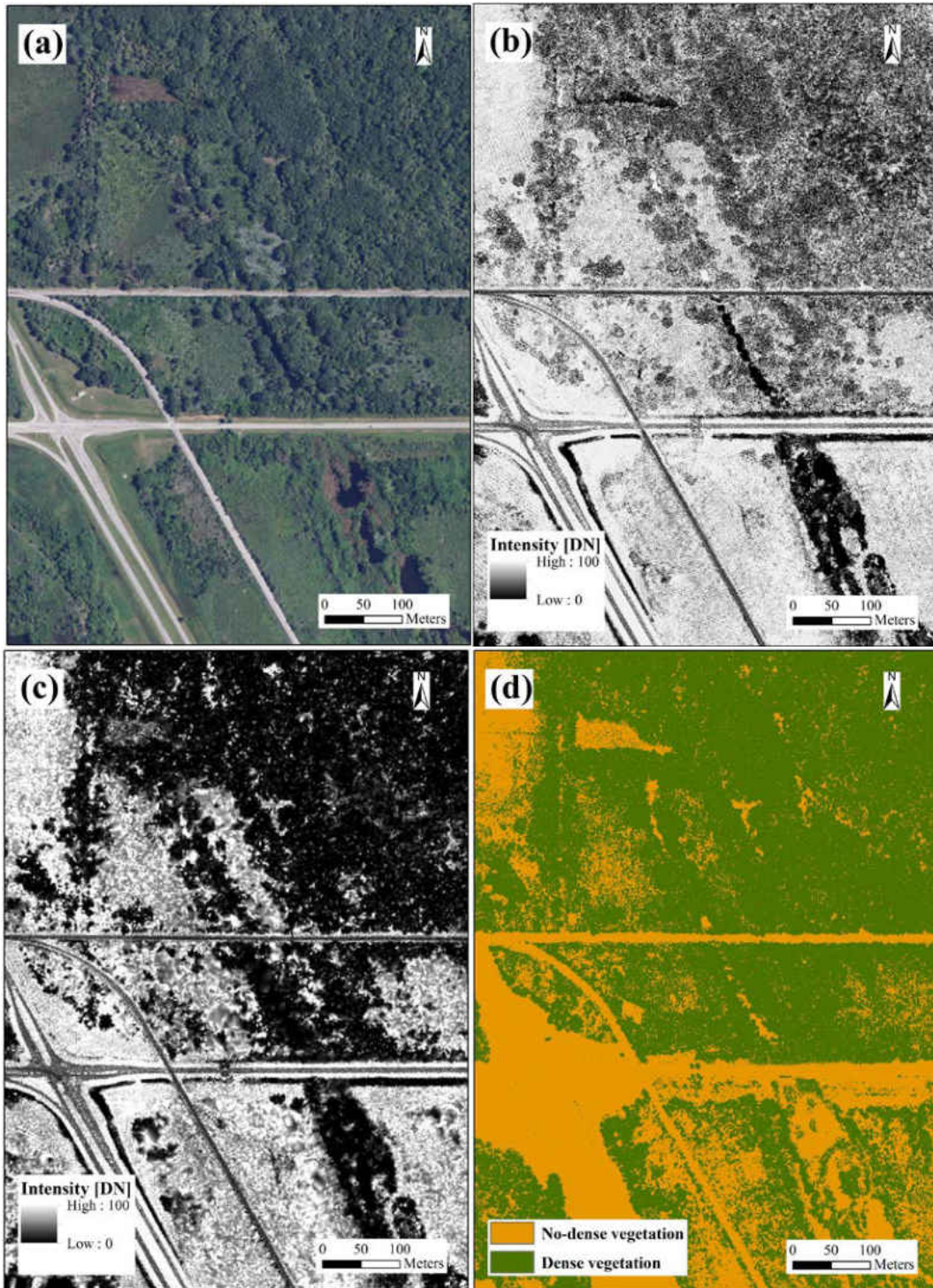
Figure 5-7: (a) Aerial image for a selected space. The intensity of returns from (b) the top of canopy and (c) the ground surface. (d) The extent of dense vegetation.

5.3.3 Decomposing Composite PDF of Intensity

The intensity of LiDAR returns from dry surfaces is comparatively higher than wet surfaces. If the intensity from a single type of surface (wet or dry) follows a Gamma distribution, the overall probability distribution function (PDF) of intensity represents a multimodal distribution. The overall PDF of intensity shows the variation over the land surface and is derived from a frequency analysis of the intensity map. Each mode of the overall PDF is associated with a type of ground surface such as wet or dry. The overall PDF can be represented by a Gamma mixture model which is a generative model for a mixture of several individual Gamma distributions. The general description of a Gamma mixture model is similar to a Gaussian mixture model (GMM) and is given by Equation (5-2) [*Rasmussen*, 1999] :

$$f(x|k_1, \dots, k_N, \theta_1, \dots, \theta_N, w_1, \dots, w_N) = \sum_{i=1}^{N} w_i \times G(x|k_i, \theta_i) \tag{5-2}$$

where f is the Gamma mixture distribution; $G(k_i, \theta_i)$ is an individual Gamma distribution for the mode i with shape parameter k_i and scale parameter θ_i. w_i represents the corresponding weight or proportion of the mixture distribution and w_i sums to unity for all values of i.

The Expectation-Maximization (EM) algorithm [*Moon*, 1996] was utilized to estimate the mean, standard deviation and weight corresponding of the individual Gamma distributions. The number of iterations of the EM algorithm was set to 1.5×10^4 and the tolerance was 1×10^{-8}.

The decomposed intensity PDFs of wet and dry areas were generated and one threshold, I_W, was identified to differentiate wet and dry surfaces. I_W was defined as the intensity at the intersection of the wet and dry PDFs. Figure 5-8a graphically shows the individual PDFs and the

threshold for wet pixels. The membership probability for each pixel was calculated by Equation (5-3):

$$P(c \in k|I_c) = \frac{w_j \times G(x|k_j, \theta_j)}{\sum_{i=W,D} w_i \times G(k_i, \theta_i)}, j = W, D \tag{5-3}$$

where $P(c \in k|I_c)$ represents the probability of pixel c with intensity value I_c and is a member of mode (i.e., cluster) j. j can be either of wet (W) or dry (D) modes. The membership probabilities of the wet and dry mode are shown in Figure 5-8b.
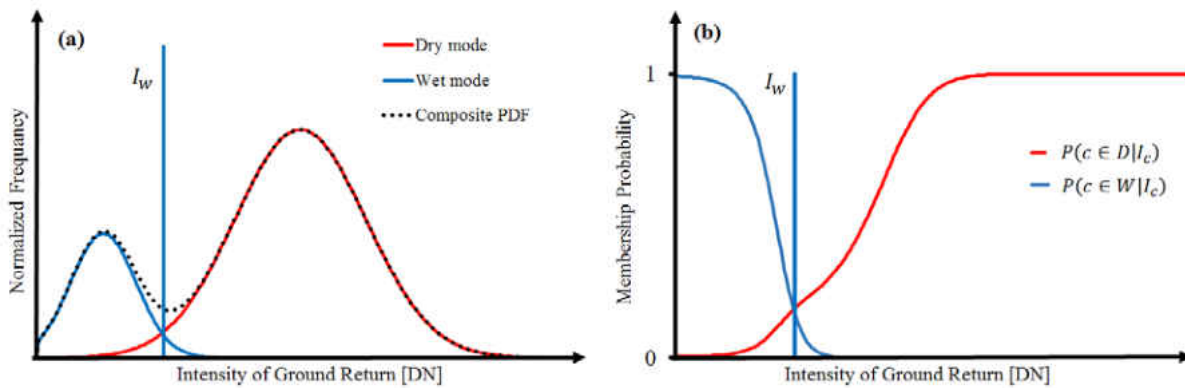
Figure 5-8: (a) A schematic representation of the composite and the individual PDFs of intensity return along with the wet (I_W) threshold. (b) The membership probability of each mode.

5.4 Results and Discussion

Wet and dry surfaces were detected using 1-m DEM and intensity grid generated from the ground returns. By decomposing the overall PDF of intensity using the methodology explained above, the intensity PDFs of wet and dry modes were extracted and the threshold I_W was identified as 6 DN shown in Figure 5-9. Figure 5-10a is an aerial image for a selected region in the study area with straight channels along the road and vegetation areas. Figure 5-10b is the corresponding

intensity image and illustrates the low intensity pattern in the channels and parts of vegetation areas. The wet surfaces and wet channel segments in the image had lower intensities than the surrounding lands. This intensity image was classified into three categories; Vegetation, Wet and Dry; based on the intensity threshold established after the vegetation masking process. Figure 5-10c shows the classified land surface based on the intensity image shown in Figure 5-10b. Most of channel areas, wetlands and surface impoundments in Figure 5-10c were classified as wet, and the areas under dense canopy were classified as vegetation. Roads, levees and dry surfaces were classified as dry.
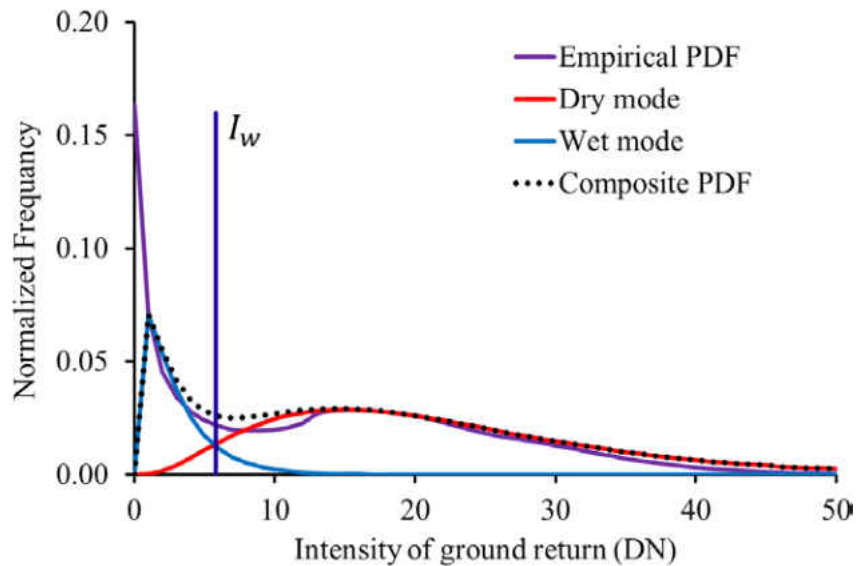
Figure 5-9: The multimodal PDF of intensity returns and the extracted individual distributions representing wet and dry modes for study area.
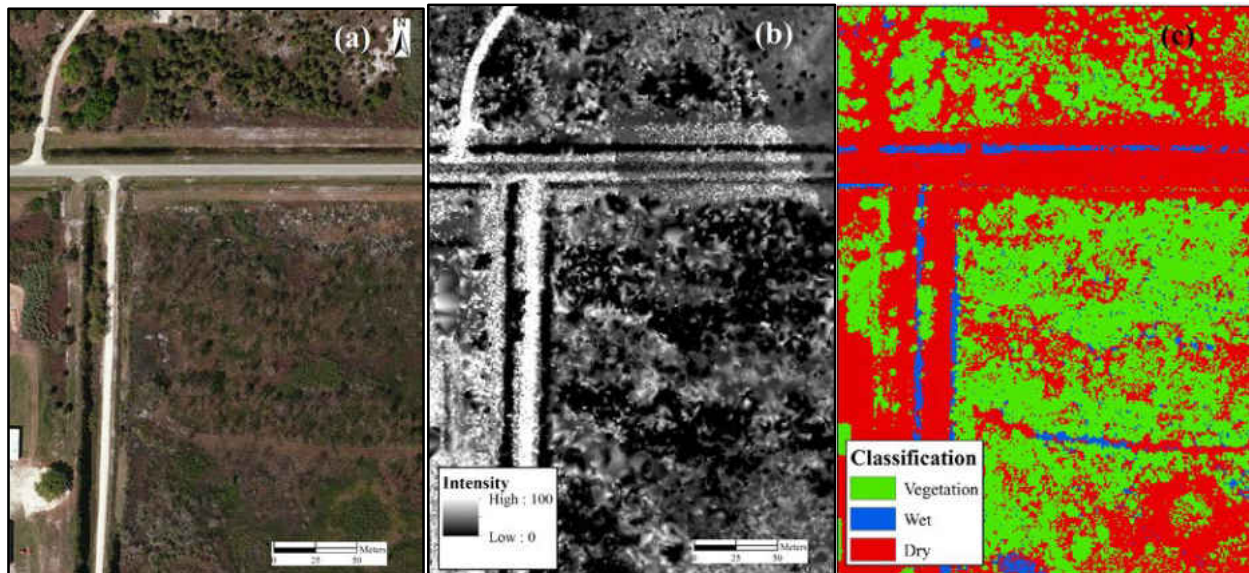
Figure 5-10: (a) aerial image for a selected space in the study area; (b) intensity image for a selected space based on the LiDAR data; (c) classified three categories of land surface (Vegetation, Wet and Dry).

Figure 5-12a shows the wetland areas identified by the U.S. Fish and Wildlife Service National Wetland Inventory (NWI) in study area. This NWI map included wetlands as well as deeper waters such as ponds, lakes, rivers and creeks. To investigate the accuracy of the NWI map, a sample area with wetlands and deep waters was selected. Figure 5-11b and Figure 5-11c shows the NWI map and the aerial image for the zoom-in area, respectively. The wetland areas identified in the NWI showed poor consistency with the aerial image, mainly because wetland extents are generally dynamic in response to hydrologic conditions such as water table elevation and prior precipitation; NWI wetlands were identified based on the maximum flooded static areas. However, the pattern of ponds, lakes and rivers from the aerial image was similar to NWI map because their extents are less dynamic than wetlands. Therefore, the deep waters from NWI were used to validate the LiDAR-derived wet areas. Figure 5-11d shows the three categories of land

117

surface with LiDAR data using the methodology described above and shows good agreement with the aerial image. However, the wetland areas are dynamic depending on the conditions and NWI wetlands are the extreme flooded areas, therefore a simple comparison of both maps will not result in meaningful insights.

The membership probability for each pixel was computed using Equation (5-3) and dense vegetation areas were excluded from the calculation. The membership probabilities of the wet area for each pixel are shown in Figure 5-11e. 0% and 100% probabilities corresponded to totally dry and wet areas, respectively. Pixel intensity on wet surfaces was less than or equal to the identified wet threshold (I_W) but there were some edge cases where a dry surface produced an intensity below the threshold, typically when the wet membership probability was less than 100%. Likewise, pixel intensity on dry surfaces was higher than I_W but they could similarly be wet based on their dry membership probability. Thus, based on the intensity values, pixels could have been misclassified due to the inherent uncertainty.
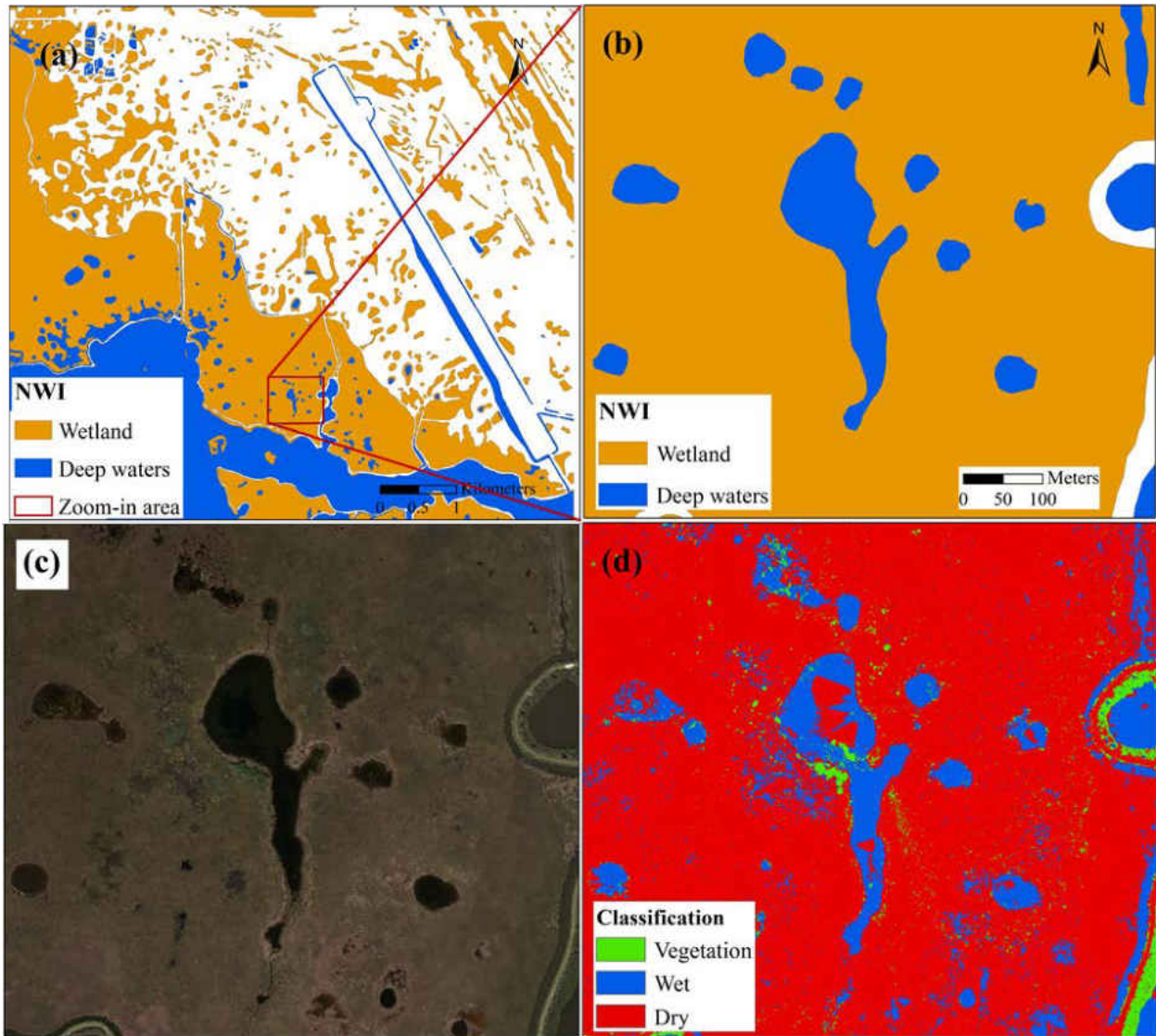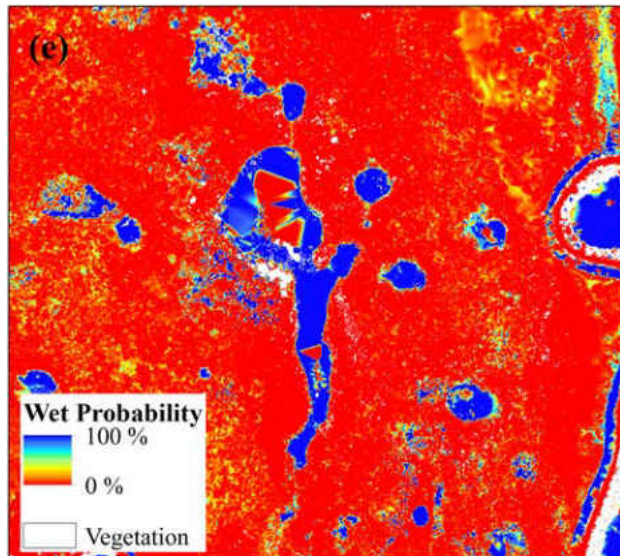
Figure 5-11: (a) Wetlands and deep water such as river, channel, lake and pond identified by NWI in study area; (b) wetlands and deep water by NWI for the zoom-in area; (c) aerial image; (d) classified three categories of land surface (Vegetation, Wet and Dry); (e) membership probability for wet area.

Figure 5-12a shows the three categories (Vegetation, Wet and Dry) of land surface and Figure 5-12b shows the membership probability for wet area. Wet areas derived from LiDAR data are only valid for the time when the LiDAR survey is performed. The vegetation areas may be wet or dry area but at this time their wet or dry state cannot be reliably predicted using this method.
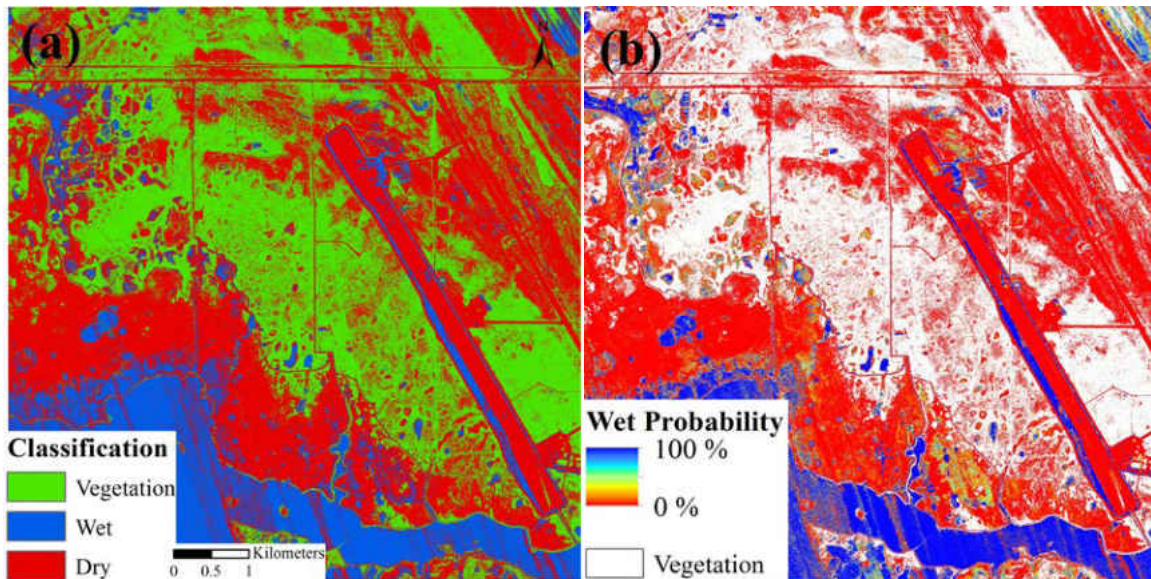
Figure 5-12: (a) classified three categories of land surface in study area (Vegetation, Wet and Dry); (b) membership probability for wet area.

The systematic method for mapping wet areas was applied to Merritt Island in East-Central Florida with all available 2007 LiDAR data. Figure 5-13 shows the location of the subject barrier islands (Figure 5-13a) and ground return intensity of 2007 LiDAR (Figure 5-13b). There were no LiDAR data available over the water surface associated with of Mosquito lagoon (middle of upper area) and Banana river (middle of lower area); however, this did not affect the identification of wet/dry area. The intensity image was classified into three categories (Vegetation, Wet and Dry) based on the intensity threshold and elevation data. Figure 5-13c shows the classified land surface based on the intensity image shown in Figure 5-13b. Rivers, wet channels, and wetlands were all included as wet areas.
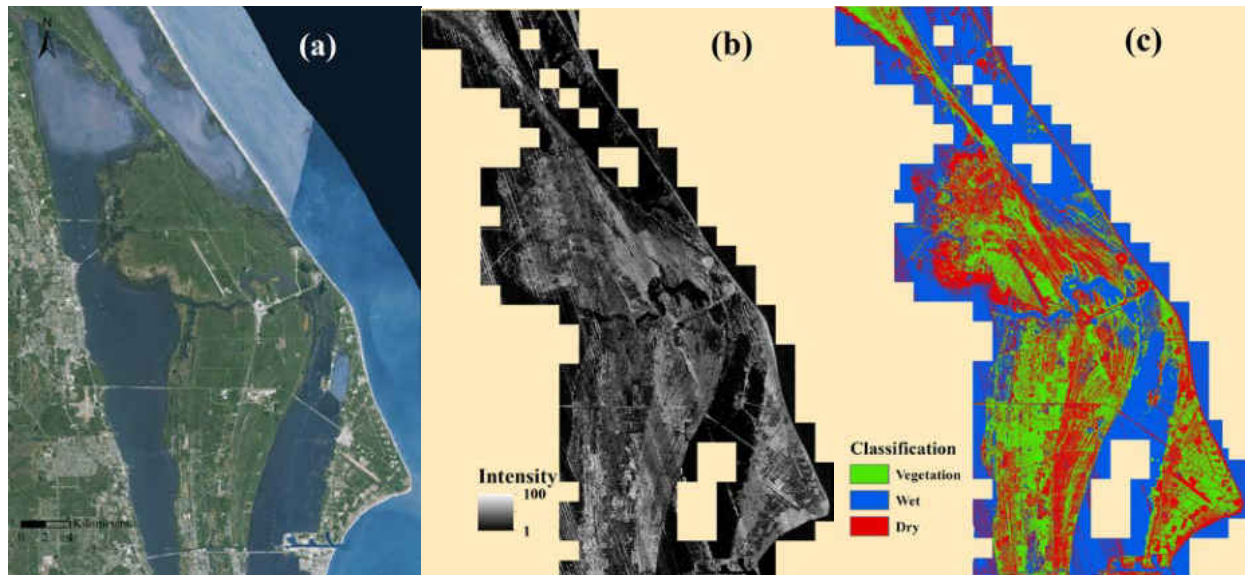
Figure 5-13: Map for Merritt Island with total available LiDAR data; (a) satellite image of Merritt Island area; (b) intensity image based on the 2007 LiDAR data; (c) classified three categories of land surface (Vegetation, Wet and Dry).

5.5 Summary and Future Research

LiDAR provides an interesting opportunity for mapping the wetland because of the high spatial resolution and the signal penetration through the canopy. This study demonstrated the potential of LiDAR for wetland mapping. A systematic method was developed for mapping the wet area based on LiDAR elevation and intensity information. Ground intensity information below dense vegetation was not descriptive enough to extract wet areas, thus dense vegetation locations were filtered out of the detection areas. The method exploited the differences between LiDAR return intensities from wet and dry surfaces; LiDAR intensities on water surfaces are generally lower than those on the dry land surface due to the strong absorption and / or specular reflection of the light energy by the water. The intensity threshold used to identify wet surfaces

was identified by decomposing the composite PDF of intensity using a Gamma mixture model and the Expectation-Maximization algorithm.

The proposed method for identifying wet areas is applicable to other regions with varying climatic and topographic gradients. Field and LiDAR surveys can proceed simultaneously to validate the developed method. Also, the more detailed study of wetland dynamics is possible if there are the multiple or regular LiDAR acquisitions. In the future, the water penetration limitation of NIR LiDAR can be overcome by incorporating green LiDAR. The green LiDAR signal can penetrate water surface and the returns can provide water depth information that can be used to track bathymetric morphology. All of these possibilities stand to enhance the understanding wetland characteristics and the accuracy of wetland mapping using readily available LiDAR data.

5.6 <u>References</u>

Brzank, A., C. Heipke, J. Goepfert, and U. Soergel (2008), Aspects of generating precise digital terrain models in the Wadden Sea from lidar–water classification and structure line extraction, *ISPRS Journal of Photogrammetry and Remote Sensing*, *63*(5), 510-528.

Dewberry (2009), *LiDAR, Breaklines and Contours for Brevard County, Florida*, State of Florida Division of Emergency Management, Contract: 07-HS-34-14-00-22-469.

Dugan, P. (1992), *Wetlands in danger*, Mitchell Beazley London Ltd.

Gillrich, J., and R. Lichvar (2014), *Use of LiDAR to Assist in Delineating Waters of the United States, Including Wetlands*, US Army Engineer Research and Development Center.

Hirano, A., M. Madden, and R. Welch (2003), Hyperspectral image data for mapping wetland vegetation, *Wetlands*, *23*(2), 436-448.

Höfle, B., M. Vetter, N. Pfeifer, G. Mandlburger, and J. Stötter (2009), Water surface mapping from airborne laser scanning using signal intensity and elevation data, *Earth Surface Processes and Landforms*, *34*(12), 1635-1649.

Hogg, A., and J. Holland (2008), An evaluation of DEMs derived from LiDAR and photogrammetry for wetland mapping, *The Forestry Chronicle*, *84*(6), 840-849.

Hooshyar, M., S. Kim, D. Wang, and S. C. Medeiros (2015), Wet channel network extraction by integrating LiDAR intensity and elevation data, *Water Resources Research*, *51*(12), 10029-10046.

Huang, C., Y. Peng, M. Lang, I.-Y. Yeo, and G. McCarty (2014), Wetland inundation mapping and change monitoring using Landsat and airborne LiDAR data, *Remote Sensing of Environment*, *141*, 231-242.

Julian, J. T., J. A. Young, J. W. Jones, C. D. Snyder, and C. W. Wright (2009), The use of local indicators of spatial association to improve LiDAR-derived predictions of potential amphibian breeding ponds, *Journal of geographical systems*, *11*(1), 89-106.

Kudray, G. M., and M. R. Gale (2000), Evaluation of National Wetland Inventory maps in a heavily forested region in the upper Great Lakes, *Wetlands*, *20*(4), 581-587.

Lang, M. W., and G. W. McCarty (2009), Lidar intensity for improved detection of inundation below the forest canopy, *Wetlands*, *29*(4), 1166-1178.

Lang, M. W., G. McCarty, R. Oesterling, and I.-Y. Yeo (2013), Topographic metrics for improved mapping of forested wetlands, *Wetlands*, *33*(1), 141-155.

Larson, V. L. (1992), *A method of assessing the conservation value of natural communities at a local scale*, MS thesis, Florida Institute of Technology, FL.

Leonard, P. B., R. F. Baldwin, J. A. Homyack, and T. B. Wigley (2012), Remote detection of small wetlands in the Atlantic coastal plain of North America: Local relief models, ground validation, and high-throughput computing, *Forest Ecology and Management*, *284*, 107-115.

Mailander, J. L. (1990), *Climate of the Kennedy Space Center and vicinity*, NASA Tech. Memo., 103498, 57 pp.

Maxa, M., and P. Bolstad (2009), Mapping northern wetlands with high resolution satellite images and LiDAR, *Wetlands*, *29*(1), 248-260.

McFeeters, S. (1996), The use of the Normalized Difference Water Index (NDWI) in the delineation of open water features, *International journal of remote sensing*, *17*(7), 1425-1432.

Mitsch, W. J., and J. G. Gosselink (2007), *Wetlands*, 4th ed., John Wiley and Sons, Inc., N.Y., USA.

Moon, T. K. (1996), The expectation-maximization algorithm, *Signal processing magazine, IEEE*, *13*(6), 47-60.

Nestler, J. M., and K. S. Long (1997), Development of hydrological indices to aid cumulative impact analysis of riverine wetlands, *Regulated Rivers: Research & Management*, *13*(4), 317-334.

Provancha, M. J., P. A. Schmalzer, and C. R. Hinkle (1986), *Vegetation types, John F. Kennedy Space Center*, Biomedical Operations and Research Office, NASA, Kennedy Space Center, FL.

Rasmussen, C. E. (1999), The infinite Gaussian mixture model, paper presented at NIPS.

Shaw, S. P., and C. G. Fredine (1956), *Wetlands of the united states: Their extent and their value to waterfowl and other wildlife*, United State Department of the Interior, Washington, DC, p. 67.

Tiner, R. W. (1990), Use of high-altitude aerial photography for inventorying forested wetlands in the United States, *Forest Ecology and Management*, *33*, 593-604.

Tiner, R. W. (1999), *Wetland indicators: A guide to wetland identification, delineation, classification, and mapping*, CRC Press.

Tiner, R. W. (2009), *Status report for the National Wetlands Inventory program: 2009*, US Department of the Interior, Fish and Wildlife Service, Division of Habitat and Resource Conservation, Branch of Resource and Mapping Support, Arlington.

Wilen, B. O., and M. Bates (1995), The US fish and wildlife service's national wetlands inventory project, in *Classification and inventory of the world's wetlands*, edited, pp. 153-169, Springer.

Wolfe, W. L., and G. J. Zissis (1993), *The Infrared Handbook*, Environmental Research Institute of Michigan, IRIA Series in Infrared and Electro Optics, Ann Arbor, MI.

Xu, H. (2006), Modification of normalised difference water index (NDWI) to enhance open water features in remotely sensed imagery, *International Journal of Remote Sensing*, *27*(14), 3025-3033.

CHAPTER 6: CONCLUSION

6.1 Conclusion

The objective of this dissertation was to evaluate the hydroclimatic controls on drainage network dynamics and characterize the variation of drainage density in various climate regions. To this end, the study watersheds were selected based on the availability of streamflow observations and LiDAR data. LiDAR data were acquired, processed and applied for generating intensity maps and land surface topography with a spatial resolution of 1-meter. Climate aridity index (E_P/P) was used as a quantitative indicator for climate.

In the study, methods were developed to extract the valley and wet channel networks using LiDAR data. A curvature-based method, incorporating both positive and negative curvature information, was developed to extract a valley (drainage) network from LiDAR-based DEMs; wet channel networks were mapped based on a statistical detection framework using the elevation and intensity information.

This research revisited the influence of climate controls on drainage density based on 121 watersheds with minimal to no anthropogenic intervention across the climate gradient and drainage density was calculated by valley networks extracted using the topographic curvature threshold from 1-m LiDAR based DEMs. The relationship between drainage density and climate aridity index showed a monotonic increasing trend; while the previous studies from *Melton* [1957] and *Madduma Bandara* [1974] showed a U-shaped relationship. This discrepancy was explained by two factors: 1) the humid watersheds from *Madduma Bandara* [1974] were modified by extensive

human interferences from a tea plantation; and 2) the drainage densities from *Melton* [1957] were underestimated due to the coarse spatial resolution (30-meter) of the topographic maps. Meanwhile, we found that the negative correlation between drainage density and drainage area only occurs in arid regions.

In situ observations of wet channel networks are limited in headwater catchments in comparison with the importance of the dynamics of stream network expansion and contraction. The systematic method was developed to map wet channel networks by integrating elevation and signal intensity of ground returns. The signal intensity thresholds for identifying wet channels were extracted from frequency distributions of intensity return. The developed method was applied to the Lake Tahoe area based on eight LiDAR snapshots during recession periods in five watersheds. A power-law relationship between streamflow and flowing channel length during the recession period was derived based on these results. The scaling exponent was within the range of reported values from fieldwork in other regions.

The streamflow characteristics of perennial streams were assessed using the relationship between streamflow exceedance probability (E_Q) and wet channel ratio (α_W) based on wet channel networks extracted from LiDAR data. Non-dimensional analysis based on the relationship between E_Q and α_W showed consistent results with previous researches about perennial stream definition, and provided the possibility to use α_W as another indicator to define a perennial stream.

A detection framework for wet area to aid in wetland mapping was developed based on LiDAR elevation and intensity information. The method utilized differences between LiDAR return intensities from water and dry surfaces to detect wet areas after masking out densely vegetated areas extracted from LiDAR topographic information for barrier islands in East-Central

Florida. The intensity threshold for wet surfaces was identified by decomposing the composite PDF of intensity using a Gamma mixture model and the Expectation-Maximization algorithm. This method showed the potential for wetland mapping.

The methodologies in this dissertation demonstrated that incorporating LiDAR data into the mapping of drainage networks, stream network dynamics and wetlands will enable a much deeper understanding of hydroclimatic controls on steam network dynamics. LiDAR data provide rich, readily available sources of information including elevation and intensity, and are of great benefit to the hydrologic research community.

6.2 Future Research

As an extension to this research, topographic features such as slope, drainage area, topographic curvature, topographic index, and others can be extracted for the valley heads, channel heads, perennial stream heads, and wet channel heads. Properties of the topographic features from each head can be quantified and the potential patterns of these properties over time across climate gradients will be evaluated.

In addition, climate controls on perennial and temporal (intermittent and ephemeral) streams, and their density can be quantified using the LiDAR-based drainage networks. Perennial and temporal streams can be defined based on the relationship between streamflow exceedance probability and wet channel ratio (i.e. wet channel length over total drainage length). Perennial streams reflect a hydrologic response to the climate at the mean annual scale and temporal streams depend on the seasonal and event scale. Therefore, the climate seasonality control on intermittent streams and the storminess control on ephemeral streams can be quantified.

6.3 <u>References</u>

Madduma Bandara, C. M. (1974), Drainage density and effective precipitation, *Journal of Hydrology*, *21*(2), 187-190.

Melton, M. A. (1957), An analysis of the relations among elements of climate, surface properties, and geomorphology, DTIC Document.

Appendix A: Connected Wet Channel and Valley Network in Study Sites
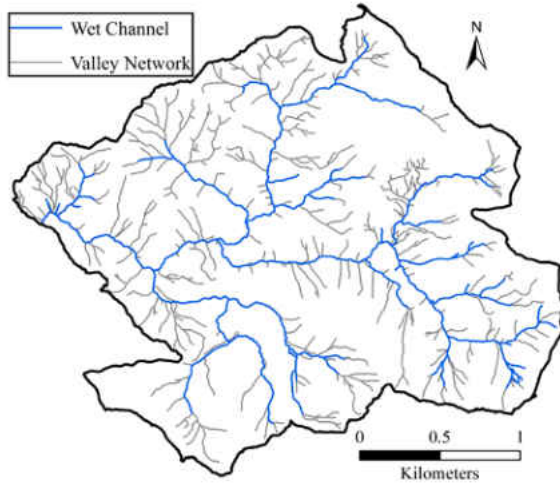
Figure A- 1: Tucca Creek, OR

Figure A- 2: Schafer Creek, OR
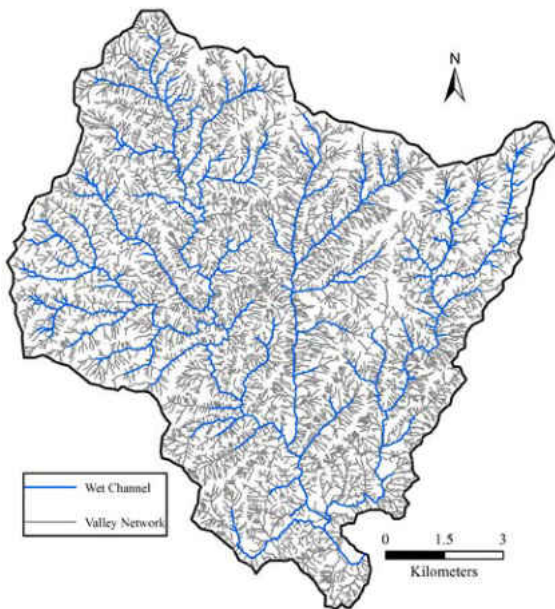
Figure A- 3: Chattahoochee River, GA
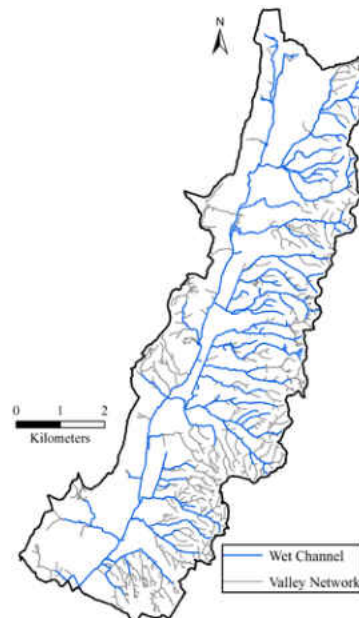
Figure A- 4: Blue Springs Creek, AL
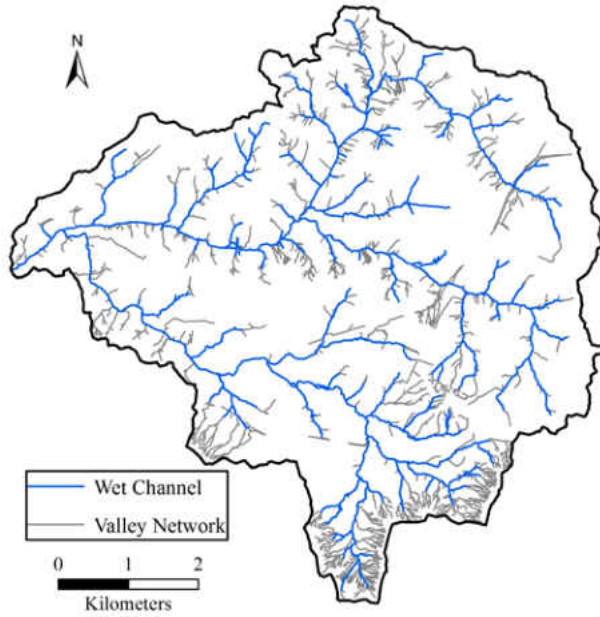
Figure A- 5: Cedar Creek, KY
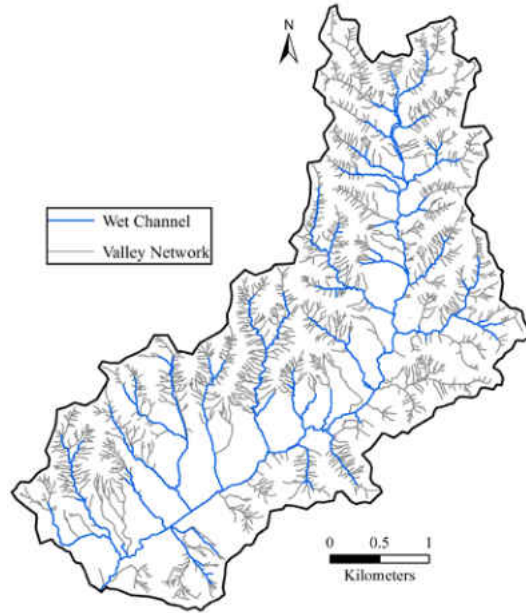
Figure A- 6: Brier Creek, KY
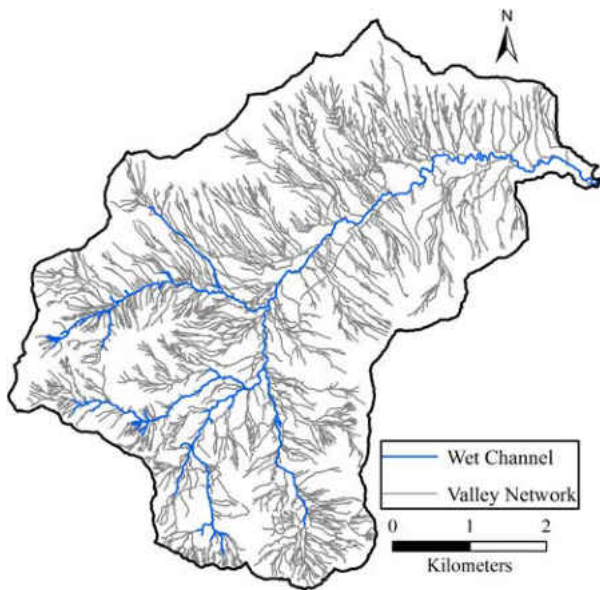
Figure A- 7: Blackwood Creek (2010), CA
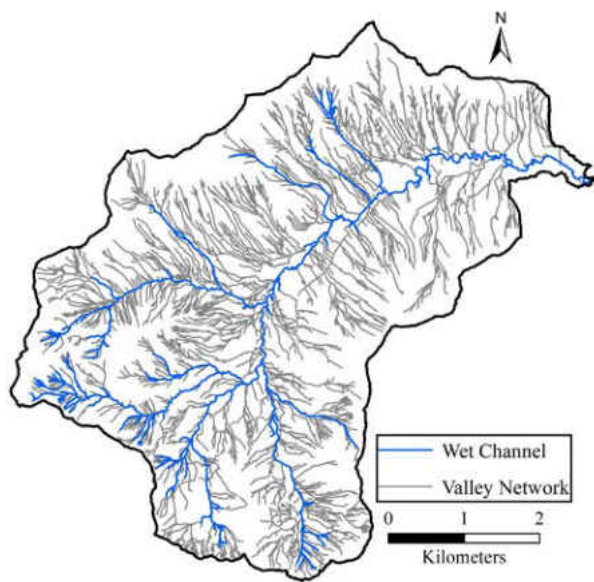
Figure A- 8: Blackwood Creek (2012), CA
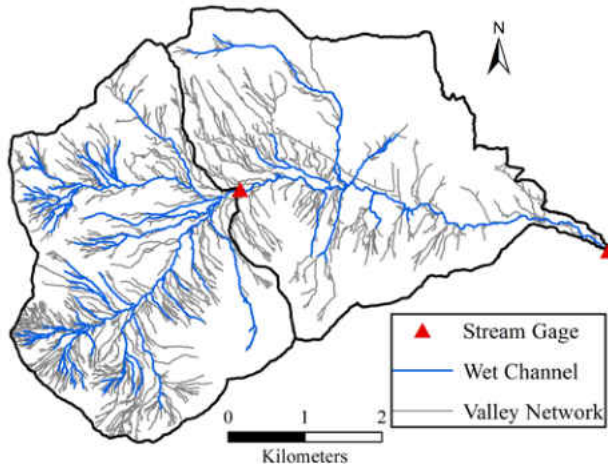
Figure A- 9: Ward Creek (2010), CA
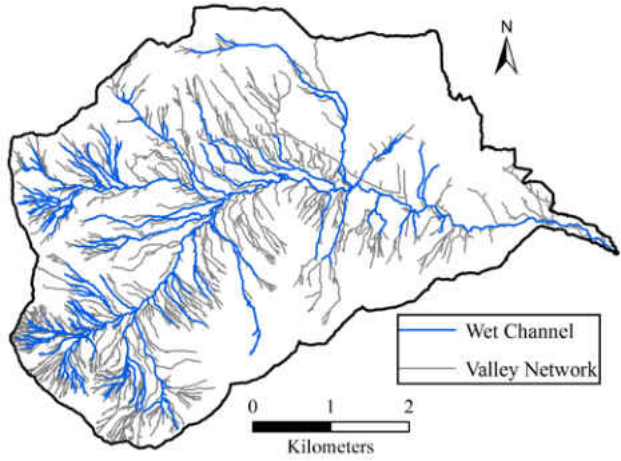
Figure A- 10: Ward Creek (2012), CA
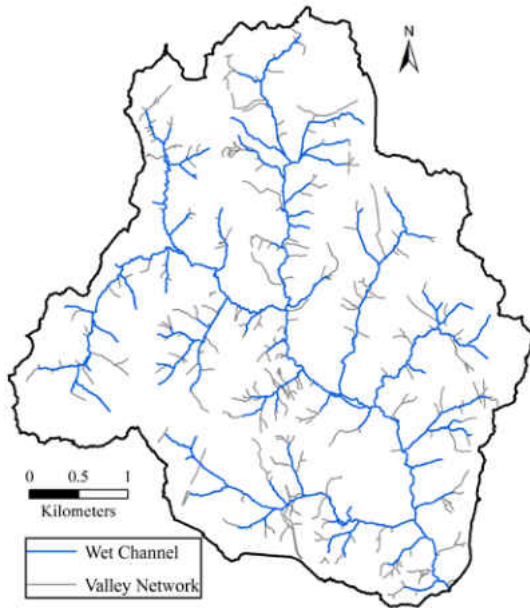
Figure A- 11: S F Quantico Creek, VA
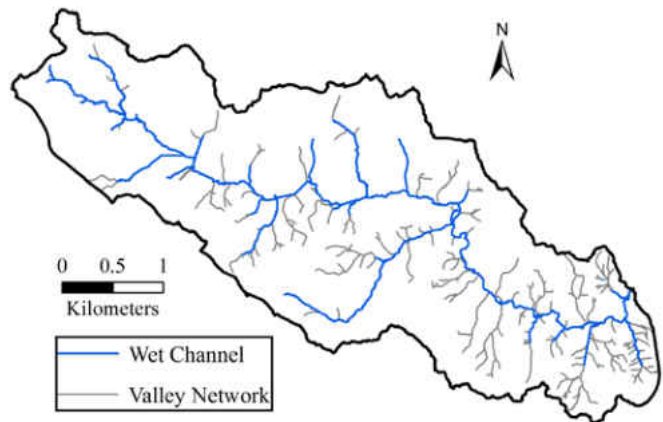
Figure A- 12: M Chopawamsic Creek, VA

133
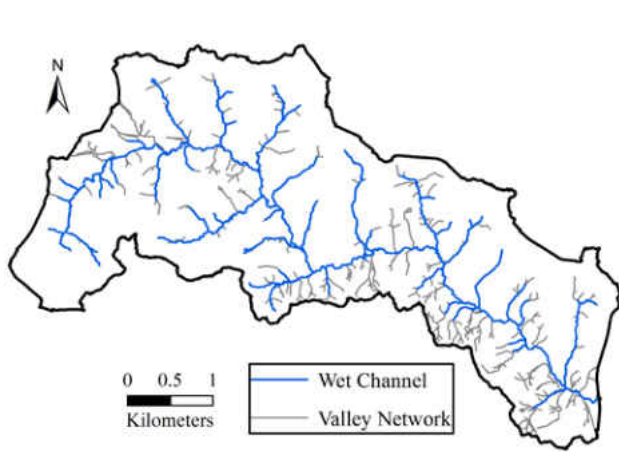
Figure A- 13: N Chopawamsic Creek, VA
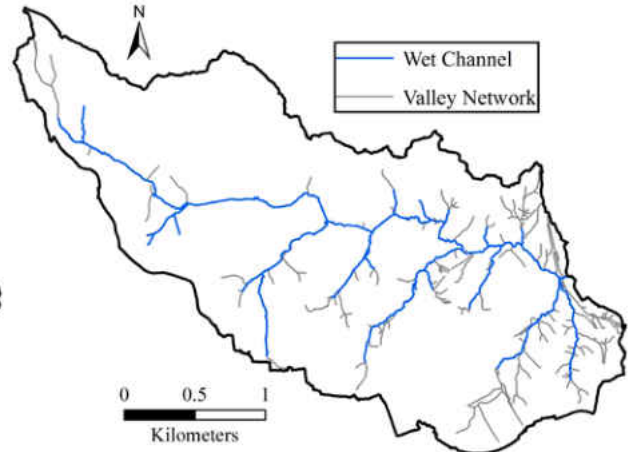
Figure A- 14: S Chopawamsic Creek, VA
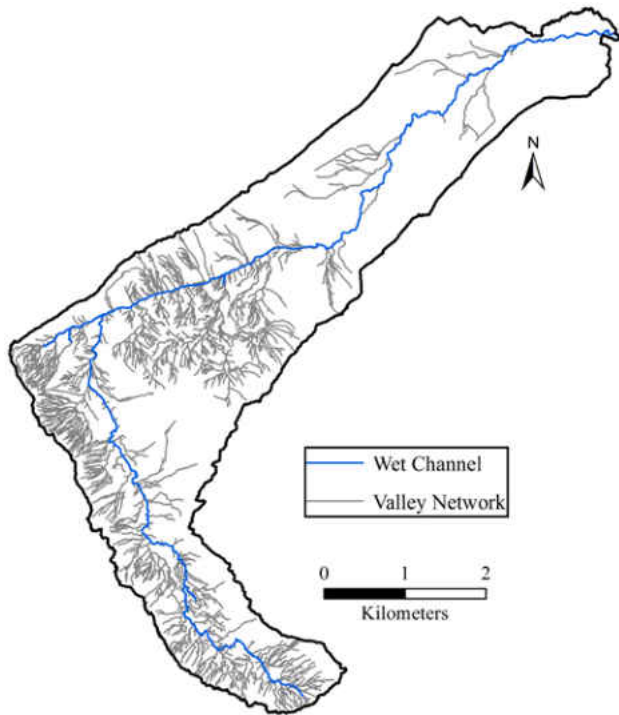
Figure A- 15: General Creek, CA
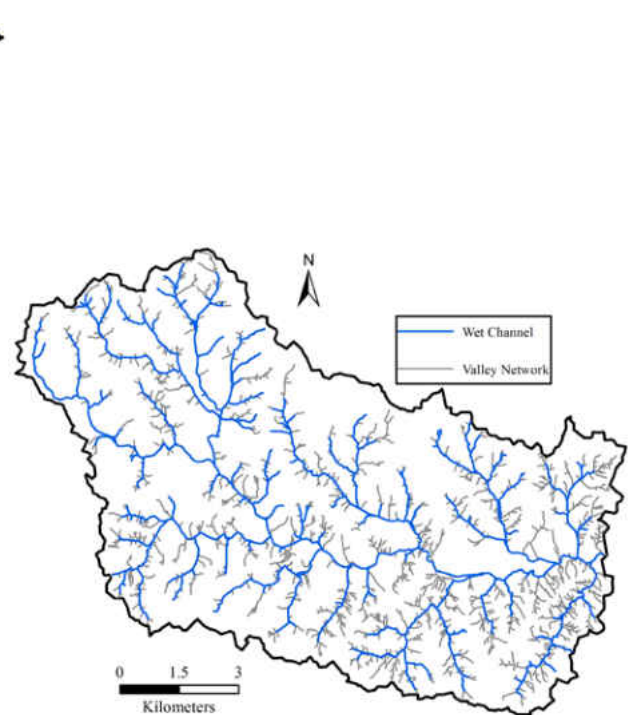
Figure A- 16: Allison Creek, SC

134
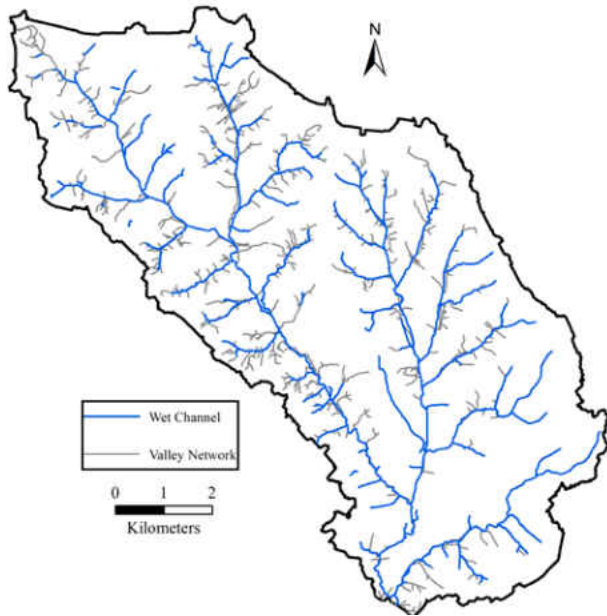
Figure A- 17: Wildcat Creek, SC

Figure A- 18: Pennington Creek, OK
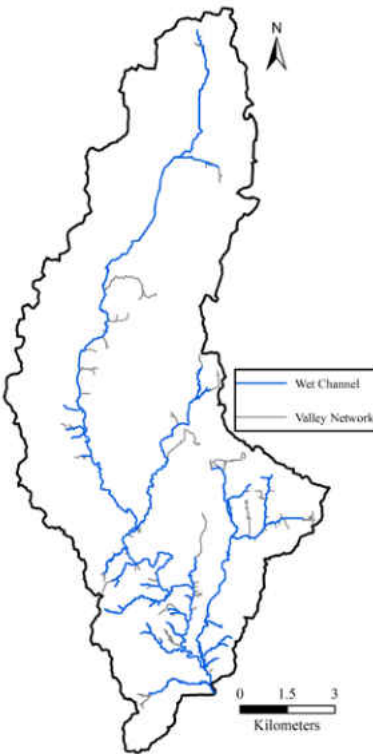
Figure A- 19: Mill Creek, OK

Figure A- 20: Rock Creek, OK

135
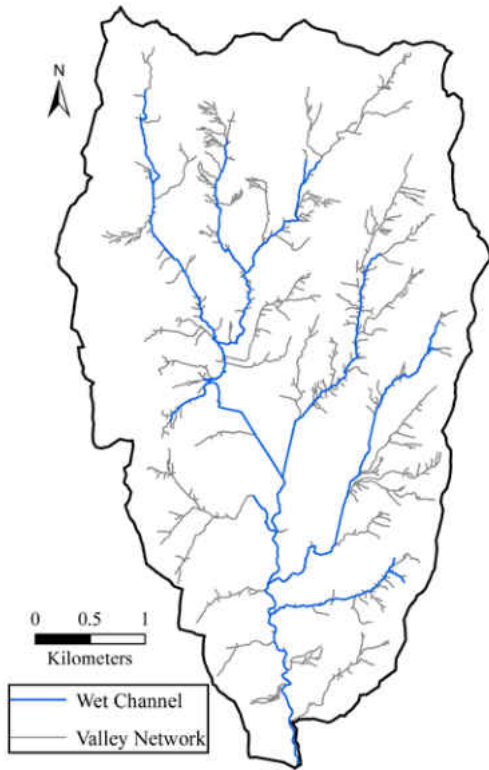
Figure A- 21: North Criner Creek, OK
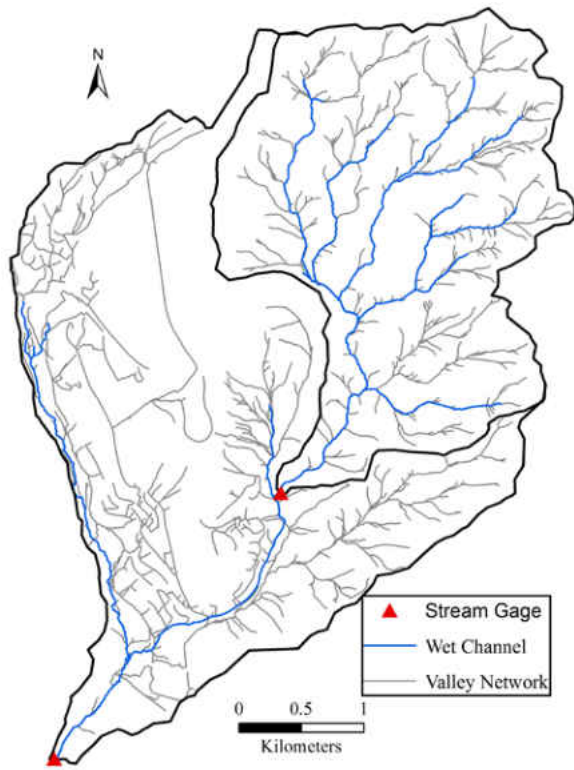
Figure A- 22: Incline Creek, NV
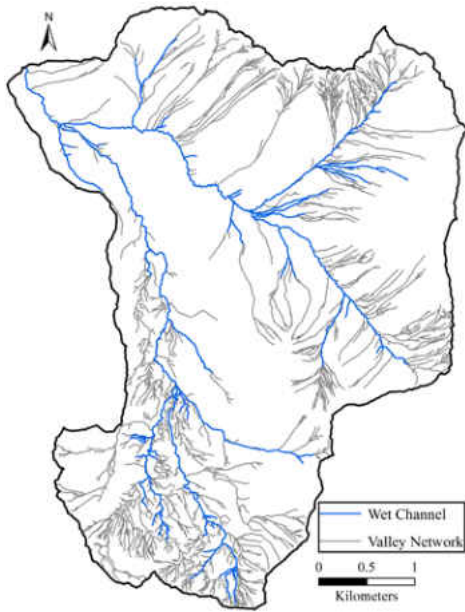
Figure A- 23: Trout Creek, CA
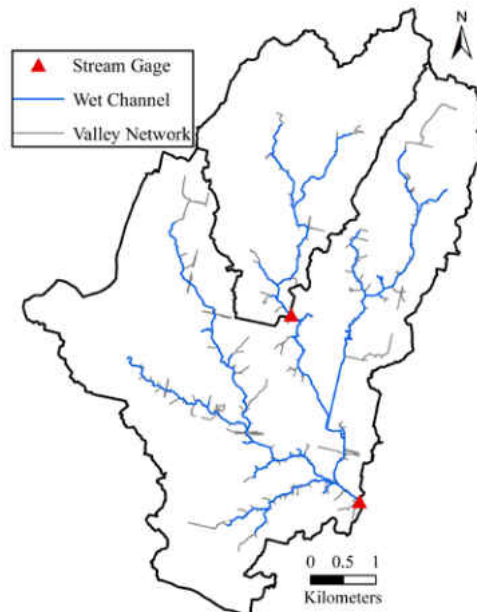
Figure A- 24: Little Washita River, OK
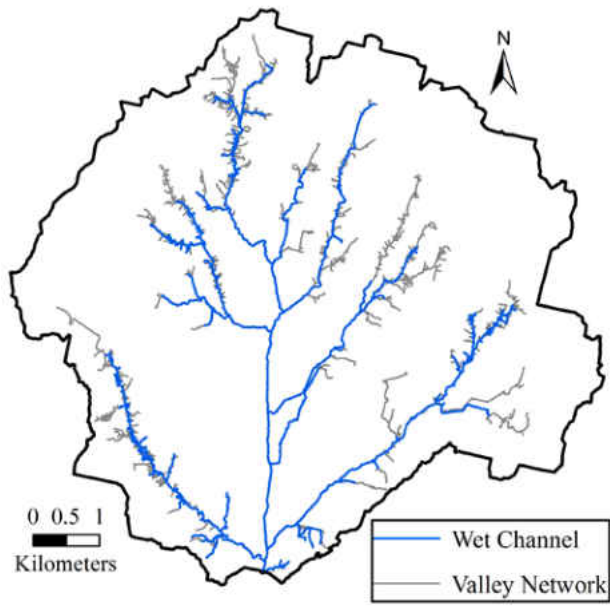
Figure A- 25: Lake Creek, OK
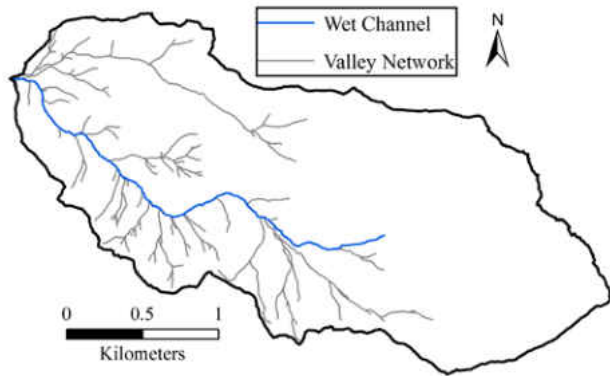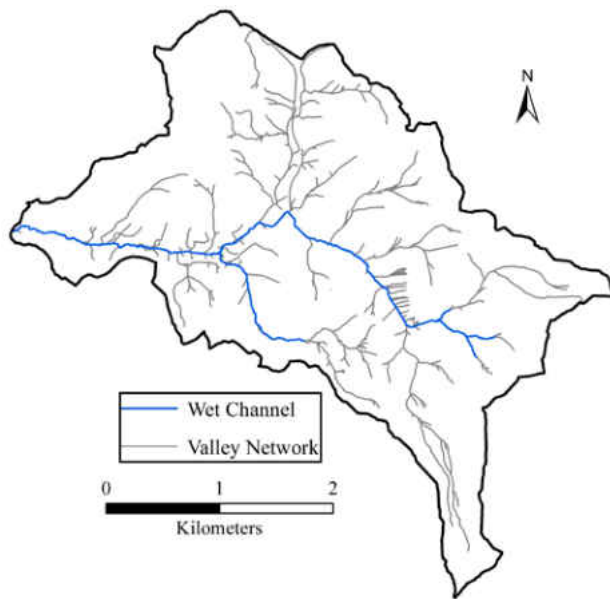

Figure A- 26: Logan House Creek, NV
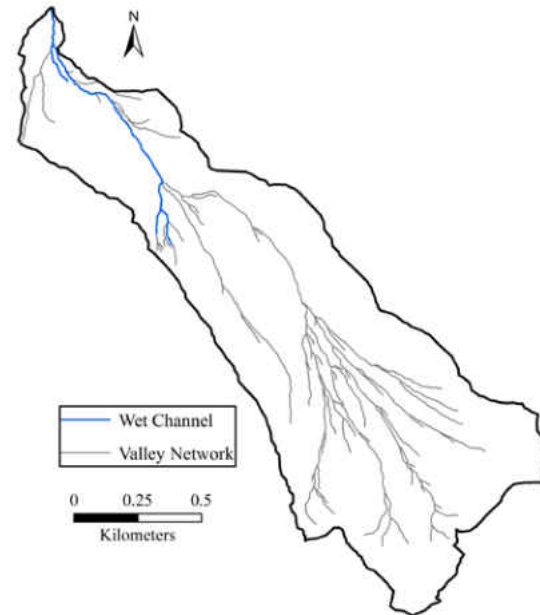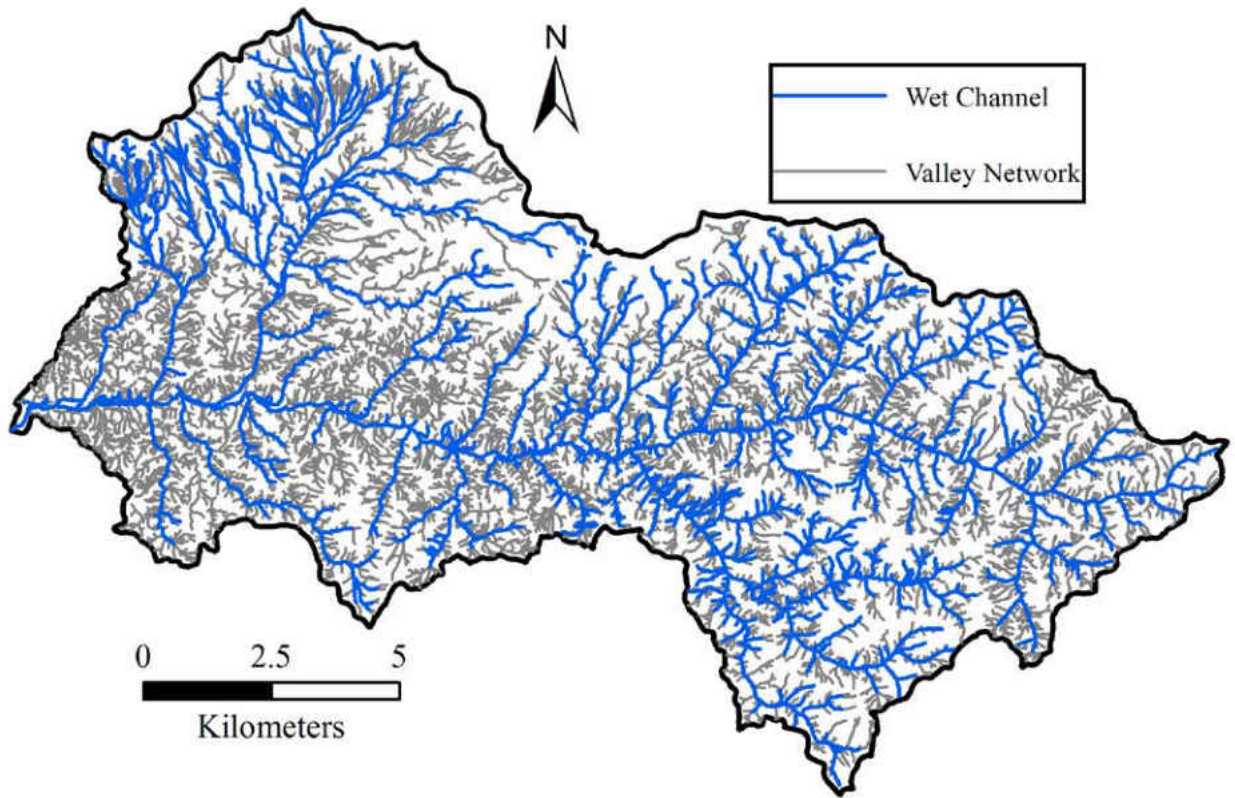

Figure A- 27: Glenbrook Creek, NV

Figure A- 28: Eagle Rock Creek, NV

137

Figure A- 29: Pine Creek near Clarno, OR